To the Graduate Council:
I am submitting herewith a dissertation written by Ying-Ling Chen entitled "Laser-Induced Gas Breakdown and Ignition". I have examined the final copy of this thesis for form and content and recommend that it be accepted in partial fulfillment of the requirements for the degree of Doctor of Philosophy, with a major in Physics.

J. W. L. Lewis, Major Professor

We have read this thesis
and recommend its acceptance:

Accepted for the Council:

Associate Vice Chancellor
and Dean of The Graduate School

# Laser-Induced Gas Breakdown and Ignition

A Dissertation

Presented for the

Doctor of Philosophy

Degree

The University of Tennessee, Knoxville

Ying-Ling A. Chen

May 1998

# Dedication

Dedicated to my parents

# Acknowledgements

I would like to thank Dr. J. W. L. Lewis, who has been my academic advisor and a good friend since I arrived at the University, for his patience and guidance to my academic and experimental achievement.

I would also like to thank my friends Dr. Christian Parigger, Dr. David Plemmoms, Dr. Lloyd Davis, Yuanji Tang, Guoming Guan, Yuxing Sun, Matt Boddicker and the research staff in the Center for Laser Applications: Newton Wright, Jim Few, Fred Schwartz, and Jim Hornkohl, for their countless supports, advice and friendships over the past many years.

# Abstract

Laser-induced gas breakdown and ignition are studied in atmospheric pressure gas flow. The nanosecond-pulsed, 1064-$nm$ Nd:YAG laser was used to create the cascade-type optical breakdown in air, oxygen, ammonia, and the combustible ammonia/oxygen mixture. We investigate the formation of the initial plasma and the chemical and gasdynamic development of the breakdown kernel. The spatial and temporal features of the energy deposition process are presented for laser breakdowns in still air. The generation of air-breakdown events is very stable between laser pulses when the incident laser power is two times larger than the threshold value. The effects associated with the ammonia flow-speed in the range of 1-7 $cm/sec$ are shown to be significant for the plasma formation and stability of both laser-induced breakdown and ignition kernel, even though the flow field is laminar. The post-breakdown development of laser breakdown and ignition is studied using high-speed photographic and spectroscopic techniques including shadowgraphs, planar laser-induced fluorescence (PLIF), spontaneous emission and Rayleigh scattering. These time-resolved two-dimensional images provide gasdynamic, radiative and NH radical concentration and temperature information to aid the understanding of the kernel dynamics. The asymmetric feature of the initial plasma and the gas dynamics that leads to the backstreaming effect in laser-induced breakdown is suggested and evaluated.

# Contents


**1 Introduction** **1**

**2 Overview of Laser-Induced Gas Breakdown and Ignition** **7**

2.1 Laser-Induced Gas Breakdown . . . . . 7

2.2 Laser-Induced Ignition . . . . . 10

**3 Energy Deposition of Laser-Induced Breakdown in Still Air** **18**

3.1 Energy Absorption in Laser-Induced Breakdown . . . . . 18

3.1.1 Experimental Setups . . . . . 21

3.1.2 Results and Discussion . . . . . 23

3.2 Images of Energy Deposition Process . . . . . 27

3.2.1 Experiment . . . . . 29

3.2.2 Results and Analysis . . . . . 31

**4 Laser-Induced Breakdown in the Flow Field** **39**

4.1 Threshold of Laser-Induced Breakdown . . . . . 39

4.1.1 Experiment . . . . . 42

4.1.2 Results and Discussion . . . . . 44

4.2 Probability Distribution Function (PDF) of NH Density in Optical Breakdown and Ignition . . . . . 53

4.2.1 Experiment . . . . . 54

4.2.2 Laser-Induced Breakdowns in Ammonia Flow . . . . . 56

4.2.3 Laser Ignition in Premixed Ammonia/Oxygen Flow Field . . 59

**5 Time-Resolved Shadowgraphs and Kernel-Dynamics of Laser-Induced Breakdown and Ignition** **64**

5.1 Experiment of Shadowgraphs . . . . . 67

5.2 Shock Waves and Kernel Development in the Early Period . . . . . 69

5.3 Development of a Single Laser-Induced Breakdown Event . . . . . 71

5.4 Laser-Induced Breakdown in Still Air . . . . . 77

5.5 Laser-Induced Spark Ignition . . . . . 77

**6 Detection of NH in Optical Breakdown Using Laser-Induced Fluorescence (LIF) — Theoretical Preparation** **83**

6.1 Introduction to LIF . . . . . 84

6.2 Calculation of NH ($A^3\Pi_i$-$X^3\Sigma^-$) Spectrum . . . . . 85

6.3 Time-Dependent Study Using Two-Level Model . . . . . 89

6.4 Collisional Effects and the Four-Level Model . . . . . 98

6.5 Consideration of NH Temperature and Concentration Measurement . 107

**7 Time-Resolved Images Using Spectroscopic Techniques** **113**

7.1 Experiment Details . . . . . 114

7.2 Time-Resolved Images of NH Spontaneous Emission and PLIF . . . . 118

7.3 NH Temperature and Concentration Images . . . . . 125

7.4 Features of Kernel Development . . . . . 140

**8 Summary** **144**

**Bibliography** **149**

**Appendices** **164**

**A Calibrations of Experimental Apparatus** **165**

**Vita** **170**

# List of Figures


2.1 Temperature and mole fraction calculation of atmospheric-pressure ammonia/oxygen flame . . . . . 13

2.2 Mole fractions of various molecules as functions of the distance in the flame front of the stoichiometric $NH_3/O_2$ laminar flame. . . . . 15

2.3 One-dimensional freely propagating ammonia/oxygen flame: (a) calculated temperature, density, and NH mole fraction across the flame front (stoichiometric condition), (b) calculated laminar flame speed as a function of the equivalence ratio. . . . . 16

3.1 Temporal structure of energy deposition in laser-induced breakdown . 19

3.2 Experimental geometry in the study of energy absorption, B.S.= beam splitter, E1 = energy meter (Laser Precision, Model Number RJP-734), E2 = energy meter (Scientech, Model Number P50), M = mirror, Pol.= polarizer, B.E.= beam expander, L = lens . . . . . 22

3.3 Energy-absorption study in laser-induced air breakdown . . . . . 24

3.4 Energy-absorption study in laser-induced air breakdown . . . . . 25

3.5 Spatial feature of energy absorption in laser-induced air breakdown . 28

3.6 Experimental geometry in the study of energy absorption, B.S.= beam splitter, E1 = energy meter (Laser Precision, Model Number RJP-734), E2 = energy meter (Scientech, Model Number P50), M = mirror, Pol.= polarizer, B.E.= beam expander, L = lens . . . . . 30

3.7 Images of energy deposition process in laser-induced air breakdown . 32

3.8 Images of energy deposition process in laser-induced air breakdown . 33

3.9 Images of energy deposition process in laser-induced air breakdown . 34

3.10 Calculated aberration pattern of a Gaussian laser beam focused by a 100 $mm$ focal length, plano-convex lens . . . . . 36

4.1 Experimental geometry in the study of threshold, B.S.= beam splitter, right energy meter: (Laser Precision, Model Number RJP-734), left energy meter: (Scientech, Model Number P50), M = mirror, Pol.= polarizer, B.E.= beam expander, L = lens, flat-flame burner (McKenna, 316 stainless steel) . . . . . 43

4.2 Threshold measurement in laser-induced breakdown in ammonia flow. flow-speed: 1.0 $cm/sec$, repetition rate: 10 $Hz$, location: 10 $mm$ above burner. . . . . 45

4.3 Threshold measurement in laser-induced breakdown in ammonia flow: (a) comparison between repetition rate of 2 and 10 $Hz$, (b) comparison of air and ammonia breakdowns. solid symbols: 10 mm above burner, hollow symbols: 30 mm above burner. . . . . 46

4.4 (a) Threshold measurement in laser-induced breakdown in ammonia flow without mixing with ambient air. (b) 90° scattering of 340 $nm$ UV light in ammonia flow. . . . . 47

4.5 Breakdown-threshold measurement in air and ammonia flow. . . . . 52

4.6 Experimental geometry in the study of threshold: B.S.= beam splitter, left energy meter (Laser Precision, Model Number RJP-734), right energy meters (Scientech, Model Number P50), M = mirror, Pol.= polarizer, B.E.= beam expander, L = lens, flat-flame burner (McKenna, 316 stainless steel) . . . . . 55

4.7 Spontaneous emission spectrum of laser-induced breakdown in ammonia flow. . . . . 57

4.8 Probability distribution functions of NH concentration in ammonia breakdowns. . . . . 58

4.9 Laser-power dependence of pdf of NH concentration in ammonia breakdowns. ammonia flow: 6.5 $cm/sec$. . . . . 60

4.10 Probability distribution functions of NH concentration in ammonia breakdowns. A quartz-cylinder was used to eliminate air-mixing effect. 61

4.11 Results of laser-ignition experiment: (a). scatter plot of NH fluorescence and absorbed laser energies for failed and successful ignitions, (b). probability distribution functions of absorption, and (c). probability distribution functions of NH concentration. . . . . 62

5.1 Experiment arrangement for shadowgraphs, L = lens, M = mirror, Pol. = polarizer, B.E. = beam expander, P.D. = photodiode . . . . . 68

5.2 Shadowgraphs of laser-induced breakdowns in air (left) and premixed ammonia/oxygen flow (middle: mole-ratio=4/3, right: mole-ratio=2/1) 70

5.3 Shadowgraphs of one individual laser-induced breakdown in still air. absorbed laser energy: 26.2 $mJ$ . . . . . 72

5.4 Shadowgraphs of one individual laser-induced breakdown in premixed ammonia/oxygen mixture. absorbed laser energy: 26.2 $mJ$ . . . . . 74

5.5 Shadowgraphs of three individual laser-induced breakdowns in still air. absorbed laser energy: 26.2 $mJ$ . . . . . 78

5.6 Shadowgraphs of three individual laser-induced breakdowns in still air. absorbed laser energy: 54 $mJ$ . . . . . 79

5.7 Shadowgraphs of laser-induced breakdowns in premixed ammonia/oxygen flow. mole-ratio = 0/1 (left), 4/3 (middle), 2/1 (right). flow speed = 6 $cm/sec$ . . . . . 80

6.1 Synthetic spectra of NH ($A^3\Pi_i$-$X^3\Sigma^-$) spontaneous radiation. . . . . 87

6.2 NH excitation spectra in atmospheric-pressure ammonia/oxygen flame. 88

6.3 Diagram of two energy levels for LIF modeling. $N$ = state population density, $g$ = degeneracy, $A$ = rate of the spontaneous emission, $Q$ = rate of collision-quenching, $b_{12}$ = rate of absorption, $b_{21}$ = rate of stimulated emission . . . . . 90

6.4 Time-dependent excited-state population for molecules pumped by a rectangular-shaped laser pulse of duration $\tau_L$. $\tau_{21}$ = relaxation time. (a) $\tau_L = 0.2\tau_{21}$, (b) $\tau_L = \tau_{21}$, and (c) $\tau_L = 5\tau_{21}$ . . . . . 95

6.5 Steady-state population as a function of saturation parameter . . . . 99

6.6 Diagram of four energy levels for LIF modeling. $N$ = state population density, $g$ = degeneracy, $D$ = downward transfer rates = $A + Q$, $T$ = energy transfer rates, $b_{12}$ = rates of absorption, $b_{21}$ = rate of stimulated emission. . . . . 103

7.1 Experimental geometry in the study of energy absorption, B.S.= beam splitter, E1 = energy meter (Laser Precision, Model Number RJP-734), E2 = energy meter (Scientech, Model Number P50), M = mirror, Pol.= polarizer, B.E.= beam expander, L = lens . . . . . 115

7.2 Synthetic spectra of NH(A-X), OH(A-X) and $N_2(2^{nd}$ Positive). relative transmissions of narrow band-pass filter for NH(A-X) PLIF experiments, broad band-pass filter for NH temperature experiments, and 1-dimensional OMA (red dotted lines) for excitation scan experiments 116

7.3 Timing control in the experiments of spontaneous emission, laser-induced fluorescence, and Rayleigh scattering . . . . . 119

7.4 Images of NH(A-X) spontaneous emission in laser-induced ammonia breakdown . . . . . 120

7.5 Images of NH(A-X) planar laser-induced fluorescence in laser-induced ammonia breakdown . . . . . 121

7.6 Images of NH(A-X) planar laser-induced fluorescence in laser-induced ammonia/oxygen ignition . . . . . 123

7.7 NH excitation spectra in atmospheric-pressure laser-induced ammonia breakdowns . . . . . 126

7.8 Measurement of LIF saturation irradiance in atmospheric pressure ammonia/oxygen flame . . . . . 130

7.9 Measurement of LIF saturation irradiance in atmospheric pressure pure ammonia breakdowns; transient breakdown kernels at 5 $\mu sec$ delay time were detected . . . . . 131

7.10 Time-resolved temperature images of laser-induced ammonia breakdowns recorded at 3, 5, 10 and 20 $\mu sec$ after breakdown were initialed. Nd:YAG laser pulse energy = 21 $mJ$ . . . . . 133

7.11 Time-resolved NH PLIF images of laser-induced ammonia breakdowns used to calculate temperature maps. Nd:YAG laser pulse energy = 21 $mJ$ . . . . . 134

7.12 NH concentration images of laser-induced ammonia breakdowns calculated from NH PLIF and temperature maps. Nd:YAG laser pulse energy = 21 $mJ$ . . . . . 135

7.13 The Boltzmann plot of a single pixel in two-dimensional temperature measurement . . . . . 136

7.14 Time-resolved temperature images of laser-induced ammonia breakdowns recorded at 3, 5, 10 and 20 $\mu sec$ after breakdown were initialed. Nd:YAG laser pulse energy = 32 $mJ$ . . . . . 137

7.15 Time-resolved NH PLIF images of laser-induced ammonia breakdowns used to calculate temperature maps. Nd:YAG laser pulse energy = 32 $mJ$ . . . . . 138

7.16 NH concentration images of laser-induced ammonia breakdowns calculated from NH PLIF and temperature maps. Nd:YAG laser pulse energy = 32 $mJ$ . . . . . 139

7.17 Rayleigh scattering of the sheet laser beam in front of the kernel (upper image), across the kernel (middle image), and in the back of the kernel (lower images); Images were recorded at 5 $\mu sec$ after breakdown were initialed . . . . . 142

8.1 Chart of recording time of the two-dimensional images presented in this dissertation . . . . . 148

A.1 Laser pulse-energy controlled by two polarizers . . . . . 167

A.2 Calibrations of mass-flow meters, MKS-5000sccm, MKS-20000sccm and MKS-50000sccm . . . . . 168

A.3 Sensitivity calibration of CCD camera and two-dimensional OMA detection system . . . . . 169

# Chapter 1

# Introduction

Interest in the combustion of materials has surely existed since prehistoric times, and a similar interest in the controlled combustion of gas/vapor mixtures extends more than several millennia into the past. Beginning in the mid-nineteenth century, there occurred semi-quantitative development and investigations of laboratory combustion devices and phenomena, respectively. The former is exemplified by the development of a laboratory gas burner by Bunsen in 1855 [1], and the basic Bunsen burner can be found in many chemistry laboratories almost one hundred and fifty years later. Less well-known perhaps was the investigation by Faraday prior to 1825 on the behavior of illuminating gases of the flames. From that approximate time (1826), however, these studies were well-known in London where Faraday presented Christmas-season lectures and demonstrations on various topics, including the candle flame and its properties for the general public and especially school children [2, 3]. Re-creation of these lectures by the British Broadcasting Corporation showed the fascination of understanding the candle flame [3].

During and following the Second World War, an ever-increasing importance of combustion has resulted from the dramatic industrialization and technological ad-

vancement of various nations. The combustion of single and two-phase mixtures is essential for electrical power production, civil and military land, sea, air, and space propulsion, the production of metals by ore extraction, and the synthesis and development of a variety of new materials.

Such widespread use and impact of combustion clearly provide economic incentives for the improvement of the efficiency of the various combustion processes. As a result, there has existed a significant international research and development effort to achieve these desired efficiency gains. More recently, the effects of the products of combustion on environmental quality and human health have gained both national and international attention. These effects span the range of the production and transport of acid rain and its effect on forests and bodies of fresh-water, the creation of nitrogen oxides effluents and their role in the production of smog and the degradation of the natural vista. and the health hazards resulting from respiration of carcinogenic hydrocarbon soot micro-particles that are common products of a variety of combustion process. To mitigate these and other possibly harmful effects, further combustion research will be required.

One of the areas of basic combustion research that has received comparatively little attention in the past several decades has been that of the ignition of the combustible mixture. The reasons for this are clearly understandable. First, the primary method of ignition for the majority of applications is the electric-discharge spark plug. For spark ignition of both gas/vapor and two-phase mixture, Ballal and Lefebvre, as described in Reference [4], have provided an excellent description of the phenomena in terms of macroscopic parameters that were capable of measurement or estimation

at the time of the research. Minimum ignition energy and ignition delay times were determined for a wide range of fuel/oxidizer mixture, flow speeds, characteristic sizes of practical liquid fuel-sprays and other parameters of engineering importance. As a result, the majority of the research work has concentrated on the understanding and optimization of the chemical and fluid mechanical properties of the fuel/oxidizer mixtures that are convected to the spark device. Secondly, there was no reasonable alternative to the spark plug, and as has been discussed, the spark plug was reasonably well understood insofar as its engineering design was concerned.

Even though use of the spark-ignition device is wide-spread, it may contribute to the production of some of the previously mentioned undesirable combustion products. For example. the wall-mounted spark-plug can easily be imagined to produce both gas-phase molecular species and particulates that would not exist without the contributory effect on the reactions by the solid-surface of the combustor wall. In the past, computation and experimental detection of such phenomena were impractical. Within the past decade, several developments have occurred that may beneficially impact the selection, design, and use of ignition device. The first is the most revolutionary and is the possible use of laser ignition of both gas/vapor and two-phase mixture. The more evolutionary, but important, developments include significant improvements in the capabilities to compute and measure detailed atomic, molecular, and particulate properties of the ignition environments.

The most obvious potential advantages of laser ignition of both gas/vapor and two-phase mixture are: (1) the ability to ignite the mixture in spatial regions that are distant from the combustor wall, which will eliminate a portion of the soot production

on the solid surface of the wall and (2) the capabilities of igniting the mixture at the desired stoichiometric or equivalence ratio.

However, the operational parameters of the laser ignition source differ significantly from those of the electric spark plug, and the implications of these differences are not obvious. For example, to achieve breakdown with practical-size lasers, the pulse-width of the laser will be typically two orders-of-magnitude smaller than that of the spark plug, and the pulse energy of the laser will typically be one to two orders-of magnitude smaller than that of the spark plug. Further, the laser source has the potential of producing a discharge in a very small, nearly spherical volume in contrast to the elongated, cylindrical spark discharge. These two differences alone, relative to the spark plug, have the potential of altering the properties of the plasma discharge, the ion-electron recombination rate and plasma chemistry properties and the subsequent time-space characteristics of the temperature(s) and reaction intermediates and products. Additional differences may exist for the minimum ignition energy, ignition delay time, the magnitude of shock-heating of the surrounding mixture and the turbulent flame speed.

The published research work of the laser ignition of gas/vapor mixture is limited, and the laser-ignition research of the two-phase mixtures has been mostly proprietary and necessarily described by both U.S. and foreign patents of Lewis and Few [5, 6].

The previous studies of gas/vapor ignitions include the macroscopic measurements of the minimum ignition energy [7, 8, 9, 10, 11, 12, 13, 14, 15, 16] and the ignition delay time [17, 18] for various laser sources and ignition mechanisms. More or less, the measured ignition energies using laser sources are typically greater than those

of electric spark ignition and the theoretical combustion calculations, and laser ignition seems to have the favor of the fuel-lean mixture condition. In electric spark ignition, the effects of both the flow-speed and turbulence on the minimum ignition energy are studied [19, 20, 21], but how the flow environment affects the formation and development of laser spark is not yet understood. The measured laser ignition delay times are typically one to two orders of magnitude shorter than the electric spark ignition. The shapes of the ignition kernels have been investigated using either Schlieren photography [18] or planar laser-induced fluorescence technique [18, 22, 23], and in contrast to the electric spark, the ignition flame-kernel of the laser spark shows significant difference in the symmetry of the gas-dynamic/flame development features. Understanding the overall difference between these two types of ignition sources. which is a result of the characteristics of the ignition sources, the effects of the mixture properties and the flow environment, will require both microscopic measurements and measurements of chemical and gas-dynamic properties of laser-ignited sources and a parallel development of theoretical predictions.

The objective of this work is to perform an experimental study of the laser ignition of a combustible gas/vapor mixture that has the following features:

1. chemical kinetics coefficients that are reasonably well-known over the relevant range of properties of the phenomena

2. spectroscopically simple emission and fluorescence signatures that will allow detailed, spatial and temporal properties of the temperature and the density of one or more reactive molecules

3. the existence of free-radical species whose detection will yield flame-front information, and

4. a mixture for which the fuel can be observed in a condensed phase for future studies of laser ignition of two-phase mixtures of the same species.

For these reasons, ammonia/oxygen was chosen as the mixture, and the subsequent material describes this work.

# Chapter 2

# Overview of Laser-Induced Gas Breakdown and Ignition

## 2.1 Laser-Induced Gas Breakdown

Laser-induced optical breakdown was first reported by Maker, Terhune, and Savage in 1963 [24]. It was found that when a Q-switched ruby laser pulse with the maximum power of tens of megawatts, passes through a focusing lens in the air, a spark exploded at the focal point similar to the electric breakdown between two electrodes. Following the first report of pulsed laser-induced discharges, numerous research studies of this topic have been carried out in a variety of media. Many review works summarize the research and give the detailed discussion of laser-induced discharge and its applications [25, 26, 27, 28, 29, 30, 31]. A typical laser-induced gas breakdown can be divided into three successive stages. First, the strong irradiance, or electric field, of the laser interacts with the gas and generates the initial optical breakdown: ionization is produced and the initial plasma appears. Next, the newly formed plasma interacts with the rest of the laser pulse. The plasma front is supported or maintained by the laser radiation, and the plasma is heated to very high temperature. Finally, a detonation-

like phenomenon appears, and it continues after the end of the laser pulse. A bright spark in the focal position and a gradually decaying shock-wave can be observed or measured. The propagation motion of plasma along the laser beam toward the focal lens is a general tendency in laser discharges. Processes such as shock wave heating, radiation, and heat conduction from the initial plasma can change the physical condition in the surrounding area and cause the ionization of gas layers adjoining the discharge plasma. This expansion of discharge during the second and third stages appears like the propagation of plasma. A relatively weak field (compared to the breakdown threshold) is sufficient to propagate the plasma that is already initiated.

Under the strong electric field of the laser beam, two primary mechanisms are responsible for the optical breakdown: the electron-impact ionization ($e^- + X \longrightarrow 2e^- + X^+$, $e^- + X^+ \longrightarrow 2e^- + X^{++}$, ...) and the multiphoton ionization (MPI) ($X + mh\nu \longrightarrow e^- + X^+$). The first mechanism requires an initial (or seed) electron to start this cascade process. This electron may be generated by the multiphoton ionization, the thermionic emission in a larger particle, or through the electron-tunnel effect [30, 32]. The electron density created through impact ionization increases exponentially with time. Through the multiphoton ionization, on the other hand, electron density increases constantly with the rate constant proportional to $(I_L)^m$, where $I_L$ is the laser irradiance and $m$ is the number of photons required in a MPI process. Generally, the ionization process of the laser-induced breakdown involves both mechanisms, although one may dominate the process during most of the period of the electron growth. Since the multiphoton ionization needs a certain number of photons to reach the ionization energy, i.e. $m/\lambda \propto mh\nu > \epsilon_I$, the MPI process is dependent

on the laser wavelength. Taking nitrogen for example, with the laser wavelength of 1064 $nm$, the first MPI requires absorption of twelve photons. The MPI cross section was measured as $4\times10^{-142}$ $(W/cm^2)^{-12}$ [33] under the above conditions. Using a typical nanosecond laser with output energy of tens to hundreds $mJ$/pulse, the electron growth through MPI is not quite sufficient to support the breakdown at atmospheric pressure, but it is possibe to supply the required initial electron for the impact-ionization breakdown. For this type of non-resonant laser-induced breakdown, the energy absorption of the initial plasma is tenuous, and is via the mechanism of electron-neutral inverse bremsstrahlung. When the electron density is sufficiently high, the absorption mechanism transfers to the electron-ion inverse bremsstrahlung process, and photon absorption by excited-states species can also contribute significantly to the final ionization state. Following creation of the plasma, the absorption of the incoming beam is near 100%, and the plasma temperature increases rapidly. The plasma expansion in this stage is not significant until the temperature and pressure are increased greatly. The expansion of the high-pressure hot plasma, occurring in the third stage, drives the shock wave outward into the ambient gas to release the pressure. For the laser-induced discharge using a very short pulse ($< 10$ $psec$), the multiphoton ionization mechanism (photon-molecule interaction) alone must provide the breakdown, since there is not sufficient time for electron-molecule collisions to occur. The breakdown threshold, therefore, is much higher than the nanosecond laser-induced breakdown, and the formation of initial plasma differs from what is described above.

The features of the propagating plasmas are determined by laser irradiance and

the gas conditions. Three primary absorption waves are known as the laser-supported combustion wave (LSC), the laser-supported detonation wave (LSD), and the laser-supported radiation wave (LSR). The temperature and pressure profile, propagation speeds of plasmas, and the intensities of shock waves are very different between these three types of plasmas. Typically, for laser irradiance greater than 10 $GW/cm^2$, the initial plasma behaves as a radiation wave (LSR). The plasma propagation speed is estimated to be on the order of $10^6$ $cm/sec$, and the temperature and pressure are approximately $10^6$ $K$ and $10^3$ $bar$ respectively.

After the laser pulse terminates, the electron density decays through the electron-ion recombination, molecular gas recombination and attachment, and the electron diffusion. The energy in the plasma core is released by radiation, thermal conduction, and heating of the shock wave. With one major exception, following cessation of the laser pulse, the description of the development of the plasma and gas-dynamic expansion and the ensuing chemical kinetics, for laser- and electric-spark breakdowns are expected share significant similarities. The major exception is the formation, development, and dynamics of asymmetric plasma kernels [10, 18, 22, 23]. Various mechanisms have been suggested to explain this asymmetric kernel development, including laser preheating [34] and the residual velocity from the initial plasma [23], but none has yet been verified.

## 2.2 Laser-Induced Ignition

Similar to an electric spark, laser-induced breakdown in a combustible gas mixture can lead to ignition. For the intrusive electrode-sparks, some particular concerns

of ignition studies are the heterogeneous catalysis, ablation of material, interference with the expanding flame front, and the interference from walls. Laser-induced breakdown provides a spatially and temporally well-defined energy source located in free space, for which the fuel/oxidant condition is well controlled, with the potential for significant increases in output power, fuel economy, and changes in pollution levels. In addition to the laser-induced discharge, two other laser-gas mechanisms, which do not involve electrical breakdown, can also lead to ignition [8, 16, 17, 22, 35, 36, 37, 38]. One is thermal initiation, and the other is photochemical ignition. A review of laser ignition by these three types of mechanisms is given by Ronney in 1994 [38]. In this dissertation, we investigate only non-resonant breakdown and the laser-spark ignition. The features of resonant laser-induced breakdowns are similar to those of the non-resonant type except for the ionization process in the early stage, while resonant photoionization reduces the minimum energy required for initiation [14, 15, 22].

For spark-induced deflagration-type flame, regardless of the energy-deposition paths. whether the energy source will develop into a self-sustained flame depends on the total deposition energy, the spark size, and the duration of energy deposition. For the purpose of practical analysis, the minimum ignition energy $E_f$, the characteristic dimension of the ignition source $\delta_c$, and the characteristic time $\tau_c$, are defined. Roughly, the minimum ignition energy can be evaluated from a sphere of gas that provides the same energy gradient as the flame front of a sustained combustion. The radius of this ignition kernel is comparable to the flame thickness, and the characteristic time is on the order of the chemical induction time. Naturally, these values depend on the properties of the combustible mixture. The dependence of the

ignition source is primarily due to the level of energy losses in the energy deposition process. For laser-induced spark ignition, different degrees of energy loss are expected for LSC, LSD, and LSR types of plasmas, which, therefore, lead to different ignition energies and characteristic lengths. A comparatively larger-sized ignition source in any of the three spatial dimensions or a longer deposition time will lead to a larger value of minimum ignition energy. In the other words, the minimum ignition energy is found to be proportional to the length of the spark (in each spatial dimension), or/and proportional to the deposition time, if any of them exceeds the characteristic value.

For the detonation type of ignition, the heat released from the chemical reactions supports the shock front rather than the thermal conduction wave of combustion, and the flame propagates at a supersonic rate instead of a subsonic rate for the deflagration-type ignition. The minimum ignition energy is at least two orders higher than what is required in the deflagration type of ignition [11, 12, 16, 39].

In this dissertation, laser-induced deflagration-type ignition of ammonia/oxygen mixtures is studied and some of the calculated results are now presented. Equilibrium chemistry calculations were performed for atmospheric pressure mixtures of $NH_3/O_2$ for a range of equivalence ratio ($\Phi$). The NASA code of Gordon and McBride [40] was used, and Figure 2.1 shows the results for the equivalence ratio ranging from approximately 0.35 to 2.0. The concentration of both major and minor species are computed, and it is to be noted that the computed concentrations span over a seven order-of-magnitude range. Of particular interest for this work are the mole fraction values of the comparatively spectroscopically simple species such as OH, NO, H, N,

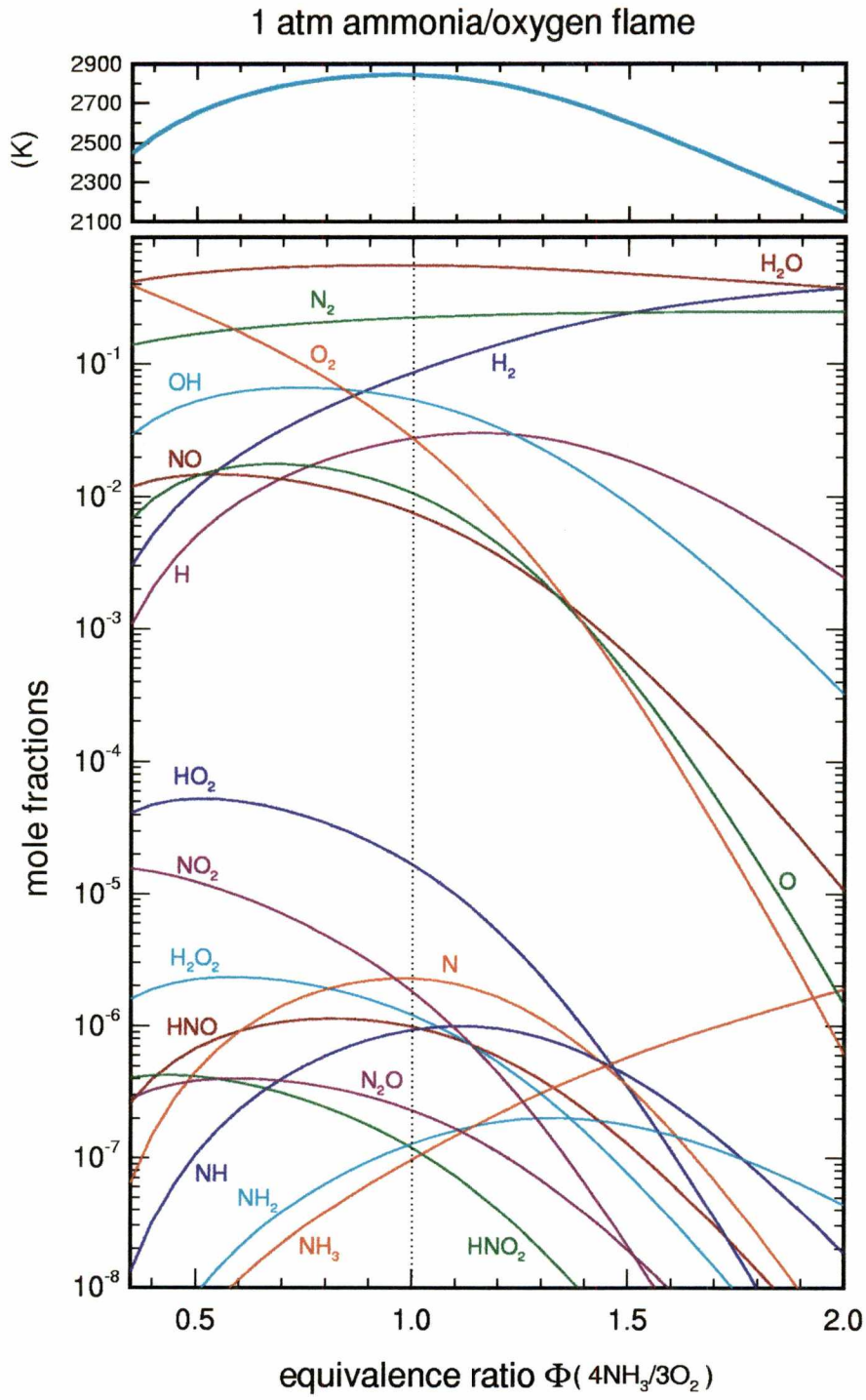



Figure 2.1: Temperature and mole fraction calculation of atmospheric-pressure ammonia/oxygen flame

and NH for which the concentrations exhibit non-zero and measurable magnitudes over the range of $\Phi$ for this work. For example, for equilibrium at $\Phi = 1$, the mole fraction of NH is approximately 1 part per million. Also shown in Figure 2.1 is the variation with $\Phi$ of the adiabatic flame temperature T for $NH_3/O_2$ combustion. It is seen that T exhibits a reasonably slowly varying dependence with $\Phi$ and is approximately 2800 $K$ for the stoichiometric ratio.

Next, the effects of finite-rate chemistry for this mixtures were evaluated using the CHEMKIN code of Sandia [41]. This computation predicts the nonequilibrium chemistry for a steady, laminar, one-dimensional flame which is appropriate for the McKenna burner that was used in this study. The $NH_3/O_2$ reaction rate database of Basevich and Vedeneev [42] were used for the CHEMKIN calculation.

Within the ignition process, a freely propagating flame consists of a well-defined flame front, where the chemical reactions involving numerous intermediates and radicals occur. Figure 2.2 is a computational result from Reference [18] using the Sandia code. It shows the mole fractions of the reactants, products, and transient species near the flame-front of the stoichiometric freely propagating flame. The distribution of the reaction intermediates illustrate a clear flame-front with a thickness of less than 0.5 $mm$. Some of the favorite diatomic molecules for density and temperature measurements in the spectroscopic diagnostics of flame are OH, NH and $N_2$. As the calculated results show, NH molecules, which are populated inside a $\sim 0.2-mm$ thin layer, can be used as a great indicator of the chemistry in the laser-ignition process. Figure 2.3(a) shows the temperature and mass density across the flame front, and the NH molecular-layer is seen to correspond to the temperature range of 1500-2500 $K$.

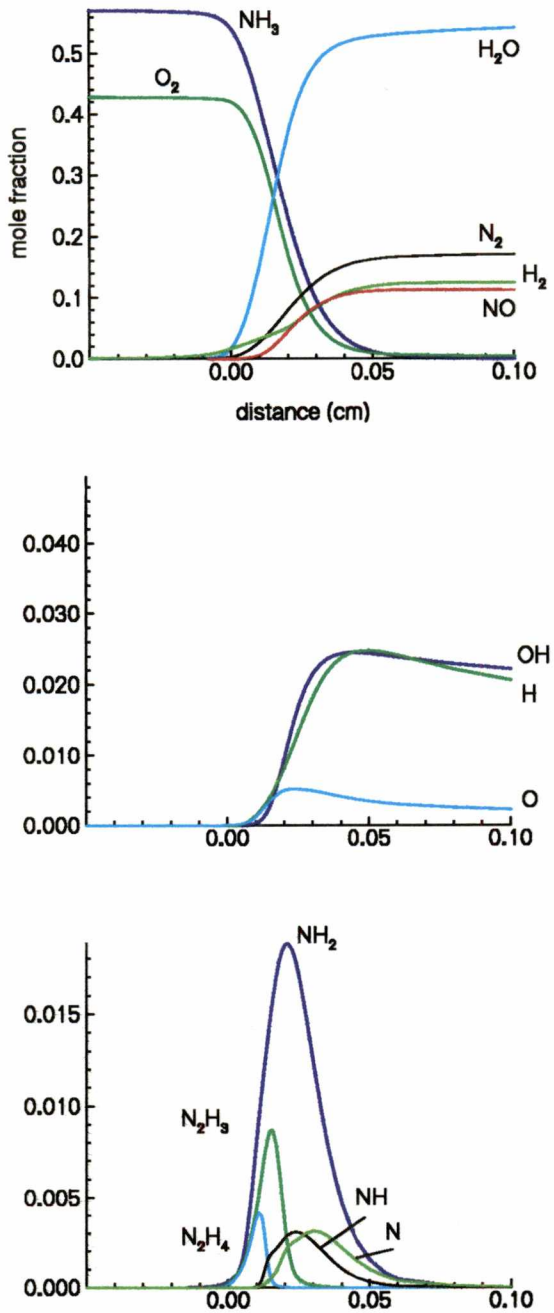



Figure 2.2: Mole fractions of various molecules in the flame front of the stoichiometric $NH_3/O_2$ laminar flame.

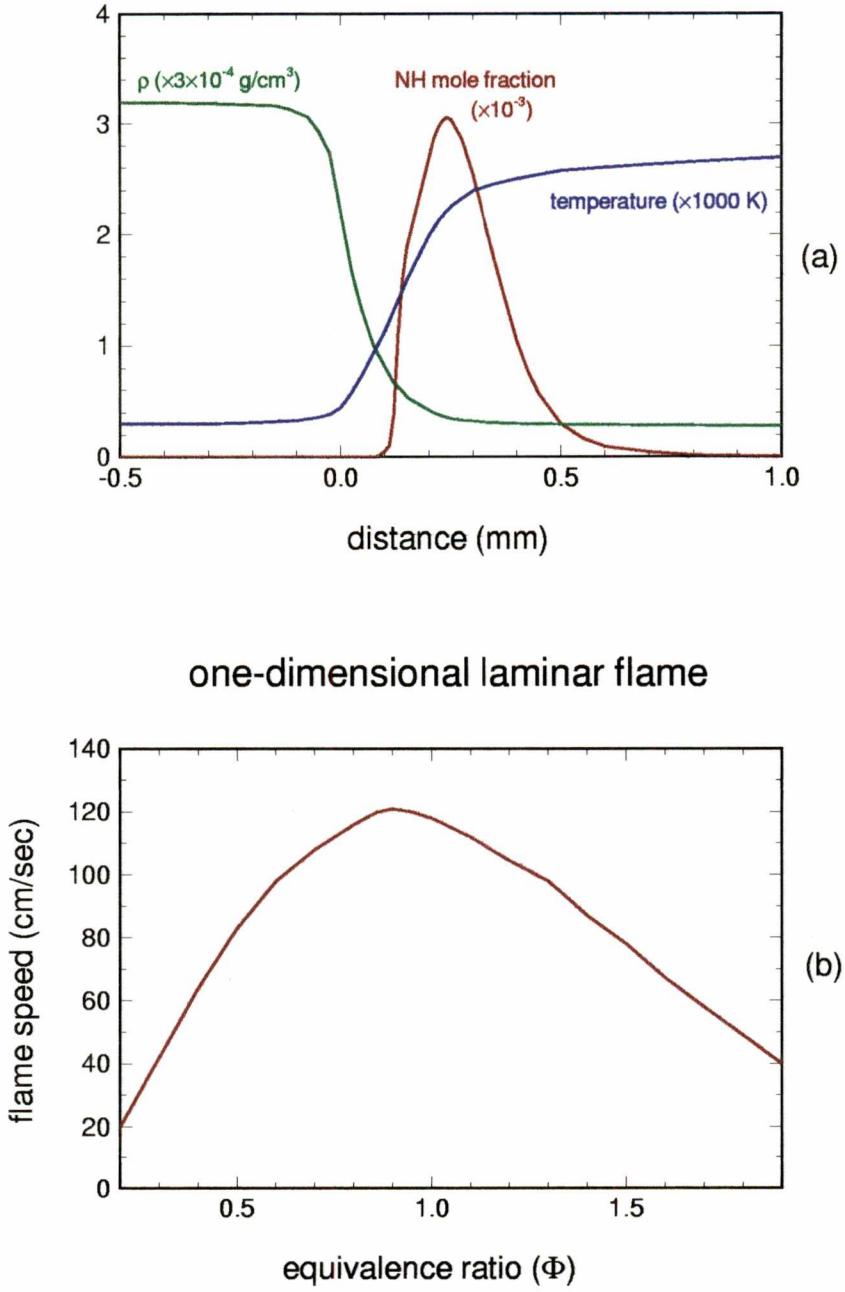



Figure 2.3: One-dimensional freely propagating ammonia/oxygen flame: (a) calculated temperature, density, and NH mole fraction across the flame front (stoichiometric condition), (b) calculated laminar flame speed as a function of the equivalence ratio.

Figure 2.3(b) gives the propagation speeds of the one-dimensional laminar flame as a function of the equivalence ratio. At the stoichiometric condition, the flame speed is about 118 $cm/sec$, which indicates an NH formation period of 100-300 $\mu sec$ in the laminar flame. For a spherically expanding flame, the flame speed is roughly 1.1 $m/sec$, which gives a characteristic time of $10 \sim 30$ $\mu sec$. If we assume the characteristic length of ammonia/oxygen ignition $\delta_c$ is 0.35 $mm$, the minimum ignition energy is then estimated

$$E_f \approx \frac{4\pi}{3}(\delta_c)^3 \rho_b \times C_p(T_b - T_u) \ , \tag{2.1}$$

where $C_p$ is the specific heat at constant pressure, $T_b$ and $T_u$ are temperatures of the burned and unburned gases, and $\rho_b$ is the density of the burned gases. The minimum ignition energy for stoichiometric mixture turns out to be $\sim 53$ $\mu J$, which is very close to the experimental result of $60 \pm 20$ $\mu J$ in the report of laser-induced ammonia/oxygen combustion by Plemmons in 1996 [18].

# Chapter 3

# Energy Deposition of Laser-Induced Breakdown in Still Air

The energy deposition process of laser-induced breakdown was studied in still laboratory air. Without the interference of strong chemical reactions and gas-flow-associated effects, the formation scenario of the initial plasma is simplified and can be revealed. In this chapter, we present and discuss the spatial and temporal features of the energy deposition process in laser-induced gas breakdowns.

## 3.1 Energy Absorption in Laser-Induced Breakdown

Significant energy absorption of a cascade type of optical breakdown starts with the generation of the initial electron. Following the rapid growth of electron density, the initial plasma becomes optically thick and absorbs practically all of the incident energy in the later laser pulse. The temporal structure of energy absorption process is described by Figure 3.1. Illustrated in Figure 3.1 are two Gaussian laser pulses with the full width at half maximum (FWHM) of 6.5 nanoseconds and peak powers

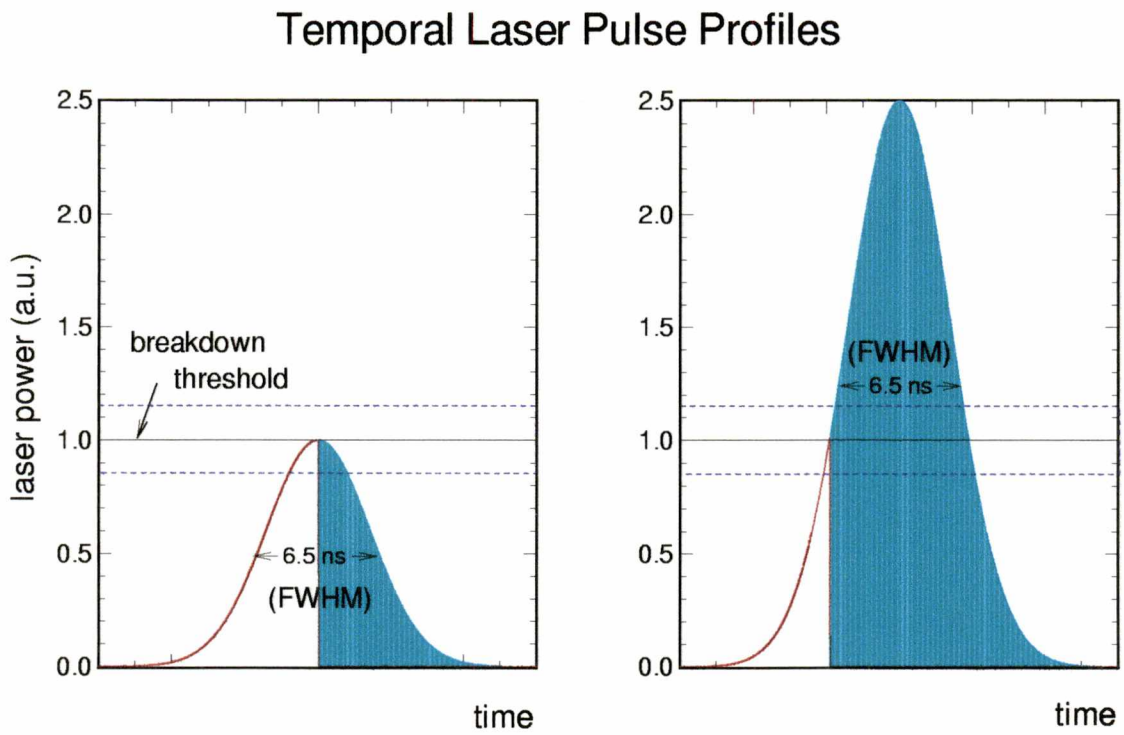



Figure 3.1: Temporal structure of energy deposition in laser-induced breakdown

1.0 and 2.5 times the breakdown threshold, which is indicated by the solid horizontal line. The upper and lower dotted lines indicate laser power range that may or may not induce breakdown. With the laser peak-power value located between these two limits, only certain a percentage of incident laser pulses induces gas breakdown. The threshold value of optical breakdown is defined as the laser power at which half of the incident laser pulses induce significant energy absorption and cause breakdown. According to our observations of Nd:YAG laser-induced breakdowns, this energy range is about 20 to 35% of the threshold value for both air and ammonia flow breakdowns. The energy absorption process can start only when the laser power reaches this threshold range. Before the absorption starts, the front portion of laser energy transmits into the focal zone unperturbed. If the electron growth rate is very rapid compared to the laser pulse-width, the shaded area in the figure equals approximately the total deposition energy of the plasma. For incident laser pulses with a certain peak-power, the deviation of the absorption between independent laser-pulses results from the uncertainty of the initiation time. In the other words, absorption can start at any time as long as the laser power is in this range. When the laser peak-power is around the threshold value (as in the left plot in Figure 3.1), this uncertainty of absorption energy is very large, and the difference of initiation time between breakdowns can be as long as 3 $nsec$. For higher incident laser power, the absorption starts earlier and the process lasts longer, and the deviation of absorption energy reduces significantly.

### 3.1.1 Experimental Setups

The experimental setup for the study of energy absorption is shown in Figure 3.2. A pulsed Nd:YAG (Continuum YG680S) laser was used to create optical breakdown in air. The Nd:YAG laser is Q-switched and emits 6.5 $nsec$ (FWHM) laser pulses at 1.064 $\mu m$ and output energy of $\sim$ 100 $mJ$. To control the incident laser energy for the breakdown experiment, the laser beam was aligned to pass through a pair of polarizers. The adjustable angle between these two polarizers gave a well-defined output energy as shown in the Appendix. The laser beam was then expanded by two lenses to a beam-width about 2 $cm$. The optical breakdown was generated by focusing the expanded laser pulse using an antireflection coated 10 $cm$-focal-length lens. An energy-meter (Scientech. Model Number P50, calibrated for 1.06 $\mu m$) was used to detect the transmitted laser energy followed the breakdowns. The incident laser energy can be measured by rotating the focal lens a small angle (relative to the optical axis) to defocus slightly the beam to eliminate the breakdown and any significant energy absorption in the focal zone. A second energy meter (Laser Precision, Model Number RJP-734) was used to detect the energy of a small fraction of the laser beam at the beginning of light path. The simultaneous recording of laser pulse-energies using both energy-meters enables the readout of the second energy-meter to be translated to the absolute value of the incident laser energy by multiplying a constant ratio. When the focal lens was aligned to create laser breakdowns, the incident and transmitted pulse energies for each breakdown can be recorded simultaneously in a computer through GPIB. the fluctuation of the YAG laser output and the system- errors of both

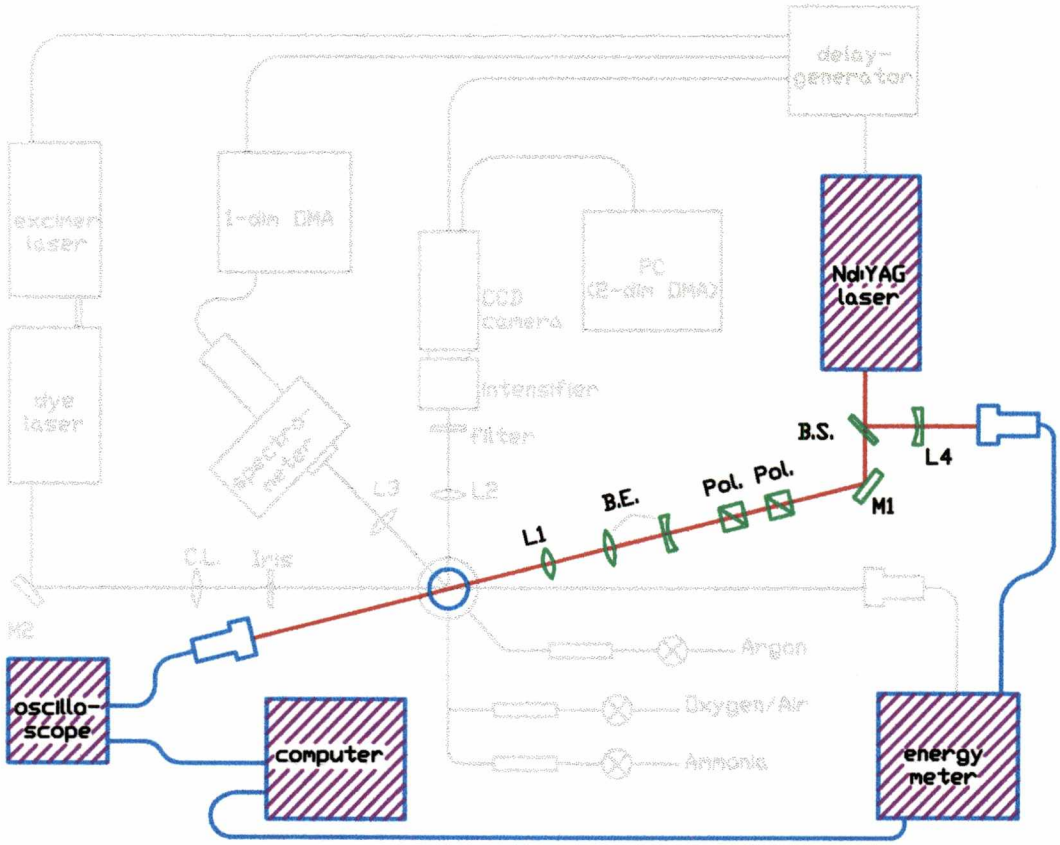



Figure 3.2: Experimental geometry in the study of energy absorption, B.S.= beam splitter, E1 = energy meter (Laser Precision, Model Number RJP-734), E2 = energy meter (Scientech, Model Number P50), M = mirror, Pol.= polarizer, B.E.= beam expander, L = lens

energy-meters were calibrated by recording energies of hundreds of laser pulses. The systematic errors of both energy meters were found less than 0.3 percent, and the fluctuation of Nd:YAG-laser pulse-energy was measured less than 1 percent.

### 3.1.2 Results and Discussion

Figures 3.3 and 3.4 show the experimental results of the incident laser-energies of thousands of pulses and the corresponding transmitted energies. The absorbed energies for the breakdowns are equal to the difference of incident and transmitted energies since significant scattering and diffracted light were not observed in the experiment. For all four plots in Figures 3.3 and 3.4, each plotted point, which corresponds to a fixed incident laser-energy ($\pm 1\%$), is the statistical result of the recording of more than 100 pulses. The error-bars show the deviations of these one hundred-plus pulses. In Figure 3.3(a), three energy regions with greatly different characters can be seen. For laser pulse-energy less than 11 $mJ$, no breakdown occurred. All the incident pulse-energy transmits through the focal zone, and the data points all reside on the dash-dot line (with slope=1, corresponding to the situation that no absorption or breakdown occurs). When the incident pulse-energies were larger than 16 $mJ$, all the laser-pulses caused significant absorption and created breakdowns. For the laser-pulses with energies between 11 and 16 $mJ$, only a certain fraction of pulses induced breakdowns (symbolized as circles), and part of them did not (symbolized as triangles).

The incident pulse-energy vs. the percentage absorption is shown in Figure 3.3(b). As the figure shows, about 50 % of incident energy was absorbed when the input

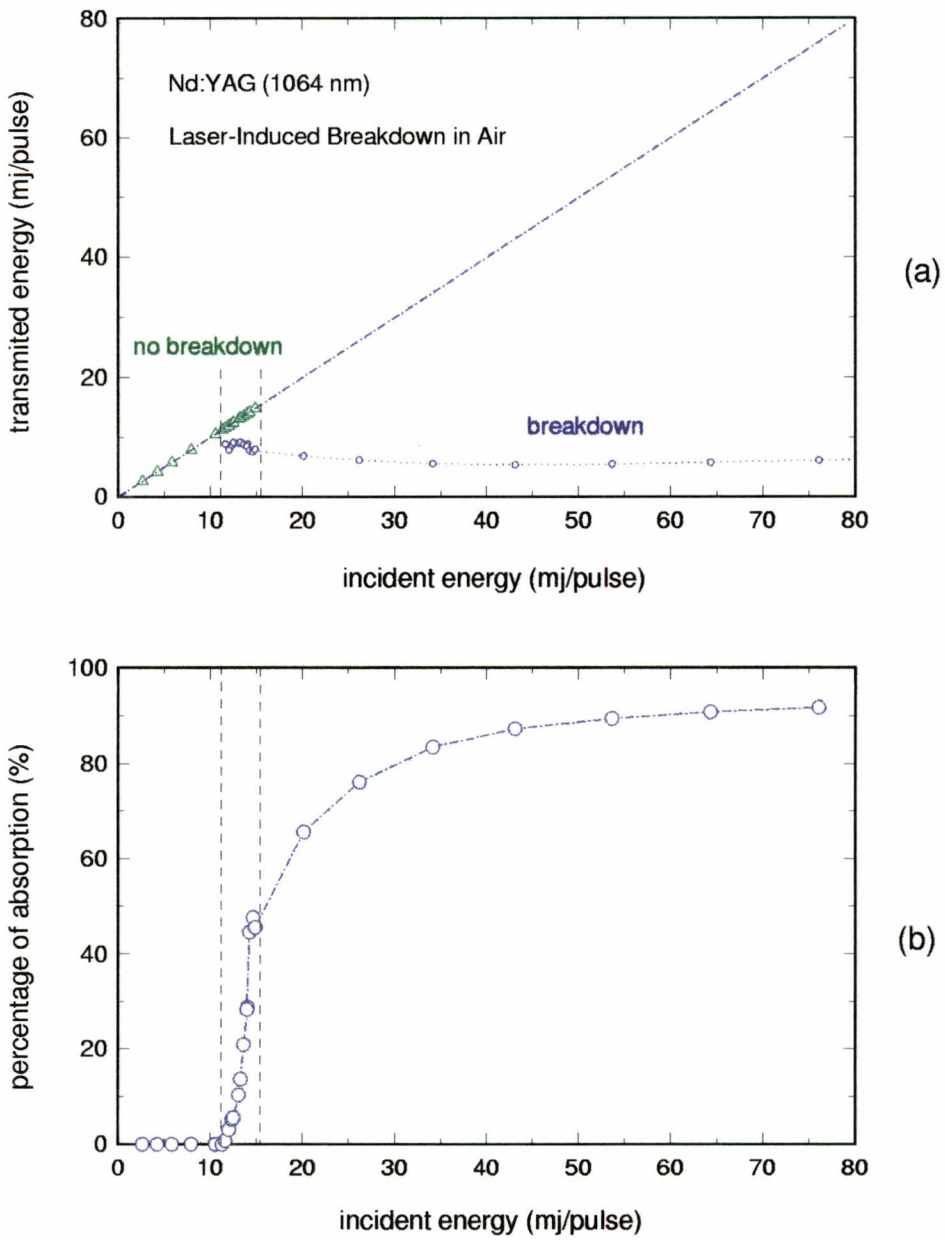



Figure 3.3: Energy-absorption study in laser-induced air breakdown

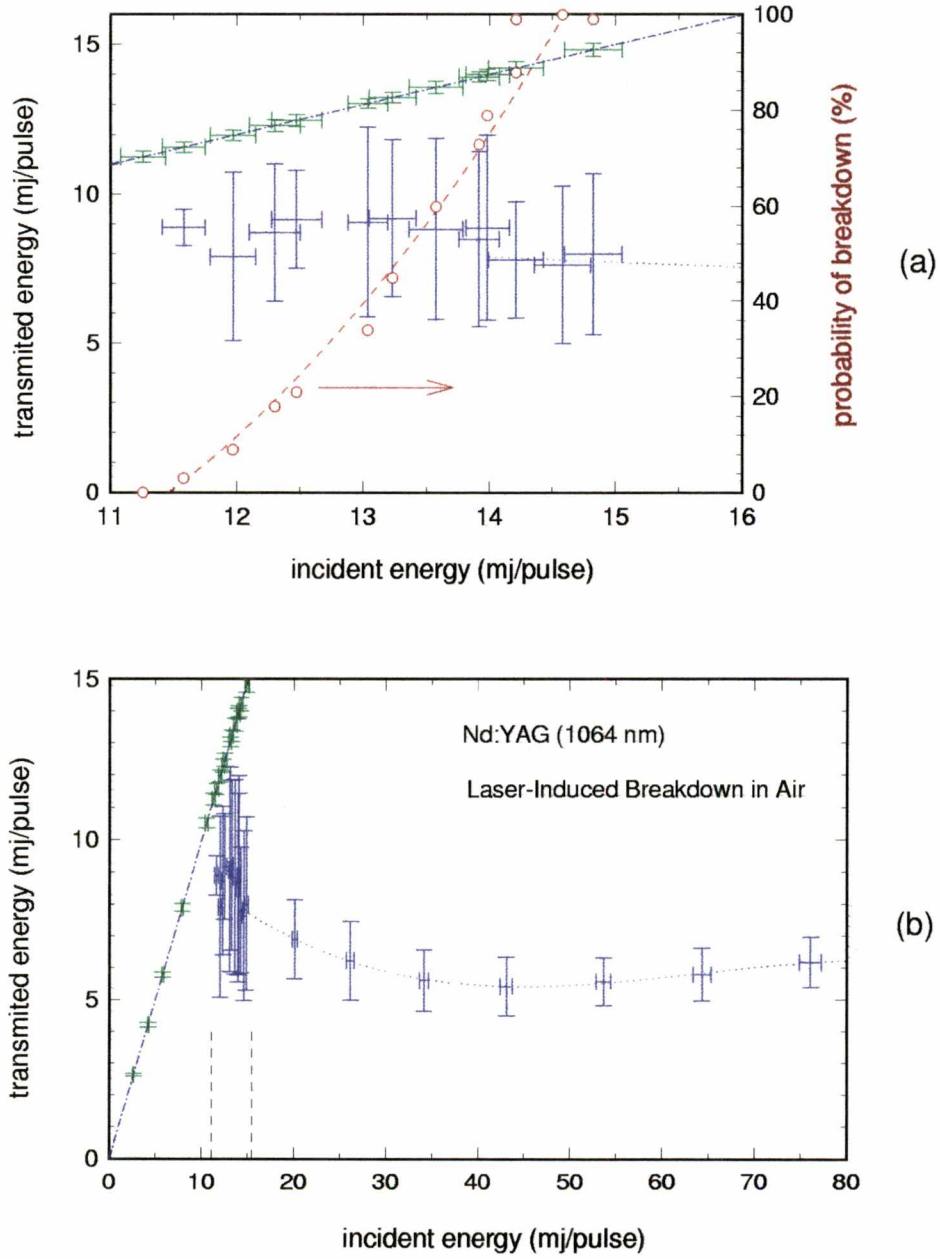



Figure 3.4: Energy-absorption study in laser-induced air breakdown

laser energy is just beyond the breakdown threshold range, which implies that following the initiation of breakdown, the free-electron grows to a highly absorbent density within a short period of time (approximately $1 \sim 2$ $nsec$). The electron growth rate, which depends on the laser irradiance, is then expected to be much faster than the reciprocal of laser pulse-width of 6.5 $nsec$ for a stronger laser excitation. Figure 3.4 is an enlargement of Figure 3.3(a) and shows the details of the absorbed energy and its deviation. First, we inspect the breakdown events with input pulse-energy inside the threshold range, between 11 and 16 $mJ$. In Figure 3.4(a), circle symbols are the probabilities of generating breakdown at a certain incident laser energy. Green crosses along the dash-dot line are those pulses that did not cause observable energy absorption in the focal zone. For pulses which caused breakdown (illustrated as blue crosses), the deviations of the absorbed energy were huge compared to their average absorption. If the initial electron in the breakdown process is produced when the local laser irradiance reaches a certain value with small deviation, the absorbed energy will not exhibit such a great fluctuation. The threshold value of the optical breakdown under our experimental conditions is clearly dominated by the creation of the initial electron, which happened to be a stochastic event over the threshold range. Although the multimode structure of the Nd:YAG laser used in the experiment could cause the deviation of the initiation time, this fluctuating behavior is quite common in long-wavelength laser-induced breakdown measurements [43, 44, 45, 46, 47]. It was discovered that the cascade type of optical breakdowns is mostly initiated by aerosols and impurities in the focal zone under atmospheric pressure [45, 46, 47]. With a laser irradiance that is two to three orders less than the breakdown threshold of pure gas

molecules, the particles of aerosols or impurities can sometimes be heated up to create electrons by thermionic emission.

In Figure 3.4(b), as the laser pulse-energy increases from 16 to 80 $mJ$, we observed that the fluctuation of the absorbed energy (i.e. the error-bars) continuously decreases, indicating a narrowing of the initiation time distribution. However, after the total transmitted energy decreases with the increasing of the input energy, it starts increasing around 45 $mJ$ of laser pulse energy. It is likely that saturation of the plasma absorption occurs around three times the breakdown threshold value. A small amount of laser energy in the rear portion of laser pulse transmits through the high-density hot plasma. The saturation of laser-induced plasmas has been observed and reported in the measurements of number density of free electron and plasma temperature respectively [18, 48]. As the reports state, when more energy is deposited into the plasma, the induced-plasma tends to expand its size instead of getting hotter or denser. The observation of the increase of transmision energy predicts more significant saturation behavior with higher incident laser irradiance ($>> 3\times$ threshold). The expansion in plasma size, which is very possibly a result of the plasma propagation as will be discussed in the followed section, reduces the degree of saturation in the energy absorption process in our experiment.

## 3.2 Images of Energy Deposition Process

In this section, the images of spontaneous radiation in the earliest stage of laser-induced plasma in air are examined. The spatial structure of energy deposition is shown in Figure 3.5. The laser beam is focused from the left-hand side into the

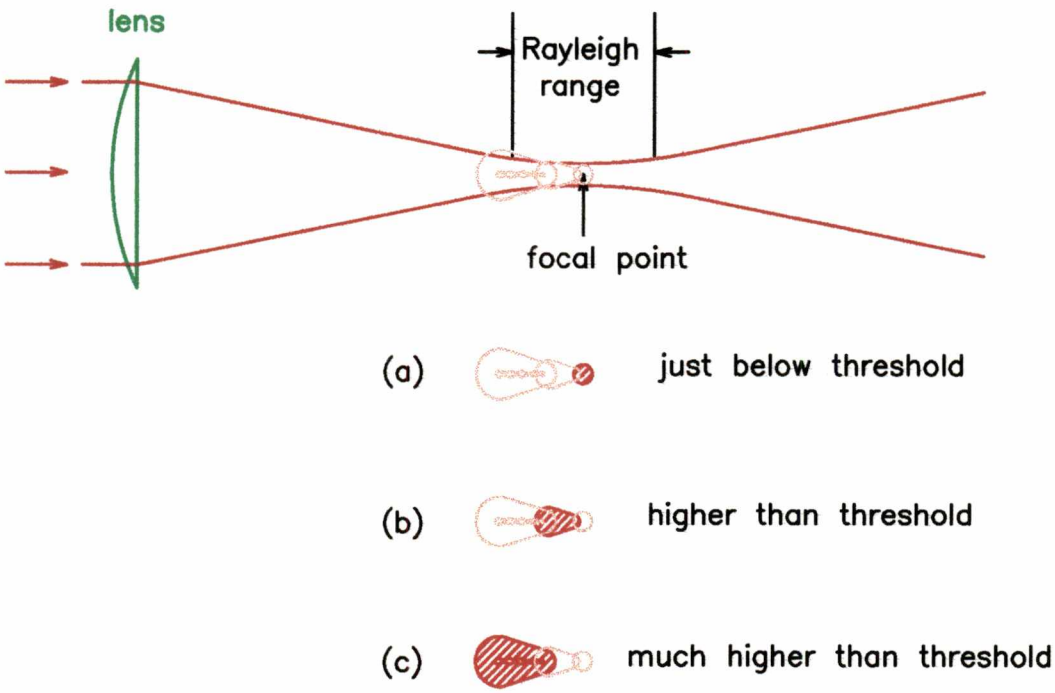



Figure 3.5: Spatial feature of energy absorption in laser-induced air breakdown

focal zone. The local laser irradiance across the focal area is proportional to the reciprocal of the laser-beam size. If the incident laser energy is higher than the breakdown threshold, then the breakdown can be initiated earlier at a location before the pulse reaches the focal point. The higher the incident energy is, the farther the initial plasma moves away from the focal point. If the laser power is lower than the threshold value (inside the threshold range, of course), the induced plasma should appear really close to the focal point.

### 3.2.1 Experiment

The experimental arrangement is shown in Figure 3.6. The Nd:YAG laser system and the optics used to induce plasma in air were the same as described in the previous section. An additional two-dimensional imaging system was used to take the spontaneous emission images of the induced plasmas in a near-perpendicular direction, 76° with respect to the optical axis of the laser beam. This system included a two-inch diameter quartz lens of 100 *mm* focal length, a neutral density (ND=1.5) filter placed in front of an intensified gated-CCD camera (EG&G PARC, model 2000 OMA SPEC) that was sensitive over the visible and UV range. The two-dimensional optical multichannel analyzer (2-D OMA) was used to control the operation of the CCD camera with an exposure resolution of 5 *nsec*. A DG535 delay generator controlled the timing between the Nd:YAG laser and imaging system. The overall temporal resolution of the image-delay between YAG laser pulse and camera images was 1 *nsec*. The spatial scale of images was calibrated using a two-dimensional grid pattern placed at the location of the breakdown kernel. The spatial resolution of images in both

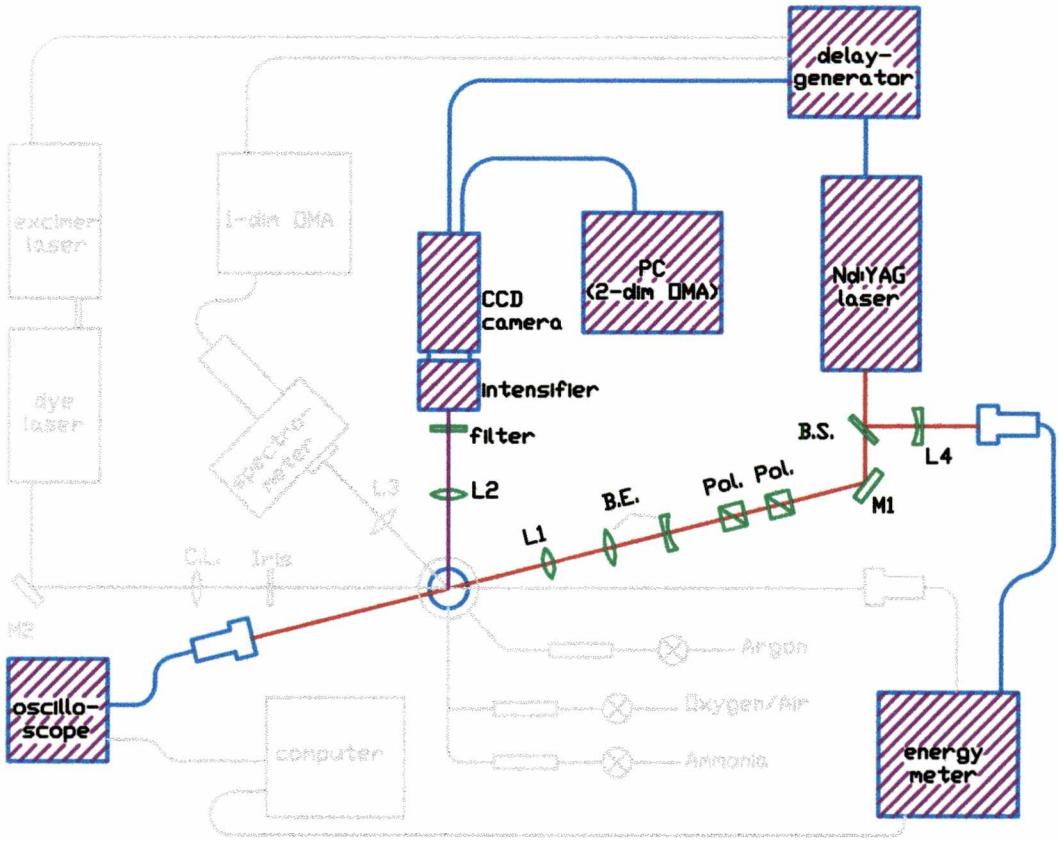



Figure 3.6: Experimental geometry in the study of energy absorption, B.S.= beam splitter, E1 = energy meter (Laser Precision, Model Number RJP-734), E2 = energy meter (Scientech, Model Number P50), M = mirror, Pol.= polarizer, B.E.= beam expander, L = lens

horizontal and vertical directions were found to be about 8.5 $\mu m$.

### 3.2.2 Results and Analysis

Figures 3.7, 3.8 and 3.9 illustrate a sequence of spontaneous emission images of breakdowns with the incident laser pulse energy of $\sim 42\ mJ$, for which the absorbed energy was $\sim 36.5\ mJ$. Each image in the figures was recorded from an independent breakdown event with the delay-time difference of 1 $nsec$. The laser beam was incident from the left-hand side, and all the image sizes correspond to 1.31 $mm$ in horizontal and 0.49 $mm$ in vertical directions. In both figures, two vertical lines are plotted as a reference distance of 0.5 $mm$. In each false-color image, the intensity gradient is illustrated from 60 % (blue color) to 97 % (pink) of its maximum intensity to reveal the core structure of the plasma. The recorded breakdown images in the experiment were very repeatable, and the images show that the initial plasma expands (or propagates) opposite to the laser's incident direction. Along the optical axis, the most intense radiation areas of the plasma appear in discrete regions. The separation of the local maximum intensities are clearly seen in the images of delay time of 3, 4 and 5 $nsec$, and this discontinuity is, indeed, present in every recorded image in Figures 3.7 and 3.8. While taking these images, the camera, a 2-D OMA system, was operated far beyond its saturation range, and this discontinuity was also observable in the breakdowns induced by different input laser energy (e.g. 16 and 80 $mJ$). The separation between these discrete spots of brightness is about 0.09$\sim$ 0.18 $mm$, which is very possibly a result of the focusing hot spots from optical lens L1 and the Nd:YAG laser beam. To examine this hypothesis, the aberration pattern of a focused Gaussian-

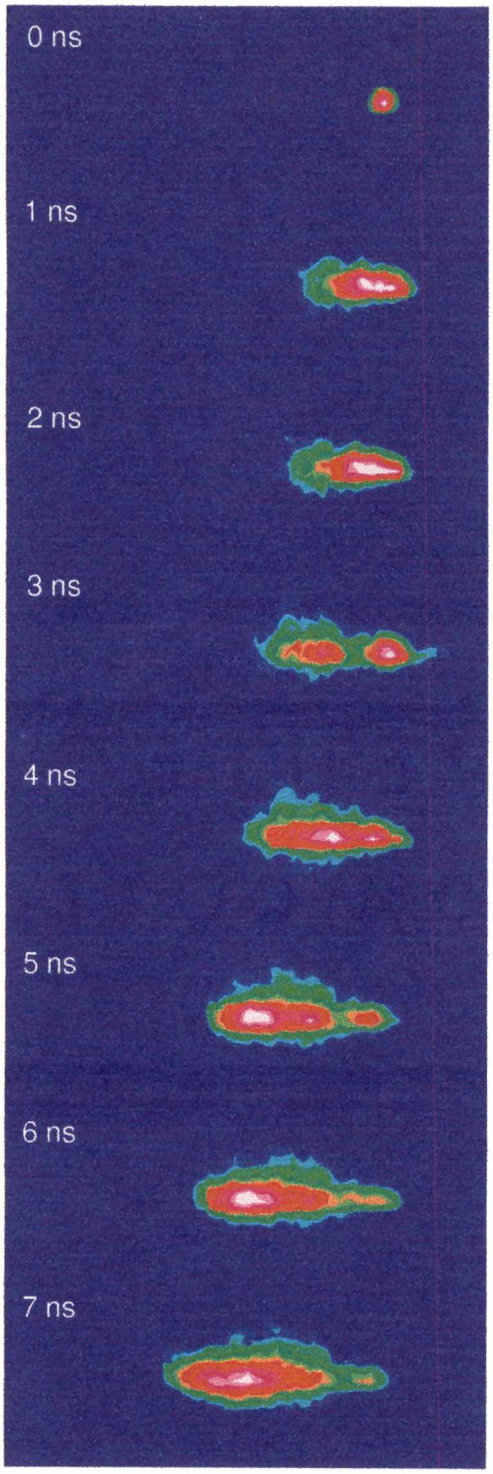



Figure 3.7: Images of energy deposition process in laser-induced air breakdown

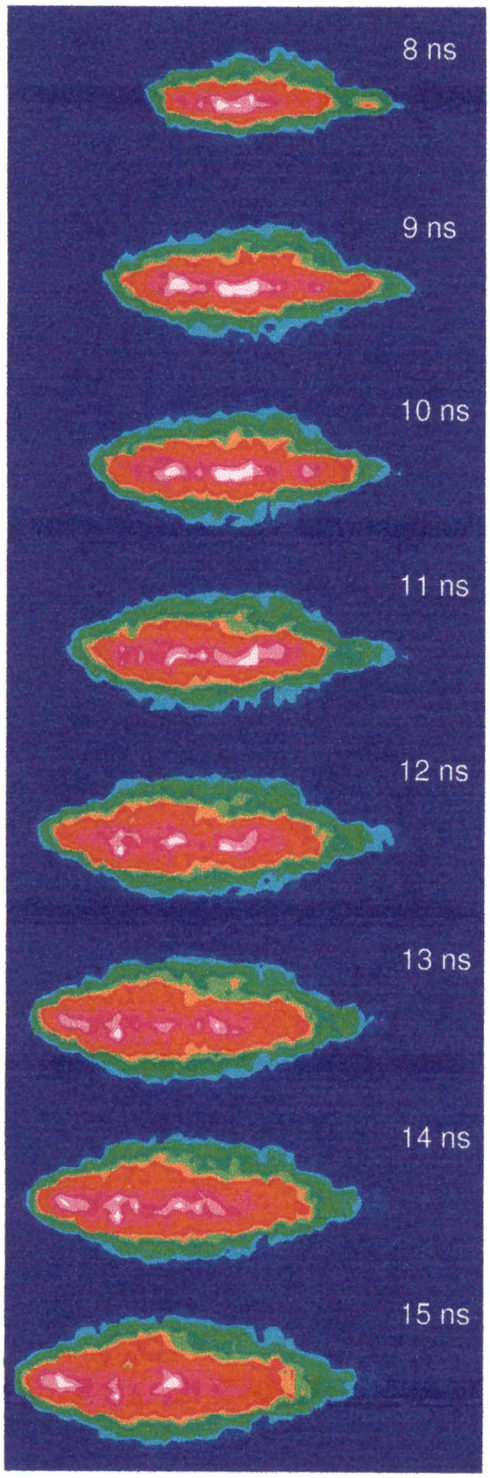



Figure 3.8: Images of energy deposition process in laser-induced air breakdown

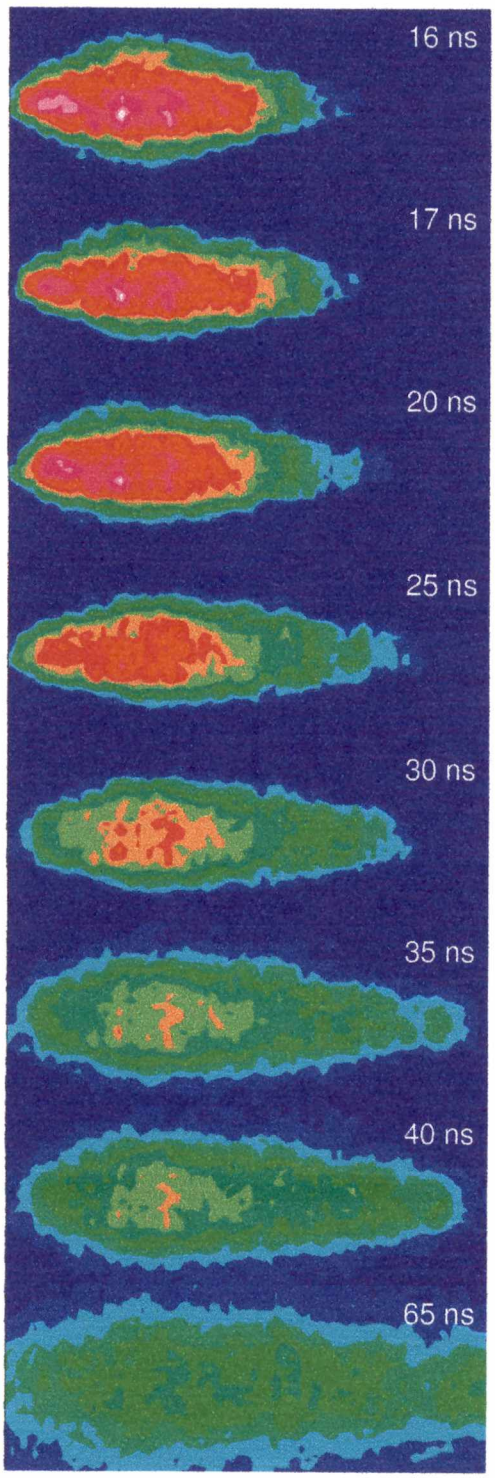



Figure 3.9: Images of energy deposition process in laser-induced air breakdown

beam with the beam-size of 2 $cm$ and wavelength of 1.06 $\mu m$ by a plano-convex lens was calculated [49, 50] and is shown in Figure 3.10. Along the optical axis, the laser intensity is integrated with diameters of 5, 10, 20, and 30 $\mu m$, and the average intensities are shown in the plot. Although, the multimode beam structure of Nd:YAG laser pulse is far from the ideal Gaussian beam used in the calculation, the calculated pattern shows the intermittent structure with the separation of brightest spots about 0.07$\sim$ 0.16 $mm$ as well.

Other than the breakdown images of the energy deposition process shown in Figure 3.7 and 3.8, experiments were also carried out for laser pulse energies of 12.1, 16.3 and 80 $mJ$. Relative to the breakdown threshold value of 13.4 $mJ$, each of these pulse energy values was chosen for obvious reasons (see Figure 3.3 and 3.4). For input energy of 12.1 $mJ$, only $\sim$ 20% of laser pulses induced breakdowns, and only 1 to 4 $mJ$ were absorbed from the laser pulses. For such a low energy absorption, the plasma propagation was not observed. When higher laser energies were applied to induce breakdowns. the locations of initial plasmas moving toward the left (lens side) slightly with the initiation times shifted earlier and with longer absorption periods were observed. In contrast to the 16.3 $mJ$ breakdown images (absorption 7$\sim$9 $mJ$), the 80 $mJ$ laser pulse (absorption $\sim$ 74 $mJ$) initiated the breakdown approximately 4 $nsec$ earlier at a location shifted 89 $\mu m$ to the left. The initiation positions of air breakdowns for laser pulses with the same energy were very stable from shot-to-shot and varied by less than 10 $\mu m$.

The plasma propagation was observed for 16.3, 42 and 80 $mJ$ excitations. With a laser energy of 16.3 $mJ$, the propagation speed was observed to be approximately

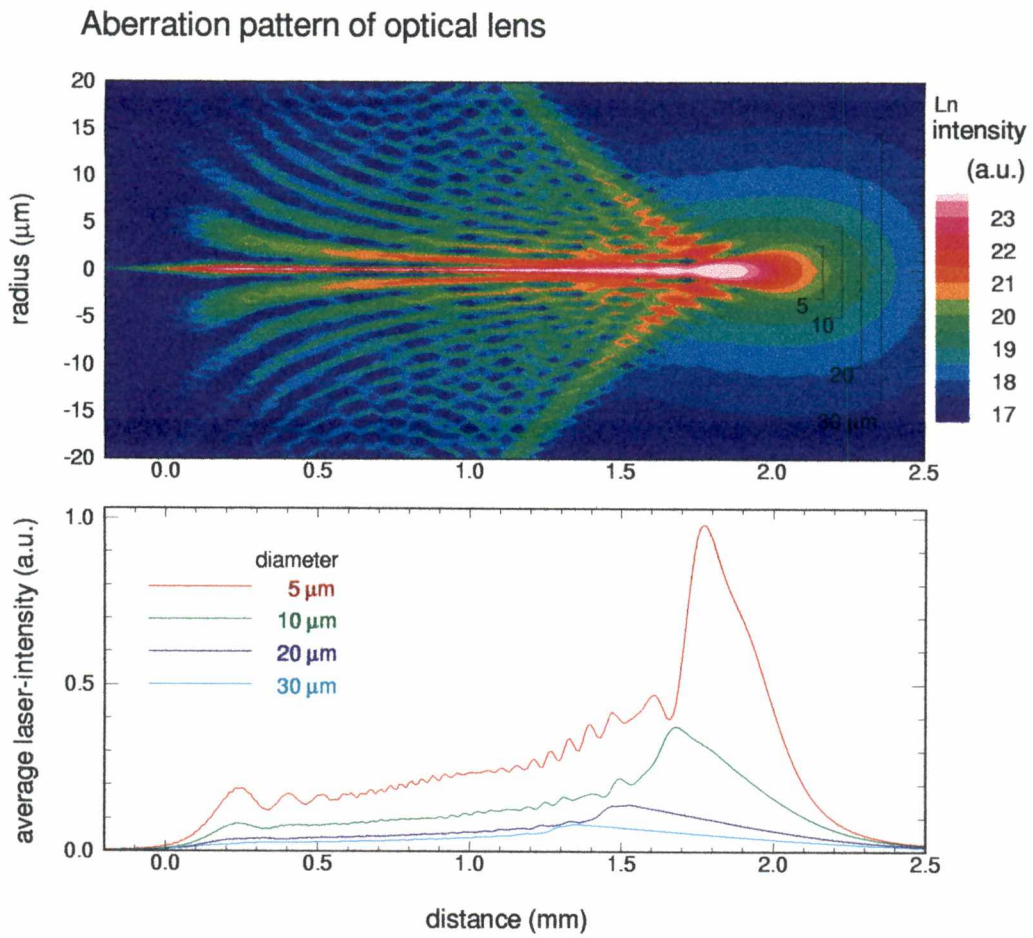



Figure 3.10: Calculated aberration pattern of a Gaussian laser beam focused by a 100 *mm* focal length, plano-convex lens

48 $km/sec$ at the first 5 $ns$, and it decreased to $\sim$ 20 $km/sec$ at later time. For the laser breakdowns with 42 $mJ$ incident energy, the plasma propagated with a uniform speed of $\sim$ 80 $km/sec$ through the first 12 $ns$ (see Figure 3.7 and Figure 3.8). As the laser energy increased to 80 $mJ$, only a trivial increase in propagation speed ($\sim$ 3 $km/sec$) was found. Along with the observation of absorption saturation from 42 to 80 $mJ$ in the previous section, this small increase of propagation speed seems to indicate the involvement of new absorption or energy-loss mechanisms for the additional deposited energy.

As discussed in Chapter 2, the propagation speed of the induced plasma depends on the laser irradiance in the plasma front. For a laser irradiance greater than one $GW/cm^2$ as in our experiments, the plasma propagates as a laser-supported radiation wave (LSR). For the special case of 12.1 $mJ$ laser excitation in our measurement, the laser pulse ended before it was able to support the plasma propagation. The energy absorption rate for LSR plasma is very rapid so that the breakdown is initiated without significant density change and the high-temperature high-pressure plasma is formed much earlier than the arrival of shock wave. The supersonic propagating plasma wave is supported by, primarily, the spontaneous radiation of hot plasma that is formed earlier. This type of problem is normally treated in quasisteady approximation (constant density) since the gas-dynamic processes do not play an important role in such a short period [31]. The plasma temperature and propagation velocity roughly scale as:

$$T \propto I_L^{\frac{1}{\beta+4}}, \tag{3.1}$$

$$V \propto I_L^{\frac{4}{\beta+4}}, \tag{3.2}$$

where $I_L$ is the laser irradiance and $\beta$ is around 1.6 for the multiply ionized gases. Using the scaling laws to scale the numerical results of 104,500$K$ and 10 $km/sec$ from one dimensional modeling for air breakdown with laser beam of 1.06 $\mu m$ and irradiance of 1.0 $GW/cm^2$ obtained by Bergel'son [51], the temperatures and propagation speeds for various laser irradiances have been computed and listed below:

| $I_L(GW/cm^2)$ | T $(K)$ | $V(km/sec)$ |
|---|---|---|
| 1.0 | 104,500 | 10. |
| 2.5 | 123,000 | 19. |
| 10. | 158,000 | 51. |
| 15. | 169,500 | 69. |
| 20. | 178,400 | 85. |
| 30. | 191,800 | 114 |

For the focusing geometry in our experiment, the laser beam diameter varies from 260 to 30 $\mu m$ (left to right) across the images shown in Figure 3.7 and 3.8. The laser irradiance is therefore, approximately ten to hundreds of $GW/cm^2$ (assuming a rectangular laser pulse with 6.5 $nsec$ pulse width). Under such a high laser irradiance, the plasma propagation speed is expected to be faster than 100 $km/sec$. However, with this extremely high value of laser irradiance, the geometry factor (radius to length ratio) is important in LSR plasma propagation due to the dilution of radiation support along the axis direction. According to Raizer's evaluation for laser irradiance as high as 200 $GW/cm^2$ in a small beam radius of 100 $\mu m$, the plasma propagation is just 100 $km/sec$, with the temperature of 75,500 $K$ which is in good agreement with the observed values [28, 52, 53]. The magnitudes of plasma propagation speeds in our experiment are in reasonable agreement with their evaluations.

# Chapter 4

# Laser-Induced Breakdown in the Flow Field

In this chapter, we continue the study of the formation of laser-induced breakdowns. The investigation emphasizes the effects on the breakdown that are related to the flow speed of the gases. Although the effects of the flow speed, which is less than 10 $cm/sec$ in our experiments, should be negligible within the extremely short time periods of formation ($\sim ns$) and decay ($\sim ms$) of the plasma kernel, some factors associated with the flow speed can affect the generation and properties of the breakdown kernel. In fact, we found the flow speed to be a major cause of the observed variation of the created plasma kernels. Both the physical and chemical properties of plasma are affected by the flow rate, and when applied to a combustible gas mixture, the influence of gas flow-speed causes significant effects on the laser-ignition process.

## 4.1 Threshold of Laser-Induced Breakdown

The breakdown threshold for the incident laser irradiance is defined to the area power density at which fifty per cent of laser shots results in breakdown of the (gas) sample. The definition of breakdown itself is more ambiguous, but the detection of the optical

spectral features of a laser-generated plasma is used as the operational definition and measure of the breakdown event. Once the plasma is formed, the plasma and chemical processes follow and, in general, combustion results for a fuel/oxidizer mixture. Two difficulties occur in the experimental study of laser ignition of reacting species. First, the breakdown process, as defined, is a stochastic phenomenon, and, as a result, fluctuation can occur in all subsequent processes. Second, the initiation and formation of the reacting species and combustion products can exhibit dependencies, or variations, on not only the breakdown event and the magnitude of absorbed laser energy but also on the nature and state of the gas sample. For example, the flow speed of the gas will be a factor in determining whether the flow field is laminar or turbulent, and the effect of turbulence intensity on the ignition process is not well understood. Also, a very low flow-speed can result in metastable remnants of the prior laser shot being present in the focal region for subsequent laser shots, thereby altering the breakdown process and the subsequent plasma chemistry reactions. Because of these reasons, the characterization of the breakdown threshold for the ammonia and ammonia-mixtures of this study is essential.

The values of the breakdown threshold in various gases have been measured and reported in numerous articles, and a few of the typical values of measurements are listed in the following table:

| author/year | pressure ($atm$) | wavelength ($\mu m$) | pulse width ($ns$) | gas | threshold ($GW/cm^2$) |
|---|---|---|---|---|---|
| Kroll, Watson/'72 | 1.0 | 10.6 | 100 | air | 3 |
| Brown, Smith/'73 | 1.0 | 10.6 | 100 | air | 3 |
| Yablonovich/'74,'75 | 1.0 | 10.6 | 100 | filtered $N_2$ | $1\sim 8\times 10^3$ |
| Dewhurst/'78 | .03~10 | .53,.69,1.06 | $\sim 10^{-2}$ | $N_2$,$O_2$ | $10^4 \sim 10^6$ |
| Armstrong et al/'83 | 1.0 | 1.06 | 30 | $N_2$ | 200 |
| Yosr, Gamal/'83 | 13.0 | 1.06 | 10 | $N_2$ | 60 |
| Williams/'85 | 1.0 | 0.53 | $\approx 10^{-1}$ | air | $\sim 10^5$ |
| Yosr, Gamal/'87 | 1.0 | 1.06 | 10 | $N_2$ | 200 |
| Plemmons/'96 | 1.0 | 1.06 | 3.5 | air | 280 |
| Plemmons/'96 | 1.0 | 1.06 | 3.5 | $NH_3$ | 170 |

The creation of optical breakdown requires the growth of free electrons to reach some certain density before the termination of the laser pulse. In some cases, the generation of an initial electron is the bottleneck of the whole process. As discussed in Chapter 2, the probability of creating an initial electron depends on the wavelength, pulse-width, and the mode structure (degree of coherence) of the laser, the existence of aerosols and impurities, the ionization energy of the gases and the gas pressure. After the appearance of the initial electron, the electron density increases at a rate which depends on the wavelength and irradiance of the laser and the pressure of the gas. For picosecond laser-induced breakdown, the threshold value is very high due to the time limit for electron growth (see Dewhurst/'78 and Williams/'85). Under such high irradiance requirements, the gas pressure and laser pulse-width play important roles of the threshold value.

At atmospheric pressure, with the use of nanosecond-lasers, the threshold value of avalanche-type breakdown is strongly determined by the creation of the initial electron. Yablonovich (1974, 1975) showed that, by eliminating impurities and filtering out particles larger than 0.1 $\mu m$, which are normally the source of initial electrons,

he could increase the threshold value by more than two orders of magnitude. Therefore, the properties and quantities of the impurities and aerosols are commonly the dominant factors of the threshold value. The laser pulse-width, in the other hand, is not influential under this circumstance.

### 4.1.1 Experiment

Using the experimental apparatus shown in Figure 4.1, the laser-pulse energy thresholds required for breakdown of $NH_3$ and air were determined. The conversion of these results to the threshold irradiance requires accurate determinations of the laser pulse-width and focal diameter, and this conversion is discussed and presented in a subsequent paragraph. For the purpose of the task at hand, only the energy threshold data were required, and the breakdown phenomenon was investigated using a range of gas flow-speeds and laser repetition rates.

As illustrated in Figure 4.1, the experimental setup for the threshold measurement was the same as in the studies of energy absorption in previous chapter except for the use of a burner and the flow-control system. The research-grade anhydrous ammonia or air was flowed through a McKenna Products flat-flame burner. The diameter of the burner is 6 $cm$ and is made of sintered stainless steel. The laser pulses were focused into the center of flowing gas at a height of approximately 10 $mm$ above the burner surface. The flow rates of two gases were individually monitored by calibrated MKS flow meters (see Appendix). For $NH_3$ breakdowns, data were acquired using the laser repetition rates of 2 and 10 $Hz$ and for $NH_3$ flow-speeds over the range of $1.0 \sim 6.0$ $cm/sec$. Further, data were acquired at the vertical positions of 10 and 30 $mm$

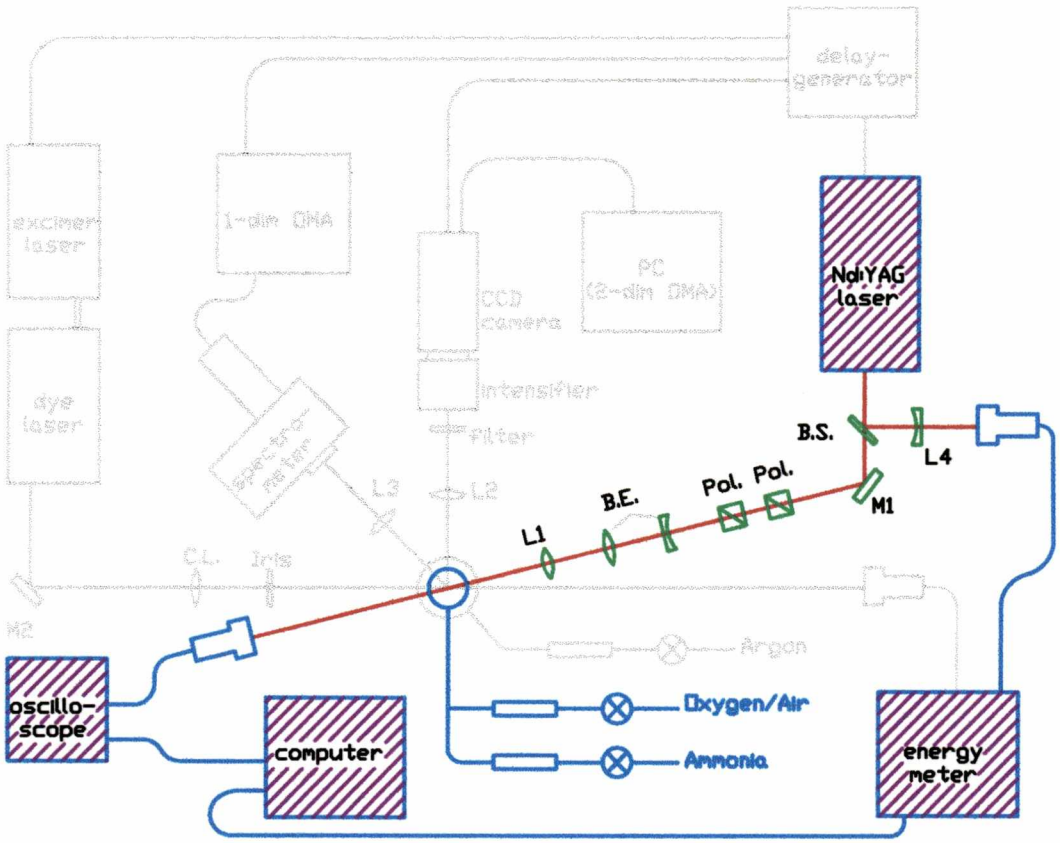



Figure 4.1: Experimental geometry in the study of threshold, B.S.= beam splitter, right energy meter: (Laser Precision, Model Number RJP-734), left energy meter: (Scientech, Model Number P50), M = mirror, Pol.= polarizer, B.E.= beam expander, L = lens, flat-flame burner (McKenna, 316 stainless steel)

above the McKenna burner. Figure 4.2 shows the results of these measurements, and it is seen that the energy threshold is approximately 6.7 $mJ$ with an uncertainty of approximately 15 per cent. Further, the unit breakdown probability is asymptotically attained with a pulse energy of $9 \sim 10$ $mJ$.

A more detailed study of the variations of the data of Figure 4.2 was performed in the approximate energy range of $6 \sim 9$ $mJ$, and the results indicated systematic variations of these results with flow-speed, repetition rate, and breakdown location in the burner field. The subsequent paragraphs consider in detail these observed variations.

### 4.1.2 Results and Discussion

The variations of the probability of optical breakdown as a function of laser energy for $NH_3$ and air are shown in Figures 4.3 and 4.4(a). Figure 4.3 shows the results for $NH_3$ for two different laser repetition rates, 2 $Hz$ and 10 $Hz$, and Figure 4.4(a) compares the breakdown characteristics. Each recorded point of $NH_3$ and air for a fixed laser energy in Figure 4.3 was a statistical result of 200 laser pulses, and the curves of the figures are polynomial fits to the data. As stated previously, the threshold values are determined by the laser energy of each curve, which corresponds to a 50 percent-probability of breakdown. From the results, we first noticed that increasing the repetition rate of the Nd:YAG laser reduced the energy required to induce optical breakdown (from solid- to hollow-symbols in Figure 4.3(a)). This reduction at the higher frequency suggested the presence of residual, metastable molecules from previous breakdown events. The phenomenon can be observed in the breakdowns

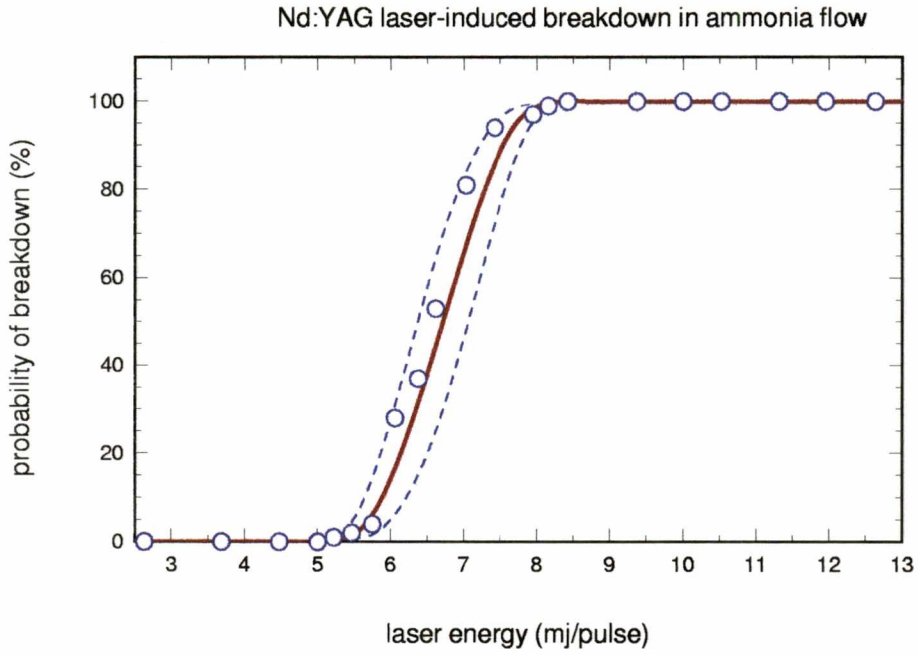



Figure 4.2: Threshold measurement in laser-induced breakdown in ammonia flow. flow-speed: 1.0 $cm/sec$, repetition rate: 10 $Hz$, location: 10 $mm$ above burner.

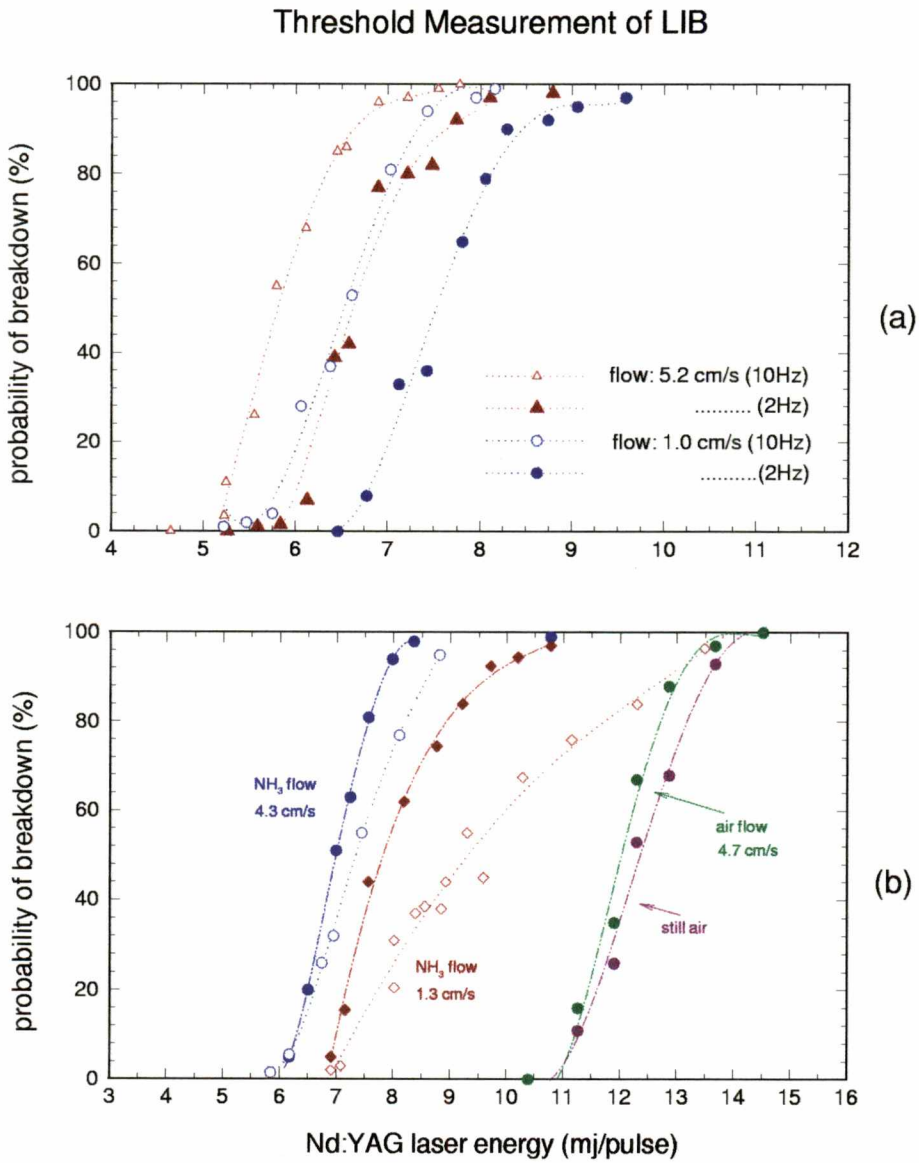



Figure 4.3: Threshold measurement in laser-induced breakdown in ammonia flow: (a) comparison between repetition rate of 2 and 10 $Hz$, (b) comparison of air and ammonia breakdowns. solid symbols: 10 mm above burner, hollow symbols: 30 mm above burner.

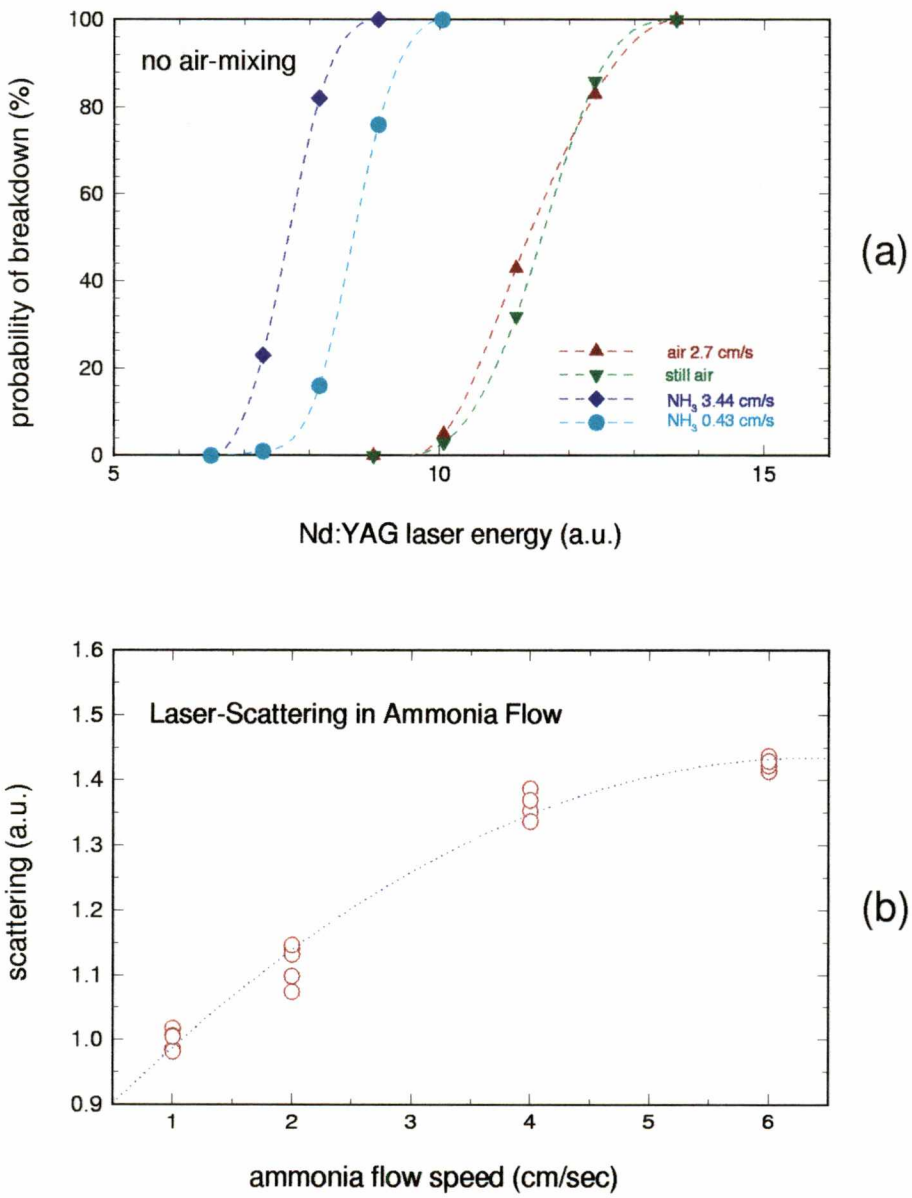



Figure 4.4: (a) Threshold measurement in laser-induced breakdown in ammonia flow without mixing with ambient air. (b) $90^o$ scattering of 340 $nm$ UV light in ammonia flow.

of ammonia, laboratory air, and oxygen flow-fields (examined at 2, 5 and 10 $Hz$). When trying to increase the flow-speed to eliminate the residual, or remnant, species from the previous breakdown event, which should increase the threshold value, the threshold curves were further reduced (from the blue circles to the red triangles in Figure 4.3(a)). It is clear that, along with the speed of molecules, the flow rate of ammonia has some effect on the breakdown-threshold.

In Figure 4.3(b), we compared the breakdown-thresholds of laboratory air and ammonia flow to examine the influence of the mixing of the gas-flow with ambient air. As shown in the figure, inducing the breakdown (or creating the initial electron) in the atmospheric-pressure ammonia gas requires less laser energy and is easier to achieve than in the air. The solid symbols in Figure 4.3(b) indicate the breakdowns that occur at 10 $mm$ above the burner surface, and the hollow symbols indicate the results at a height of 30 $mm$. With the increase of height of the focal volume above the burner, the ammonia breakdown curves tend toward the air results with the minimum required initiation energy staying around the same values. The ammonia curve of 1.3 $cm/sec$ flow at 30 $mm$ location shows the mixing nature clearly (symbols of hollow diamonds). The elongation of the threshold-curve occurred in the $NH_3$/air mixture (although, the amount of air may be trivial) implies and predicts a greater fluctuation of kernel formation between breakdown events, even using a much higher laser energy. With the increase of flow speed at the specified location, the degree of mixing with the ambient gas is reduced (symbols as blue-circle, from solid to hollow).

To eliminate the air-mixing effect in ammonia flow, experiments were carried out with the use of a quartz-cylinder (2-inch inner-diameter) above the burner surface

to confine the ammonia flow, and the results are shown in Figure 4.4(a). The data show that increasing the ammonia flow-speed clearly lowers the breakdown threshold. Therefore, gas mixing is not the only factor associated with the flow rate that affects the threshold value. The difference between ammonia flow at 3.44 and 0.43 $cm/sec$ in Figure 4.4(a) is very possibly a consequence of the presence of ammonia aerosol, or micro-droplets, that are produced by condensation of super-cooled ammonia as it expands in its passage through the valves of the system. As the ammonia flow-rate increased, the concentration of $NH_3$ aerosol droplets would be expected to increase more significantly than other commonly used gases due to its vapor-pressure properties and comparatively high condensation temperature. Elastic scattering of the laser-beam radiation was used to attempt to detect the presence of the presumed ammonia micro-droplets. It is known that this elastic scattering signal is sensitive to the droplet size and is proportional to the local density of the scatterers for optically thin media. For a droplet diameter $d$ and radiation wavelength $\lambda$, it is known that for the size parameter $X=\pi d/\lambda << 1$, Rayleigh scattering is the appropriate model, and for this case, the differential and total cross section varies as $d^6/\lambda^4$. For a specified $\lambda$, as the diameter increases, the size parameter X increases, and the total scattering cross section vary as $X^m$, where typically $m > 2$ for $X< 5$. Details of such scattering process are given by Reference [54]. If ammonia condensation and aerosol formation occurs as the vapor flow-rate increases and if such micro-droplet condensate increases with increasing flow-rate, the Rayleigh-Mie scattering signal should exhibit a corresponding increase, which will lend support to the condensation premise. To check this, an experiment was performed where ammonia gas was flowed through the

flat-flame burner with an argon shroud-flow to prevent air mixing and to stabilize the core flow. A vertically polarized UV laser-beam was injected into the region 1.0 $cm$ above the burner surface, and the scattered light was observed perpendicular to the beam axis. Figure 4.4(b) shows the dependence of elastic scattering light of an UV- (wavelength 340 $nm$) laser beam in various ammonia flow-rates. An increase of 45 % of scattering signal was observed as the $NH_3$ flow-speed increased from 1 to 6 $cm/sec$. The increase in Rayleigh/Mie scattering with the increase in flow-rate of $NH_3$ indicates the presence of scattering species other than molecular, gas-phase $NH_3$. Further, since this effect, as well as an increase in fluctuation of the $NH_3$ scattering signal, is not observed with air flows, it is most likely due to the condensation of $NH_3$ during the transfer from the $NH_3$ tank to the observation volume. It is desirable and possible to estimate the order-of-magnitude of the concentration of these possibly extraneous scattering species if one assumes the condensate droplets are monodisperse in size. An estimate of the size of this presumed condensate, microdroplet, or cluster is aided by the assumption that a reduction in the breakdown threshold by "particulates" requires that the particles exhibit the collective properties appropriate to either a liquid or a solid. In other words, it is reasonable to assume that the photoionization of a weakly bound, macromolecule with short-range order will not exhibit gross variations relative to the monomer in the breakdown threshold. It has been found that molecular clusters exhibit continuum properties when the number of molecules per cluster exceeds approximately $10^4$ [54]. If the cluster diameter were on the order of 0.01 $\mu m$, there would be approximately 30,000 molecules per cluster, which satisfy this criterion. Using Rayleigh scattering predictions, one can show that

the total scattering cross section, $\sigma_c$ for a liquid $NH_3$ droplet of 0.01 $\mu m$ diameter is

$$\sigma_c \sim 10^{-17}(cm^2), \tag{4.1}$$

where the liquid $NH_3$ index of refraction is assumed to be approximately 1.325. If the Rayleigh cross section of the $NH_3$ molecule is $\sigma_m$, for a 100 per cent increase in scattering,

$$\frac{(n_c\sigma_c)}{(n_m\sigma_m)} \sim 1, \tag{4.2}$$

where $n$ is the number density and $\sigma$ is the cross section and the subscripts $c$ and $m$ denote cluster and molecule, respectively. Then, if the total cross section, $\sigma_m \sim 10^{-26} cm^2$ [55]. one finds

$$\frac{n_c}{n_m} \sim \frac{\sigma_m}{\sigma_c} \sim 10^{-9}, \tag{4.3}$$

or the cluster mole fraction is on the order of ppb. For this size condensate, the mass fraction of liquid-phase droplets is then on the order of ppm. A similar conclusion, rather than using the index of refraction, results if one assumes the cluster polarizability is additive and computes the number and mass fraction of the cluster $NH_3$ condensate particles.

Using these results of cluster concentrations of ~ppb, it is seen that for a focal volume of $\sim 10^{-7}$ $cc$, one would expect to find within the laser focal volume a Poisson-distributed cluster sample of $\sim 1000 \pm 30$ for each laser shot. Therefore, for each laser pulse, aerosol microdroplets can be expected to exist within the focal volume with a high probability and comparatively small variance.

In Figure 4.5, we show a summary of the threshold measurement. Using an estimated focal diameter of 35 $\mu m$, the threshold of optical breakdown in laboratory

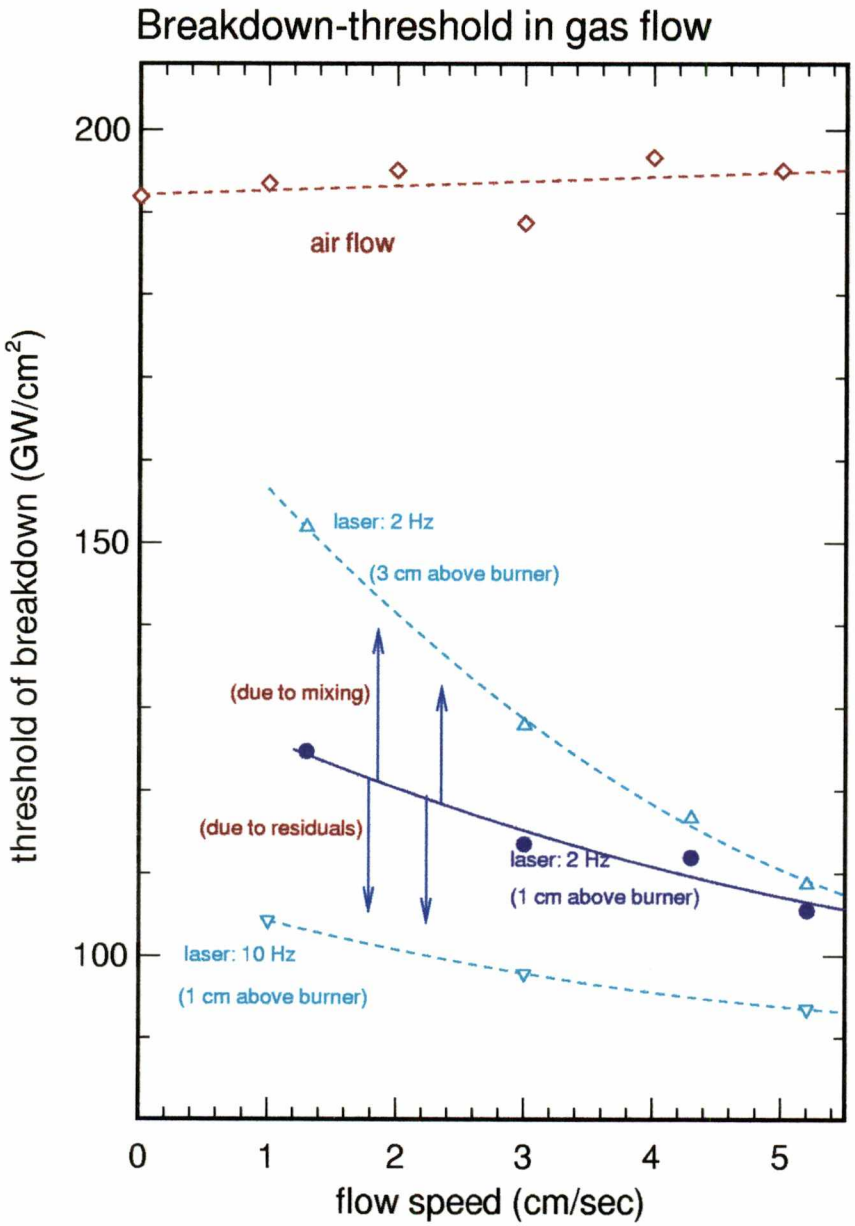



Figure 4.5: Breakdown-threshold measurement in air and ammonia flow.

air is measured approximately 190 $GW/cm^2$. The threshold of ammonia flow, however, decreases with the increasing flow speed as the postulated cluster concentration and size increases. When the effect of air mixing occurs, the breakdown curve tends to move toward the region of air (from solid-circles to up-triangles). That is, for slow flow speeds, mixing with the surrounding air increases, and the threshold values approach those of the entrained air sample. Finally, if remnant molecules from the previous breakdown are in the focal region while next breakdown is initiated, the threshold decrease by 15 $GW/cm^2$ (from solid-circles to down-triangles).

## 4.2 Probability Distribution Function (PDF) of NH Density in Optical Breakdown and Ignition

From pulse to pulse, laser-created breakdowns in the flow fields are not as stable and repeatable as in the still laboratory air. The goal of the research here is to examine the distribution function of breakdown events under a certain flow condition. In these experiments, we simultaneously measured and recorded the absorbed energy and the chemical composition of a grouped of breakdown events. The measurement of energy absorption was performed as in the previous chapter. The laser-induced fluorescence (LIF) spectroscopic technique was used to detect the NH molecular concentration in the plasma kernel of ammonia breakdown and ammonia/oxygen ignition. Under the transient conditions, the fluorescence signal was acquired at a selected time delay, 5 $\mu s$ after the initiation of breakdown with gate-width of 100 $nsec$. Within the duration of 5 $\mu s$, NH molecules are formed primarily through the recombination

process inside the plasma kernel rather than by the combustion chemistry, which would take tens to hundreds of microseconds to produce a significant amount of NH. If the absorbed energies in a group of breakdown events are close enough, we assume that the plasma kernels have similar thermal structures, and the intensity of fluorescence is proportional to the concentration of the probed molecules.

### 4.2.1 Experiment

The experimental schematic is shown in Figure 4.6. The Nd:YAG laser was operated at a repetition rate of 2 $Hz$ in experiments of ammonia breakdown. The LIF probe laser is an excimer-pumped dye laser system. The pumping laser is the Lambda Physik EMG 150 MSC excimer laser, which has been filled with XeCl and produces 308 $nm$, 10 $ns$ pulses with approximately 60 $mJ$ per pulse. The dye laser is a Lambda Physik FL3002E with the oscillator and amplifier filled with p-terphenyl dioxane solution which lases in the spectral region around 340 $nm$. The spectral line width of dye laser pulses is approximately 0.15 $cm^{-1}$. The dye laser is focused by a cylindrical lens with focal length of 30 $cm$ into a sheet-beam, which slices across the center of the breakdown-kernel with an angle of 14° with respect to the optical axis of Nd:YAG laser beam. The wavelength of the dye laser is tuned to the resonance of a well-resolved rotational transition of the $A^3\Pi_i - X^3\Sigma^-$ system of NH molecules. The laser-excited NH molecules in the spatial cross section of the plasma kernel radiate UV fluorescence, which is detected by the intensified CCD camera with a 100 $ns$ gate, which overlaps the dye laser pulses, in the 90° direction. A narrow band-pass filter centered at 337 $nm$ with bandwidth of 10 $nm$ is used to reduce the radiation other

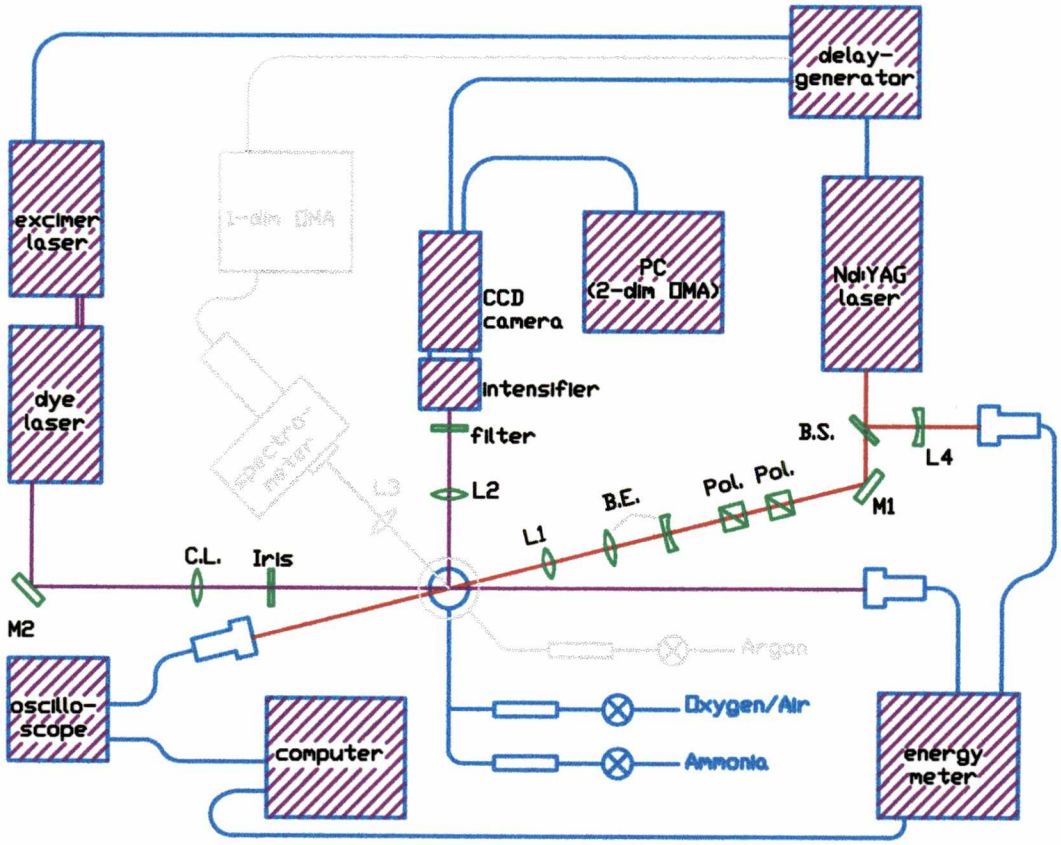



Figure 4.6: Experimental geometry in the study of threshold: B.S.= beam splitter, left energy meter (Laser Precision, Model Number RJP-734), right energy meters (Scientech, Model Number P50), M = mirror, Pol.= polarizer, B.E.= beam expander, L = lens, flat-flame burner (McKenna, 316 stainless steel)

than the NH fluorescence around 337 $nm$. Since the LIF signal is strongly wavelength-dependent, by tuning the dye-laser off the resonance of the NH spectral lines, the monochromatic background of elastic scattering such as Rayleigh and Mie scattering can be obtained and subtracted from the fluorescence signal.

### 4.2.2 Laser-Induced Breakdowns in Ammonia Flow

The spontaneous emission produced by the laser-induced breakdown is shown in Figure 4.7 as a function of wavelength for 0.35 to 10.35 $\mu sec$. The rapid decay of the emission, which is a background signal for the LIF data, is to be noted in the figure.

Figure 4.8 shows the probability distribution functions of NH concentration in breakdowns in ammonia flow. The flow-speed of ammonia was varied from 2.2 to 8.6 $cm/sec$. Energies of Nd:YAG laser pulses were around 20 $mJ$ per pulse. In each flow-speed and X-Y plot of Figure 4.8, 200 laser pulses were recorded. The abscissas are the relative intensity of NH fluorescence, and the ordinates represent the corresponding probability distribution function (pdf). The hollow-green vertical bars indicate the location of offset (fluorescence = 0), which are contributed mostly from the spontaneous radiation of plasma and the Rayleigh scattering of the probe laser. The solid-red vertical bars present the probability distribution of these 200 laser induced breakdowns. The figure shows that at low flow rates, about one-fifth of the laser-induced plasmas generate an immeasurable or a very low concentration of NH molecules, and the distribution function shows a two-peak structure with one peak located at the zero position. The two-peak phenomena, likely a consequence of the gas mixing with ambient air, gradually dissipate with the increase of flow rate.

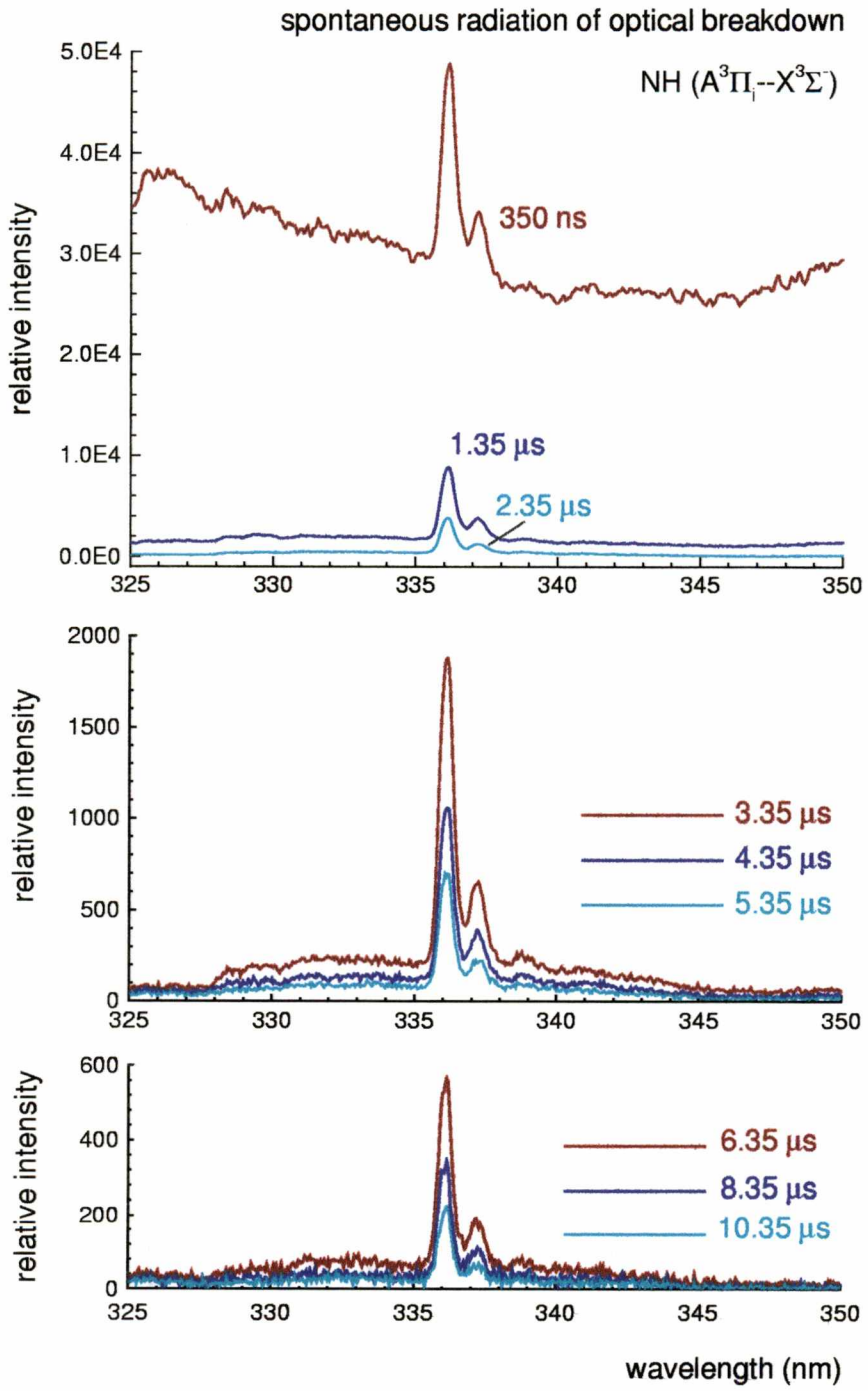



Figure 4.7: Spontaneous emission spectrum of laser-induced breakdown in ammonia flow.

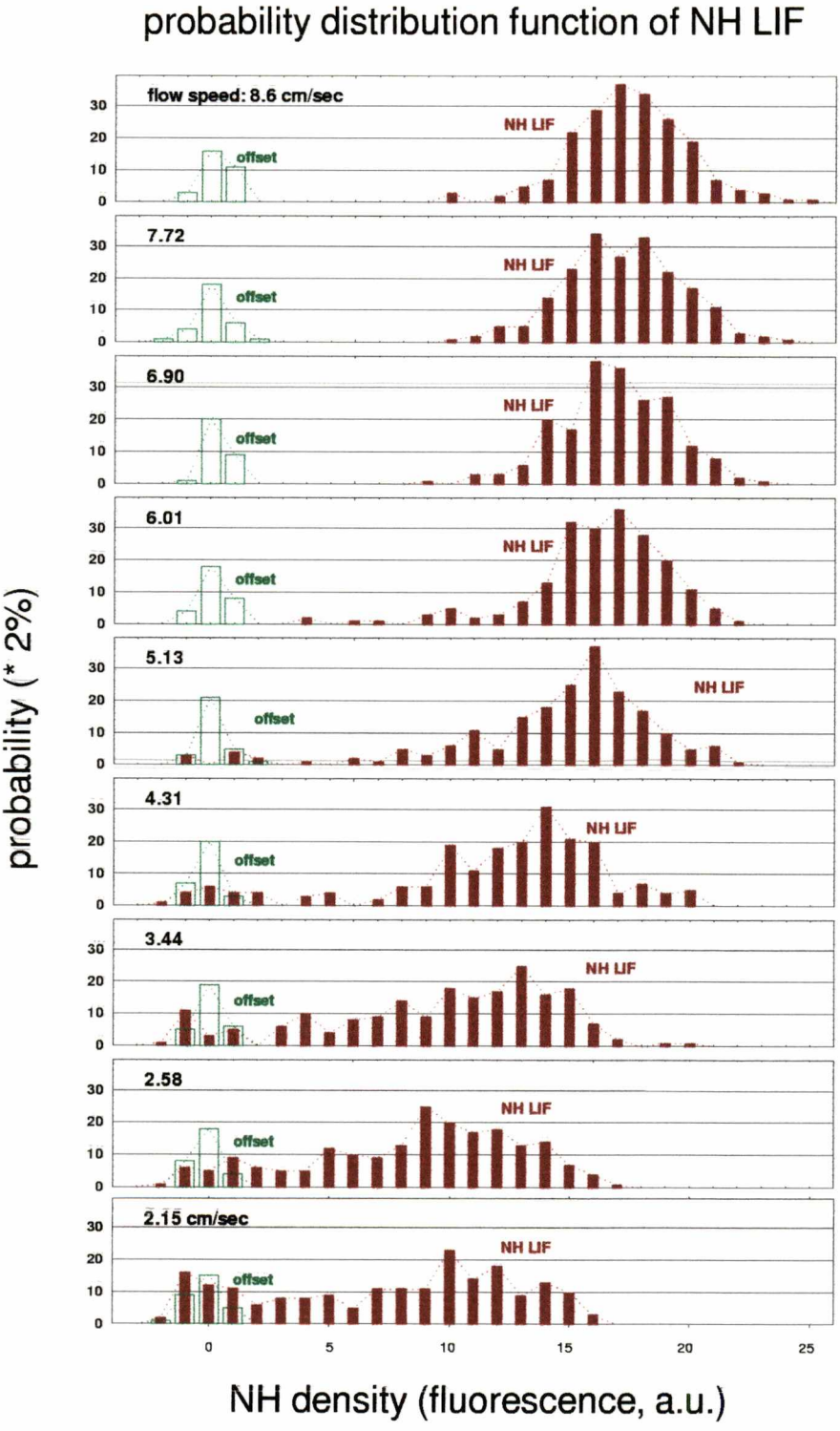



Figure 4.8: Probability distribution functions of NH concentration in ammonia breakdowns.

The breakdown threshold, as described in the previous section, reduces with the increase of flow-rate and is manifested by an increasing absorbed energy, the size of the initial plasma, and therefore, an increase in the NH density. In Figure 4.9, for an ammonia flow speed of 6.5 $cm/sec$, distribution functions are given for laser pulse energies of 11 and 21 $mJ$. The experiments using a quartz-cylinder standing above the burner surface were performed under very slow ammonia flow (see Figure 4.10). Without mixing with laboratory air, breakdowns present the normal single-peak distribution.

### 4.2.3 Laser Ignition in Premixed Ammonia/Oxygen Flow Field

Laser-breakdown and laser-induced ignition are both stochastic processes. Obviously, breakdown is required to achieve laser-induced ignition, but it was observed that breakdown was only a necessary and not a sufficient condition for ignition. It was of interest to see if there exist spectroscopic indications early in the plasma decay process that serve as predictors for subsequent ignition. To accomplish this, the NH fluorescence signal was observed 5 $\mu sec$ after the absorption and breakdown events in a pre-mixed ammonia/oxygen mixture of 4.5 $cm/sec$ flow-speed. Illustrated in Figure 4.11(a) is the NH signal for 550 individual laser pulses and the observation of a successful or failed ignition event. Another 60 laser-induced breakdown events were measured for off-resonant pumping of the probe laser to determine the magnitude of the background level. The background of the fluorescence signal includes the spontaneous radiation of plasma, which depends on the amount of absorbed energy, and the scattering from the probe laser. With a Nd:YAG laser pulse energy of 32

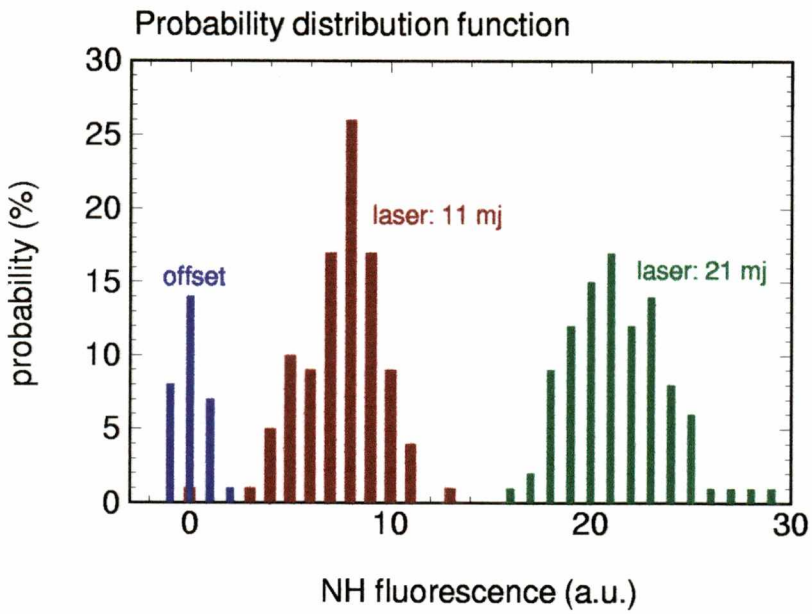



Figure 4.9: Laser-power dependence of pdf of NH concentration in ammonia breakdowns. ammonia flow: 6.5 $cm/sec$.

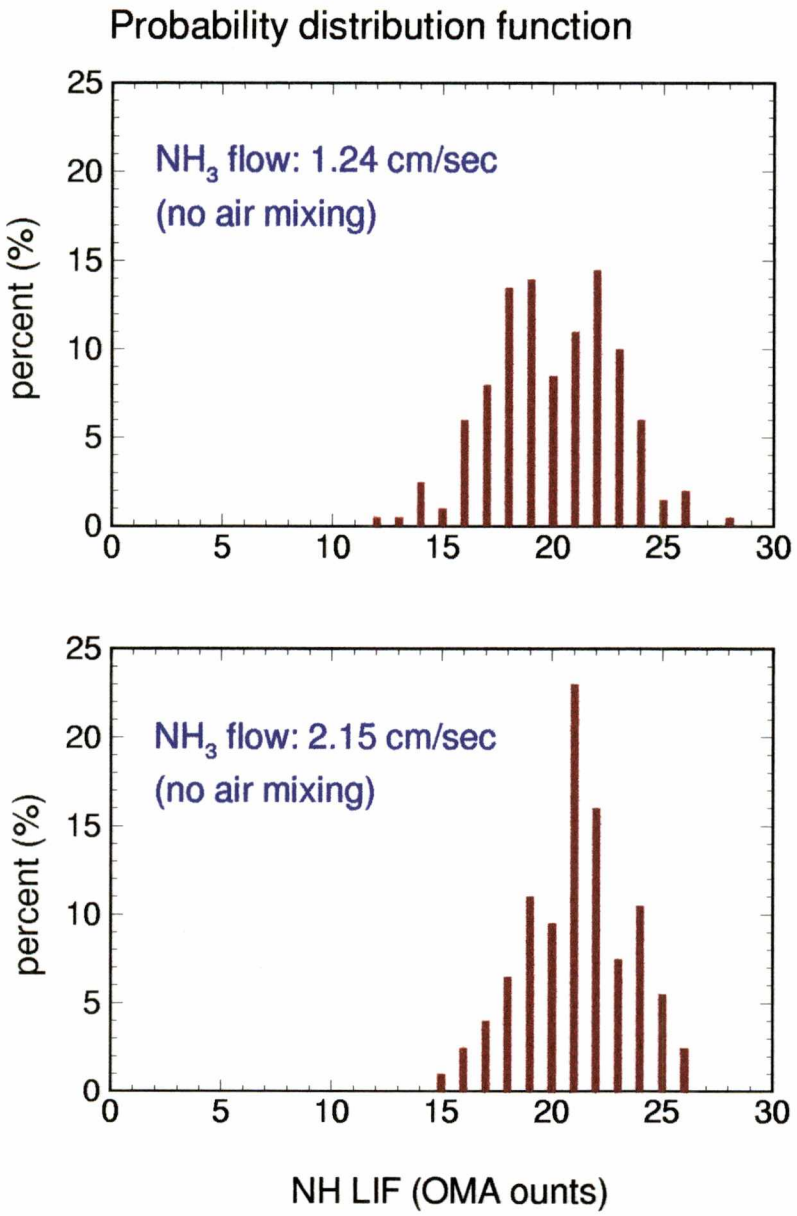



Figure 4.10: Probability distribution functions of NH concentration in ammonia breakdowns. A quartz-cylinder was used to eliminate air-mixing effect.

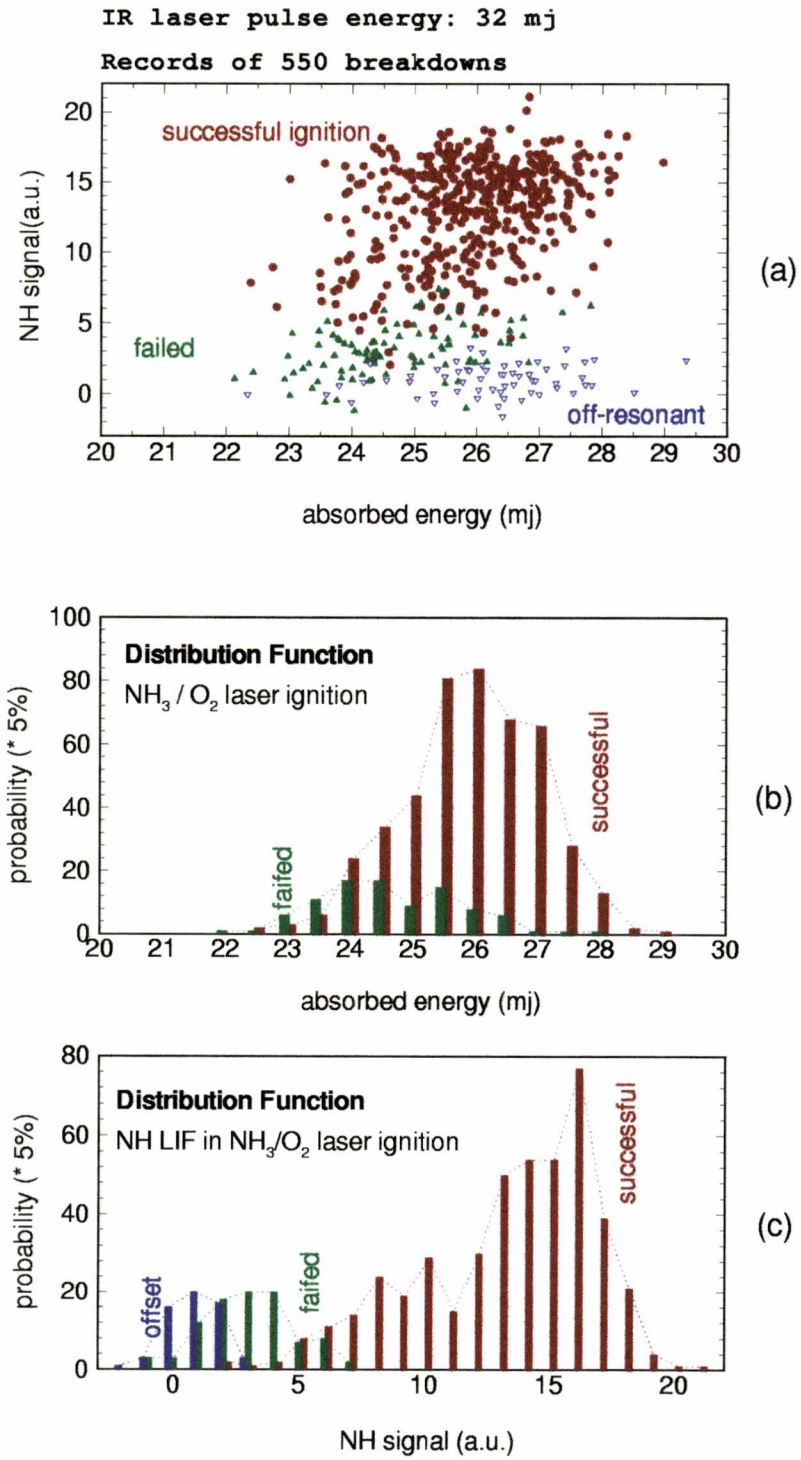



Figure 4.11: Results of laser-ignition experiment: (a). scatter plot of NH fluorescence and absorbed laser energies for failed and successful ignitions, (b). probability distribution functions of absorption, and (c). probability distribution functions of NH concentration.

$mJ$, absorption was approximately 26 $mJ$ with a fluctuation of less than 10 %. The initial plasma kernel could be described as a cylinder of nominal length × cross-sectional area of $1 \times 0.01\ mm^3$, and this volume had expanded to a cylinder of volume $3 \times 4\ mm^3$ at 5 $\mu sec$ after breakdown. It was found that the absorbed energies and kernel sizes and volume did not exhibit significant pulse-to-pulse variation and yet 94 out of 550 breakdown events failed to progress to ignition. Shown in Figure 4.11(a) are the NH signals for each of these breakdown events, and it is seen that the successful and failed ignition events can be group into two distinct groups with only a modest amount of overlap. Compared with the previous PDF measurements in pure ammonia flows, these two groups in Figure 4.11(a) correspond to the two-peak profiles for the ammonia breakdown process. When the data in Figure 4.11(a) are projected onto the X- and Y-axes, the probability distribution functions of absorption and recombined NH could be plotted (see Figure 4.11(b) and (c)). These results show that the fate of the laser ignition is very possibly already determined at the early time of energy deposition. At 5 $\mu sec$ after deposition ends, the density of the recombined intermediate species clearly predicts the destinies of ignition much earlier than the time when the chemical reactions become significant. Since the size of initial plasma in the focal zone is so small compare to that of electric sparks, the air-mixing effects is strongly responsible for the fluctuating of formation of laser-induced plasma. As we increase the flow speed further, the probability of failed ignition reduces to zero.

# Chapter 5

# Time-Resolved Shadowgraphs and Kernel-Dynamics of Laser-Induced Breakdown and Ignition

High-speed photography using the shadowgraph method was performed to visualize the sequences of events in the development of the plasma kernel following a single laser-induced breakdown or ignition event. The shadowgraph technique, which is a simplified variation of the Schlieren method [56, 57, 58, 59, 60], has been widely applied in the measurement of shock waves for decades. The propagation of radiation is known to be affected by density variations of the medium through which the beam passes. For a spatial density variation of the assumed lossless transmission medium, both diffractive and refractive effects are possible for coherent optical beams. A measure of the magnitude of diffraction of radiation of wavelength $\lambda$ is given by the ratio $\lambda/L$, where $L$ is a characteristic length of the scattering object or density gradient. In this study, the characteristic lengths are typically such that $\lambda/L << 1$ for optical radiation, and as a result, diffraction is not significant. The only exception could be the thickness of the shock-front following laser breakdown, and the subsequent

photographic data will indicate the magnitude of this effect.

For shadowgraph measurements, refractive effects are of more interest, for they provide information regarding the density variations in the medium and are useful in determining features such as shock- and flame-front shapes and speed and also general features of the reacting flowfield. Several models exist for evaluating the deviation of the propagation path of the ray and the change in the intensity of the transmitted beam. For example, for those cases for which the beam's amplitude varies slowly with respect to the wavelength $\lambda$, it is known that the Eikonal equation

$$(\bigtriangledown\ L)^2 = n^2(\vec{r})\ , \tag{5.1}$$

is the descriptive equation for the locus of constant phase of the wave and that the ray's direction is perpendicular to these constant phase surface [61]. In Equation 5.1, $n(\vec{r})$ is the spatially varying index of refraction and $L$ is the optical path-length. From Equation 5.1, it is easily shown that the locus of the ray can be written as

$$\frac{d}{dt}[n(\vec{r})\ \frac{d\vec{r}}{ds}] = (\bigtriangledown\ n)\ , \tag{5.2}$$

where $\hat{s}$ is the unit vector of the propagation path. Discontinuities or rapid spatial changes in $n(\vec{r})$ are dealt with using the general form of Fermat's Principle. From Fermat's Principle with a straightforward derivation, one can show that the radius of curvature $R$ of a light ray traveling through a medium with index of refraction $n$ is given by [62]:

$$\frac{1}{R} = \frac{1}{n}(\bigtriangledown\ n)\ , \tag{5.3}$$

or expressed for the angle of displacement

$$\phi = \frac{L}{R} = \frac{L}{n}(\bigtriangledown\ n)\ , \tag{5.4}$$

where $L$ is the thickness of the medium. If the wavelength of the incident light beam is far from any resonant excitation of the medium, a simple expression (known as the Dale-Gladstone Law) describes the relation between the fluid density $\rho$ and the refractive index.

$$n - 1 = K\rho \ , \tag{5.5}$$

where $K$ is a constant for any given gas over a wide range of pressure, and has very small dependence on wavelength. In the case involving ionization, the equation can be expressed as

$$n - 1 = \Sigma_s K_s \rho_s + K_e \rho_e \ , \tag{5.6}$$

where the summation is over different molecule species, and the contribution from the free electrons can be negative and dispersive. In the shadowgraph method, a beam of parallel light is used to transmit through the object of interest, and then illuminates a display screen at the back of this object. On the screen, the shadow illustrates the beam displacement due to the density gradient in its light path. The brightness (darkness) in the shadowgraph indicates a convergence (divergence) of light, and the convergence is proportional to the gradient of the angle displacement ($\bigtriangledown \phi$) for small angle and near-zone measurement. Thus, the shadow effect depends on the second derivative of the density, under this approximation. When the screen is moved farther from the detected object, the difference between the shadowgraphs and the true position (or size) of subject increases.

In the following sections, we demonstrate high-speed shadowgraphs of laser breakdowns using high-frequency laser pulses (13.5 $kHz$) as the light source of shadowgraph

method with a synchronized high-speed camera. The presentation includes the statistical, or shot-to-shot, variation of laser-induced breakdown and ignition, the variation in the observed behavior with increased laser power, the observation of shock waves and the overall process of kernel development.

## 5.1 Experiment of Shadowgraphs

Figure 5.1 shows a schematic of the experimental arrangement used to take the shadowgraphs of laser-induced plasmas. The Nd:YAG laser system and optics used to create the optical breakdowns have been described in the previous chapters. In addition to the burner system used to provide a constant axisymmetric flow of ammonia or/and oxygen gases, an annular sheath-gas flow of argon was used to surround the core flow. This sheath flow served to help stabilize the core flow field and to decrease its diffusive and gas-dynamic mixing with ambient air.

To record the time-resolved shadowgraph images of the decaying plasma, an Oxford copper-vapor laser (CVL) with wavelength of 510 $nm$ and pulse width (FWHM) about 30 $ns$ was used as the light source. The CVL pulse repetition rate was 13.5 $kHz$, and the propagation direction of the CVL pulses and the Nd:YAG beam were perpendicular; both of these beam axes were perpendicular to the cylindrical axis of the burner flowfield. The shadowgraphs of the breakdown kernels were imaged on a screen that was located approximately two meters behind the kernels. A Kodak high-speed camera, Model 4540, was synchronized with the CVL source to provide a photographic record of the breakdown and post-breakdown phenomena. The images of 128×128 pixels have spatial resolution of approximately 115 $\pm$ 5 $\mu m$ in both the

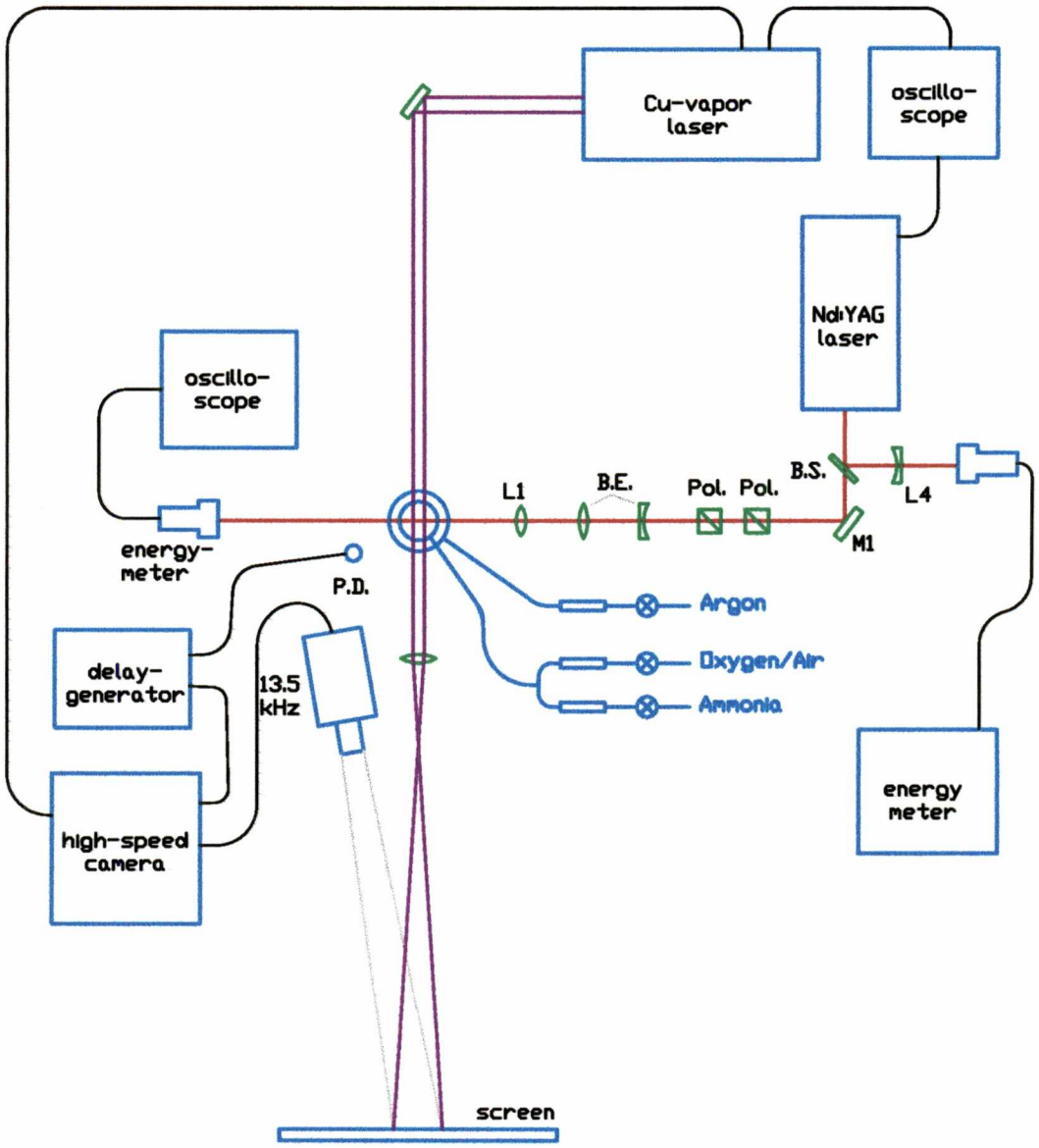



Figure 5.1: Experiment arrangement for shadowgraphs, L = lens, M = mirror, Pol. = polarizer, B.E. = beam expander, P.D. = photodiode

horizontal and vertical directions. The temporal resolution (or the exposure time) of the shadowgraphs was determined by the pulse-width of copper laser. Two DG-535 delay generators controlled the timing between the camera and two laser systems. When ignition data were acquired, a photodiode monitored the transmitted YAG-laser pulse and terminated the recording of the high-speed camera at 150 $ms$ after the arrival of Nd:YAG signal.

## 5.2 Shock Waves and Kernel Development in the Early Period

Figure 5.2 shows the development of the plasma kernel during the first 60 $\mu s$ after the breakdown. The images of the left-most column show the optical breakdowns of laboratory air with absorbed energy of 24.4 $\pm$ 0.5 $mJ$. The images of the middle and right-most columns show the breakdowns in the premixed ammonia/oxygen gases with equivalence ratios of 1.0 (stoichiometric condition) and 1.5 (fuel-rich condition), respectively. The absorbed energies in both of the ignition conditions were 28.0 $\pm$ 0.5 $mJ$. The Nd:YAG laser beam was focused from the left-hand side, and the burner was located at the lower side of all images. At 0.5 $\mu s$ of delay time, breakdown kernels appear identical under these three experimental conditions. After 5 $\mu sec$, the shock waves have already separated from the plasma kernels and have propagated outward. The reflections of shock from the flat-flame burner can be observed after 40 $\mu s$ of time. For the observed time regimes, and under these three experimental conditions, the shock waves were observed to be supersonic, but not hypersonic. The interference patterns of the CVL beam in all images reveal the kernel sizes rather than the

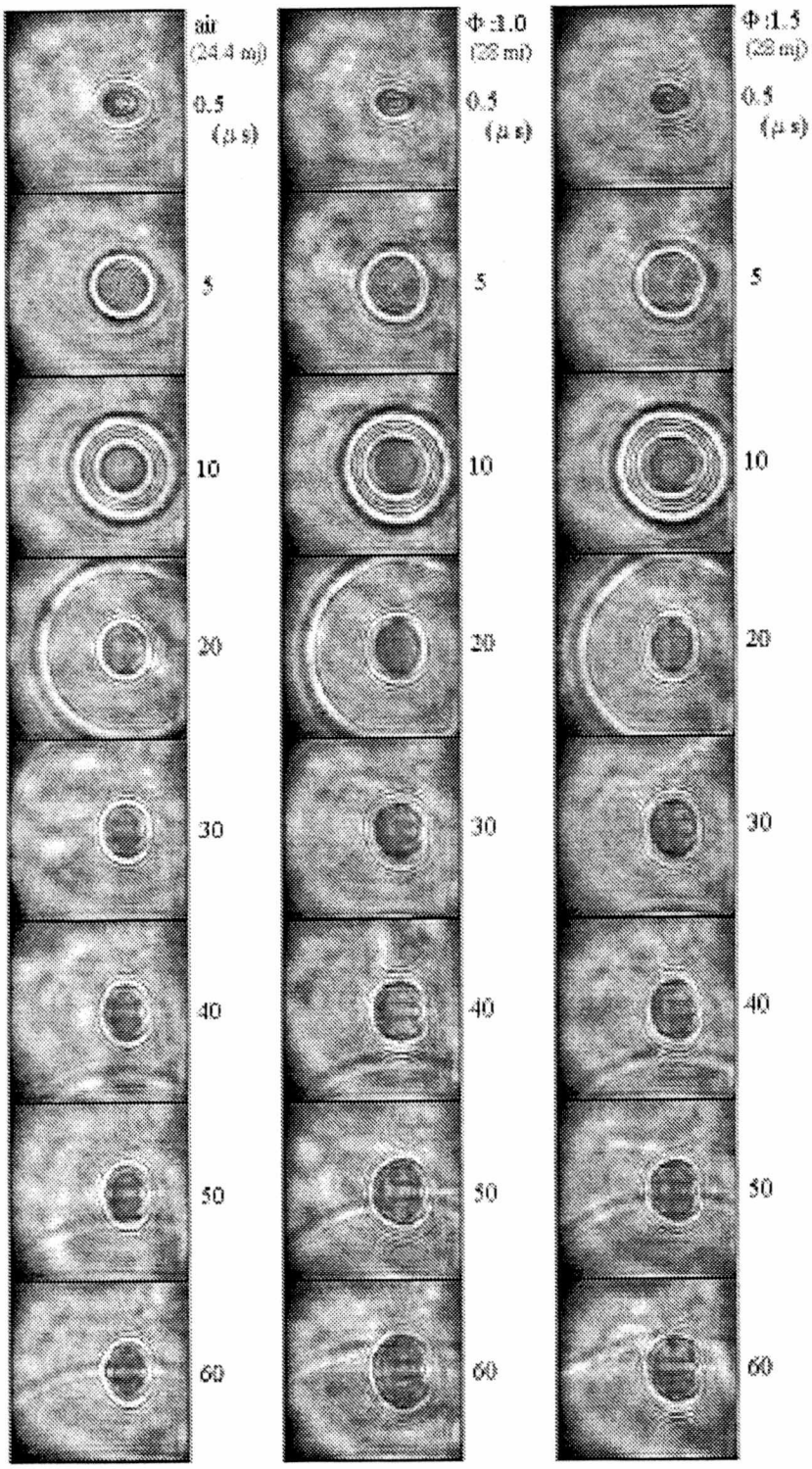



Figure 5.2: Shadowgraphs of laser-induced breakdowns in air (left) and premixed ammonia/oxygen flow (middle: mole-ratio=4/3, right: mole-ratio=2/1)

detailed structures of the kernels. The plasma kernels develop a tunnel, appearing from the right-hand side, moving opposite to the laser's direction after about 30 $\mu s$. The PLIF images in last chapter show this backstreaming behavior at much earlier time as compared to shadowgraphs here. This is because the PLIF images present the distribution of NH molecules in the thin layer of cross section of the decaying kernel, whereas the shadowgraphs are the images of interference patterns in the copper laser illumination beam with the whole kernel.

## 5.3 Development of a Single Laser-Induced Breakdown Event

Figure 5.3 shows a 3.5 $ms$-long recording of one complete sequence of the decay of a single laser-induced air breakdown event. For these data, 26.2 $\pm$ 0.5 $mJ$ of laser energy was deposited in the plasma. The very first image in this figure was recorded at 0.5 $\mu s$ after breakdown, and the subsequent recordings were taken at 74 $\mu s$ increments. The exact delay time of each image in Figure 5.3 is marked alongside its frame. It can be seen from Figures 5.2 and 5.3 that the plasma kernel decays away without significantly changing its size, which suggests that, after the first few microseconds following the breakdown, the pressure inside the kernel has already decreased to a value close to the post-shock gas pressure outside the kernel. The backstreaming structure (the tail or tunnel) moves and decays with a gradually reducing speed of approximately 25 to 1 $m/sec$. Gas- and kernel-dynamics are likely the primary considerations in the early decaying process ($\ll$ 500 $\mu sec$) of laser-induced breakdowns. After the gas-dynamics effects fade-out, diffusion contributes mostly in the rest of

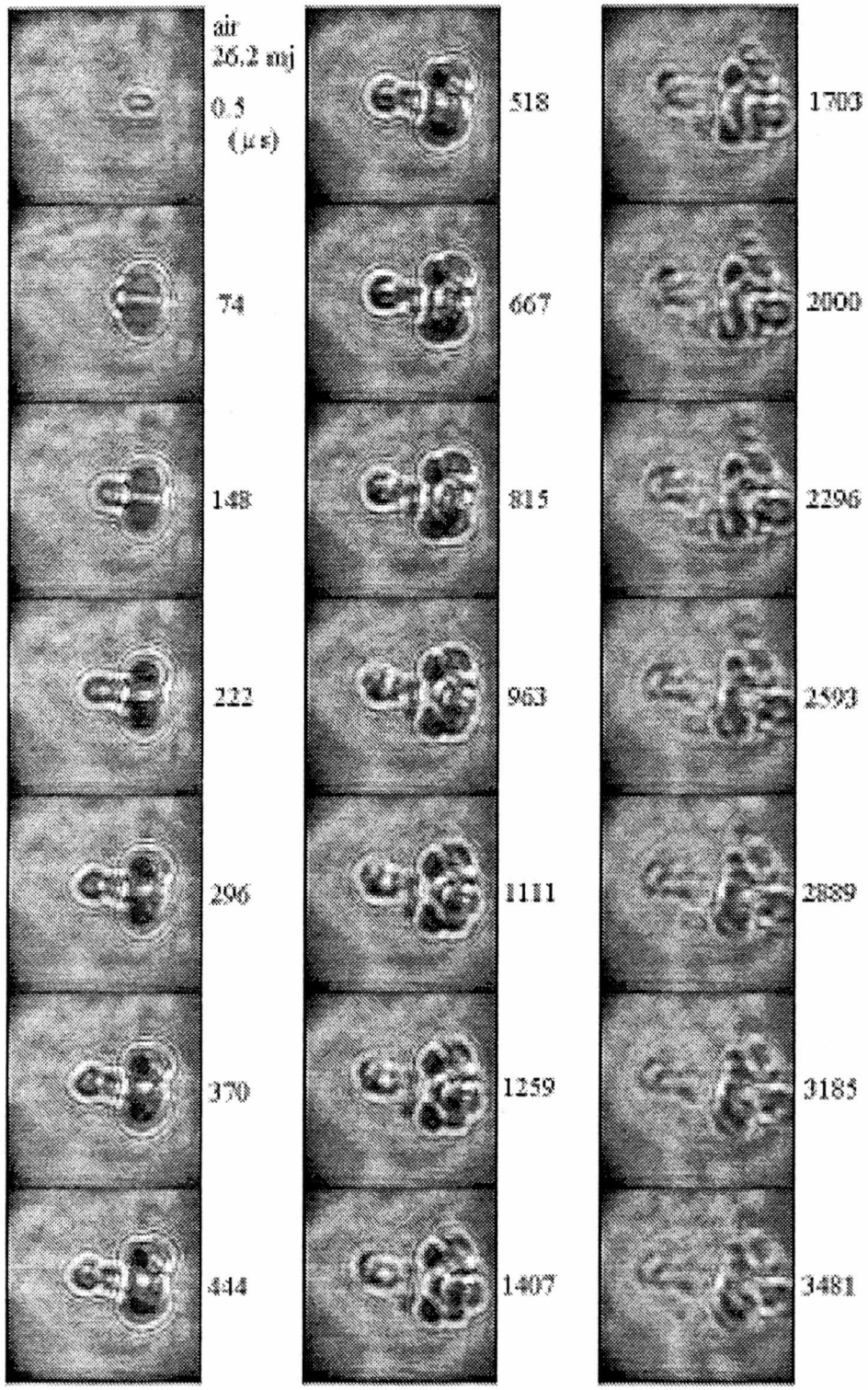



Figure 5.3: Shadowgraphs of one individual laser-induced breakdown in still air. absorbed laser energy: 26.2 $mJ$

decaying process. A sequence of shadowgraphs of the laser ignition process from initiation through decay in fuel-rich ammonia/oxygen flow, is shown in Figure 5.4. The absorbed energy of this event was $28.0 \pm 0.5\ mJ$. The physical structure (from the backstreaming effect) of the decaying kernel was observed as well. With the participation of a stronger chemical reaction, the plasma kernel developed into a flame kernel within $0.1\ ms$. The contour of the flame kernel is much smoother than the breakdown kernel in Figure 5.3. After $1.5\ ms$, the flame front expanded out of the range of the shadowgraphs light source.

The toroidal shape of the kernel appears to be a universal phenomenon of both short-pulse electric and laser sparks [23, 63, 64]. Although the development of the electric kernel is symmetric along its axis, results of the computer simulation of electric sparks by Kono *et al.* [64] provide some important information of the backstreaming effect of laser sparks. Their calculation of sparks in nitrogen, which neglected chemical reaction effects, shows the formation process of a hot ellipsoidal plasma kernel produced by the instantaneous electric spark ($< 0.3\ \mu s$) in the cylindrical coordinate. Within the first few $\mu s$ after the birth of electric spark, a shock wave separates from the residual hot gas and propagates outward. Inside the shock wave, the gas moves outwards rapidly, and causes an over-expansion, resulting in a spatially varying velocity distribution after the shock wave is far from the kernel. This gaseous motion points inward along the axis, and outward in the radius direction, and causes the subsequent toroidal development of the kernel. The table below lists and compares some of Kono *et al.*'s simulation or experimental parameters and their results with our observations from shadowgraphs of laser breakdowns.

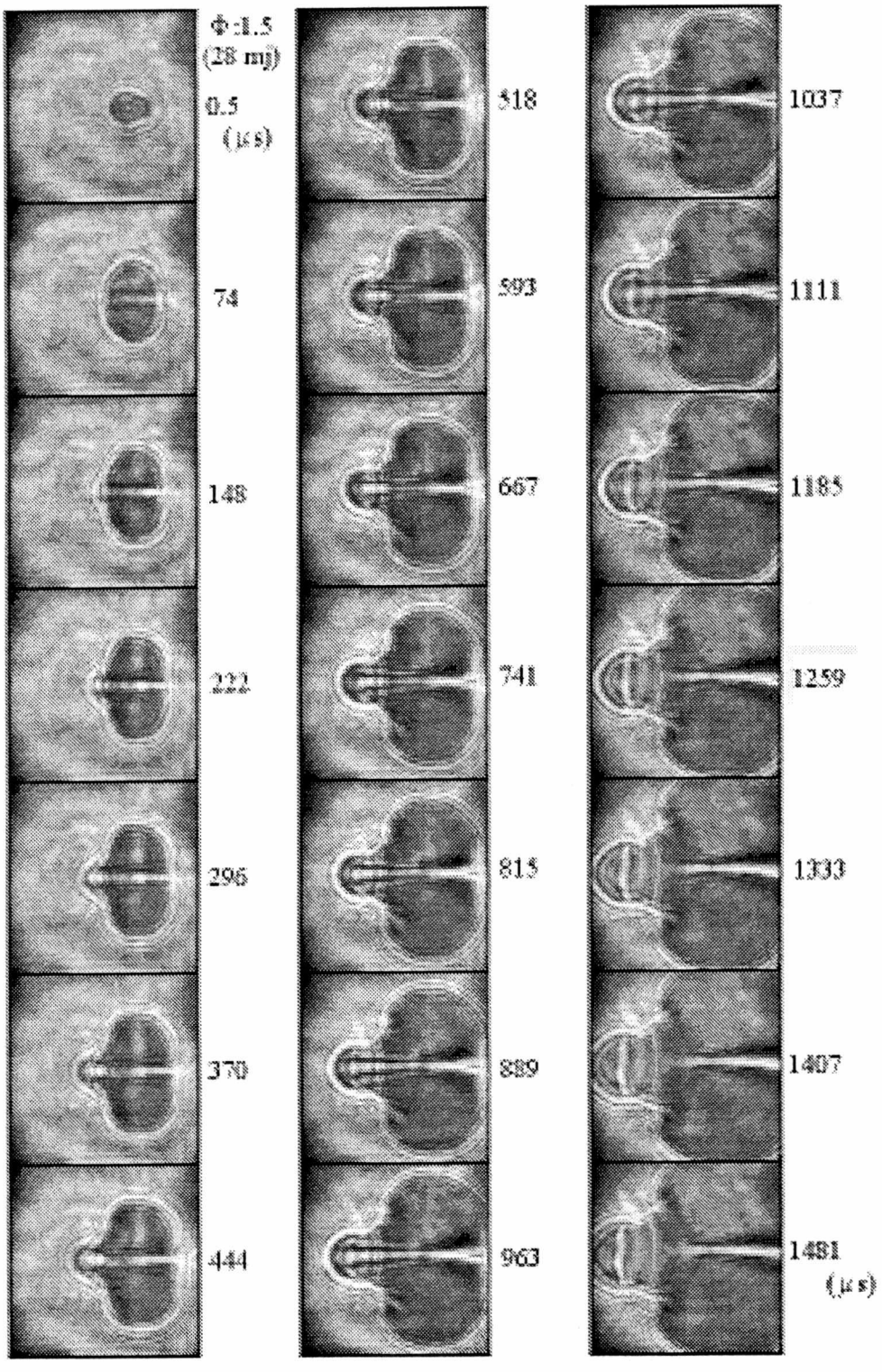



Figure 5.4: Shadowgraphs of one individual laser-induced breakdown in premixed ammonia/oxygen mixture. absorbed laser energy: 26.2 $mJ$

| | Kono *et al.* | | | this work |
|---|---|---|---|---|
| deposited energy | 2.1 $mJ$ | 4.6 $mJ$ | 9.1 $mJ$ | $\sim$ 25 $mJ$ |
| deposition time | $< 0.3\mu s$ | $< 0.3\mu s$ | $< 0.3\mu s$ | $< 0.02\mu s$ |
| shape of initial plasma | ellipsoid (at 0.3 $\mu s$) | ellipsoid (at 0.3 $\mu s$) | ellipsoid (at 0.3 $\mu s$) | cone (at 20 $ns$) egg (at 0.5 $\mu s$) |
| size of kernel (dia./length) | 0.2/2.8, 0.2/1.6, 0.8/1.6$mm$ (at 0.3 $\mu s$) | 0.2 $mm$/ .5 $\sim$ 1.5$mm$ (at 0.3 $\mu s$) | 0.2 $mm$/ - (at 0.3 $\mu s$) | 0.2 $mm$/ $\sim$ 1 $mm$ (at 20 $ns$) |
| formation-time of torus | $< 50\mu s$ | $< 18\mu s$ | $< 18\mu s$ | 10 $\sim$ 30 $\mu s$ |
| diameter of torus | $\sim$ 1, 2, 3 $mm$ (at 100 $\mu s$) | $\sim$ 2 $mm$ (at 20 $\mu s$) | $\sim$ 2 $mm$ (at 20 $\mu s$) | $\sim$ 3 $mm$ (at 30 $\mu s$) |
| gaseous motion | -, 9, 7.5 $m/s$ (at 100 $\mu s$) | - | - | $>$ 25 $m/s$ (35$\mu s$) $\sim$ 15$m/s$ (100$\mu s$) |

Contrasted to the electric spark, the laser-induced plasma has an asymmetrical (backstreaming) decaying feature, which is very likely due to its asymmetrical optical focusing geometry; i.e., the initial plasma is formed on only one side of the focal zone. In our experiment, the initial plasma is shaped like a horn lying on the optical axis with a length of approximately 1.0 $mm$ and diameter of 200 $\mu m$ on the left (lens side) and 35 $\mu m$ on the right end. According to Kono *et al.*'s comparison in the 2.1 $mJ$-deposition cases, the shape (or the ratio of length and diameter) of the initial plasma affects the strength and distribution of gaseous motion that results in the toroidal development. The energy density deposited in the initial plasma will also affect the intensity of shock wave and the subsequent gaseous vortices. Since the geometric shape of the initial plasma of laser breakdown is asymmetric and the deposited energy density is greatly different on both sides, the strength of inward gaseous motions along

the plasma axis are expected to be mismatched and the backstreaming phenomena would be a consequent result. As we observed from the shadowgraphs, the speed of the backstreaming motion is around 25 $m/sec$ at 35 $\mu s$ of time and decreases with the decaying process. This movement is about 3 to 4 times stronger than Kono *et al.*'s calculation for 2.1 $mJ$ condition, but the absorbed energy in the laser plasma is about 10 times larger than Kono *et al.*'s condition as well. More detailed computations are required, however, to describe quantitatively and accurately this vortex production process.

Another possible cause of backstreaming phenomena in laser breakdown is the laser preheating of ambient gas in front of the breakdown region. Peterkin *et al.* described the formation of an aneurismal structure in front of the laser-induced plasma in metal surface using a computer code, MACH2 [65]. This computer simulation and experimental measurement demonstrate the effect of laser preheating in the generation of aneurysms. As Peterkin *et al.* discussed, the formation of the asymmetric aneurysms in the laser/kernel interface requires that the laser irradiance is sufficiently large to ionize the ambient gas to some certain density. In this case, $10^3 \sim 10^5\ GW/cm^2$ of laser irradiance and a few percent of pre-ionized gas molecules are required. If the ambient medium is not preionized, there is no aneurysm. The time of formation and development of aneurysm in Peterkin *et al.*'s observation and calculation results are extremely short and on the order of tens to hundreds $nsec$. The effect caused by the laser preheating is much faster than the backstreaming phenomena we observed. Moreover, the backstreaming effect in laser-induced gas breakdown seems to start from the back (focal side), where the laser pulse is mostly

absorbed, rather than the heating side. This phenomena is shown very clearly in the time-resolved NH PLIF images in this dissertation.

## 5.4 Laser-Induced Breakdown in Still Air

Shadowgraphs of laser-induced air breakdowns are compared in Figures 5.5 and 5.6. In static laboratory air, the formations of laser-induced plasmas are very stable, and the cause of the deviations between breakdowns is mostly the variation in output and beam quality of the Nd:YAG laser pulses. Three subsequent air breakdowns were recorded in each figure. The absorbed laser energies were $26.2 \pm 0.5\ mJ$ in Figure 5.5 and $54 \pm 0.5\ mJ$ in Figure 5.6. Other than the expansion in the kernel sizes, increasing the deposited energy neither intensifies the shock waves nor significantly extends in time the kernel decay process. Under exactly the same experimental conditions, the observable differences between each of three independent breakdown events are their kernel shapes (body and tail), which are strongly affected by the backstreaming effect. The spatial and temporal structures of the Nd:YAG laser pulses would be responsible for these small deviations of kernel-dynamics in each individual breakdown.

## 5.5 Laser-Induced Spark Ignition

Laser-induced breakdowns in three different premixed ammonia/oxygen flows are presented in Figure 5.7. From left-to-right, breakdowns were induced in pure oxygen flow (equivalence ratio, $\Phi = 0$), stoichimetric ($\Phi = 1.0$), and fuel-rich ($\Phi = 1.5$) conditions. The flow speeds of the premixed gases in these three conditions were all controlled at $6.0\ cm/sec$. The deposited laser energy in these three kernels were 24.6, 28.0 and

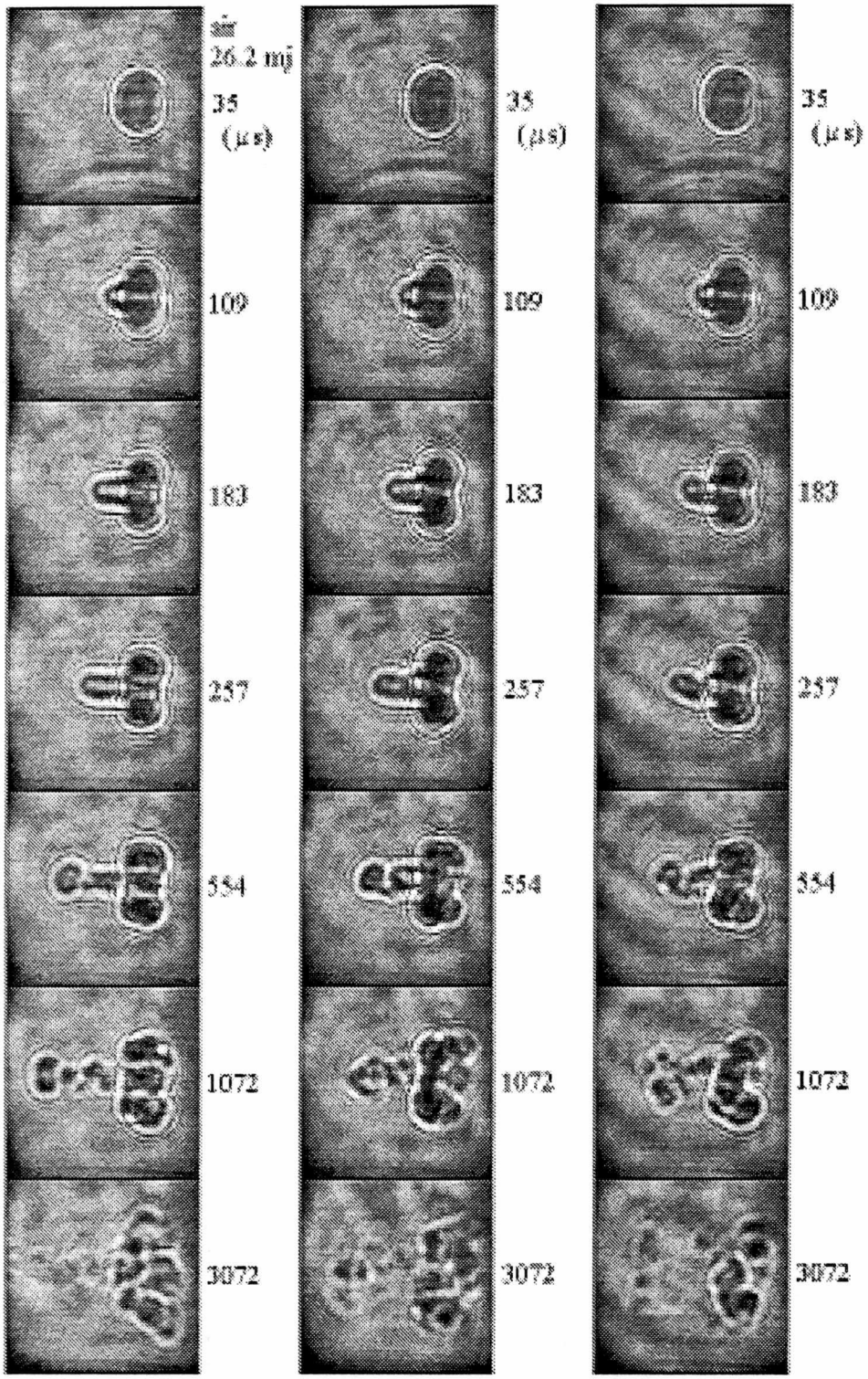



Figure 5.5: Shadowgraphs of three individual laser-induced breakdowns in still air. absorbed laser energy: 26.2 $mJ$

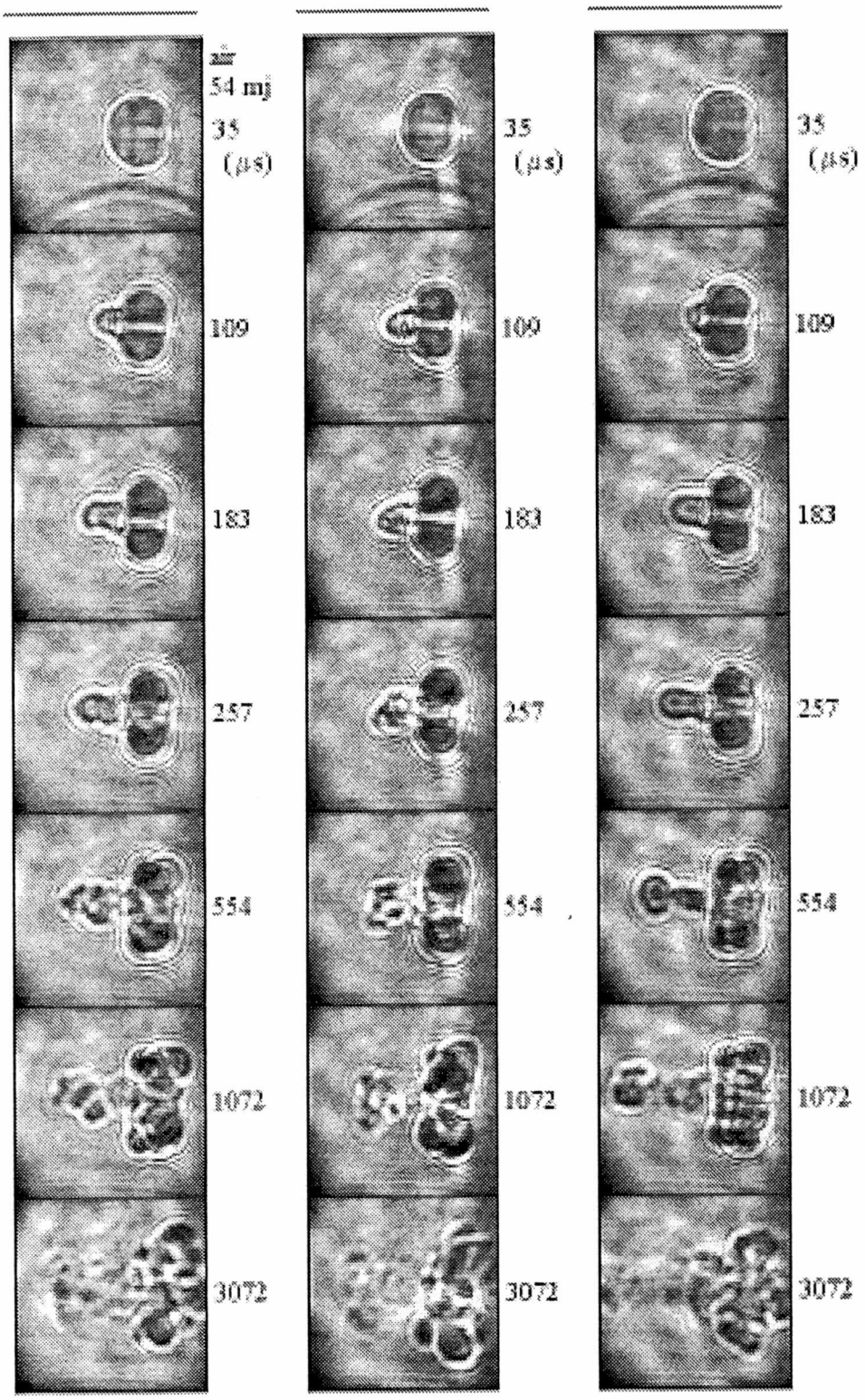



Figure 5.6: Shadowgraphs of three individual laser-induced breakdowns in still air. absorbed laser energy: 54 $mJ$

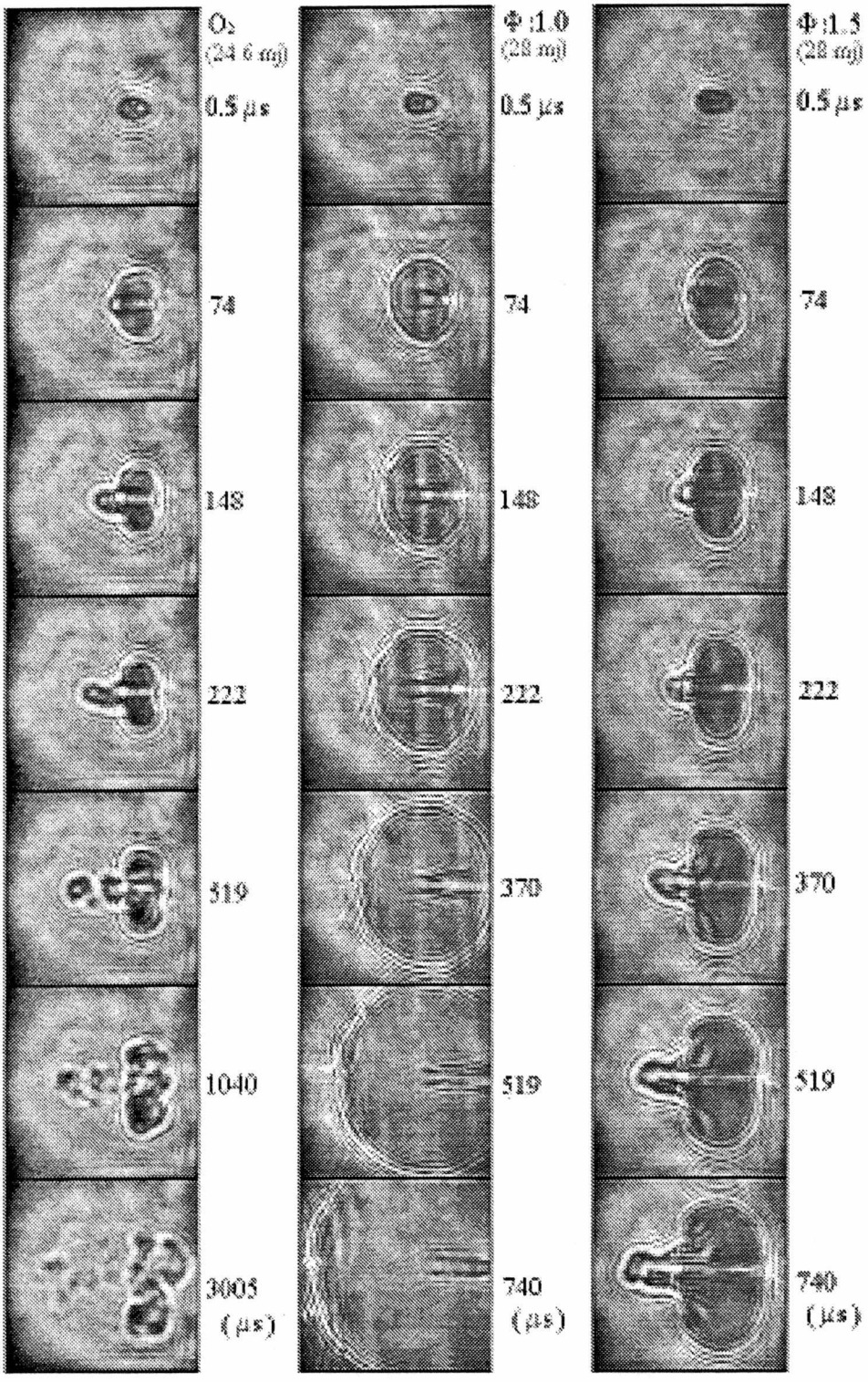



Figure 5.7: Shadowgraphs of laser-induced breakdowns in premixed ammonia/oxygen flow. mole-ratio = 0/1 (left), 4/3 (middle), 2/1 (right). flow speed = 6 $cm/sec$

28.0 $mJ \pm 5\%$, respectively. As indicated in the figure, the corresponding times for each shadowgraph are not exactly the same in these three columns. At the delay time of 74 $\mu s$, the developing kernels show apparent differences in their sizes due to the degree of involvement of chemical reactions. For the stoichimetric condition, the chemistry within the kernel is so strong that it overcomes the backstreaming effect of kernel and the breakdown kernel evolves into ignition similar to a point flame source. In contrast to the $\Phi = 0$ for pure oxygen and $\Phi = 1.5$ for fuel rich conditions, the flame front of ignition in stoichiometric mixture appears spherical. In the fuel-rich condition, the chemical reactions are not as fierce as at stoichiometry. The development of the kernel shows the compensation between the boundary chemistry and kernel dynamics.

To compare with the measurements of laser ignition, flame speeds in premixed ammonia/oxygen gases were calculated using the CHEMKIN [41] chemical kinetics code and the reaction mechanism found in reference [42]. In this calculation, species of $H_2$, $O_2$, H, O, OH, $HO_2$, $H_2O_2$, $H_2O$, $N_2$, N, NO, $NO_2$, HNO, $NH_3$, $NH_2$, NH, $N_2H_4$ and $N_2H_3$ are considered, and the rate constants are quoted from reference [66]. The laminar flame speeds of the $\Phi = 1.0$ and $\Phi = 1.5$ cases are obtained as 118 and 77 $cm/sec$, respectively. In Figure 5.7, the average expansion speeds for the two ignition cases during 0.1 to 0.5 $ms$ are approximately 11 and 4.4 $m/s$ in the radius direction. If we use the relation of laminar flame speed and the spherically expanding flame front speed discussed in reference [18], and assume that the thickness of flame front in our experiment is negligible compared to its distance from the ignition source, then the flame speed in $\Phi = 1.0$ and $\Phi = 1.5$ conditions are derived to be 115 $cm/sec$ and

52 $cm/sec$ respectively. In this derivation, the assumptions made are not rigorous especially for the fuel-rich case due to the stronger gas-dynamic effect compared to its chemical reactions. The reason for the large percentage difference in the fuel-rich side is not well understood in this point.

# Chapter 6

# Detection of NH in Optical Breakdown Using Laser-Induced Fluorescence (LIF) — Theoretical Preparation

Laser-induced fluorescence (LIF) is one of the most sensitive spectroscopic methods used in today's laboratories. It possesses the capability of detecting transient free radicals at the part-per-million (ppm) and even part-per-billion (ppb) level. The objective of this chapter is to discuss the practical considerations of measuring NH molecules in the ammonia/oxygen breakdown kernel using this spectroscopic technique. As discussed in Chapter 2, the NH radical exists only inside the thin layer of the flame-front with the thickness of 0.2 to 0.4 $mm$. Moreover, NH molecules produced from the chemical reaction appear only for a very short time, between 80 to 400 $\mu s$, after the reaction starts. Monitoring the spatial and temporal formation of a transient species such as NH provides significant information of the gas-dynamics as well as the chemistry in the ignition process. From the spectroscopic point of view, the triplet emission of NH molecules in the $(A^3\Pi_i - X^3\Sigma^-)$ system has been studied

since 1919 [67, 68, 69, 70]. The (0-0)-band of the NH spectrum exhibits an open rotational structure in the P- and R-branches with well-resolved spin splittings. With these advantages, the rotational temperatures of NH molecules are comparatively easily obtained and analyzed in the environment of heavy collisional quenching.

The discussion in the subsequent sections describes the experimental conditions (e.g. laser irradiance, laser pulse-width, detection condition, etc.) and presents appropriate models to obtain the NH temperature and concentration in the ignition kernel. The primary difficulty in these measurements is the lack of understanding in the thermal-averaged energy-transfer cross sections and the quenching conditions of the high-pressure, hot plasma kernel. For the analysis, the necessary assumptions, approximations, and estimations (based on the knowledge of atmospheric-pressure combustion calculations and measurements) are discussed.

## 6.1 Introduction to LIF

Fluorescence is the spontaneous emission of radiation from an atom or molecule following its excitation by various ways: heating, chemical reaction, collision with electron, or photon absorption. For laser-induced fluorescence, a laser beam is used to cause photon absorption in a particular species by tuning the laser wavelength to the resonance of one of the molecule or atom. The population in the directly pumped upper state increases efficiently from the supply of the corresponding lower state. Since the absorption process is resonant, laser-induced fluorescence has larger cross sections than most of the other spectroscopic methods.

Laser-induced fluorescence is emitted by the spontaneous radiation from the ex-

cited state of the atom or molecule following photon absorption. While a molecule is in an excited electronic state, it does not necessarily emit radiation to return to the stable ground state. Many other pathways of energy loss are available to compete with spontaneous emission. They include dissociation, energy transfer to another molecular, energy transfer to other internal energy states in the same molecule, and chemical reaction. These paths competitive with fluorescence, termed quenching processes, reduce the amount of fluorescence and obscure the interpretation of the LIF data. The understanding of quenching processes may be achieved through calculation, if all the colliding species densities are known, and if all the appropriate quenching and energy-transfer rates data are available. But this is hardly the situation. One of the ways of dealing with this difficulty is to use experimentally determined quenching correction. It is necessary to describe the quenching effects in more detail and evaluate the required parameters for NH detection in the following sections. Then, we are able to select the appropriate model and experimental conditions to minimize the errors due to the ignorance of collisional parameters and to attain the accurate measurements.

## 6.2 Calculation of NH ($A^3\Pi_i$-$X^3\Sigma^-$) Spectrum

To employ the NH LIF measurement, the computation of the synthetic NH spectrum is necessary. Using available tables of electronic dipole line strengths [71, 72], the molecular spectrum of spontaneous radiation, laser-induced fluorescence, Raman scattering and degenerate four-wave mixing can all be computed for specified rotational and vibrational temperatures. The line strength is a very convenient quantity

for the calculation of synthetic spectra, and it can be transformed to the Einstein coefficients, oscillator strength, and cross sections [73].

A set of synthetic spectra of the NH (A-X) system with the spectral resolution of 15 $cm^{-1}$ is shown in Figure 6.1 for an equibrium temperature of 3000 $K$. The transitions located between 325-350 $nm$ are the $\Delta v = 0$ sequence bands, and include (0-0), (1-1), and (2-2) bands. The vibrational transition bands ($v' = 1$, $v'' = 0$) and ($v' = 0$, $v'' = 1$) with intensity amplification of 250 are also shown. The symbols $v$ and J are the vibrational and rotational quantum number, and the prime ($'$) and double prime ($''$) are used to indicate, respectively, the upper and lower electronic states. Due to the similarity of the potential curves of the upper and lower electronic states, the NH (A-X) spectrum exhibits the symmetric structure centered on the band-head at 336 $nm$. In laser-induced fluorescence experiments, the probe laser is tuned in the wavelength range, 339-343 $nm$, which is part of the P-branch in the (0-0) band of the spectrum. In this spectral range, we can easily find some of the rotational transitions which are spectrally well-resolved with no overlap. Figure 6.2 shows the experimental data of the NH excitation spectrum in the atmospheric pressure ammonia/oxygen flame. The excitation spectrum provides highly resolved spectral structure by scanning the wavelength of a probe laser. The spectral line-width of the probe laser is $\sim 0.15\ cm^{-1}$, and the measured FWHM of spectral resolution in Figure 6.2 is $\sim 0.5\ cm^{-1}$, indicating the absorption line-width to be $\sim 0.4\ cm^{-1}$ in the ammonia/oxygen flame. This value is close to the measured value of OH ($\sim 0.3\ cm^{-1}$) in the atmospheric combustion [74, 75]. In the next chapter, the experimental LIF and calculated spectra will be used to determine two-dimensional spatial temperature profiles. It will be seen that

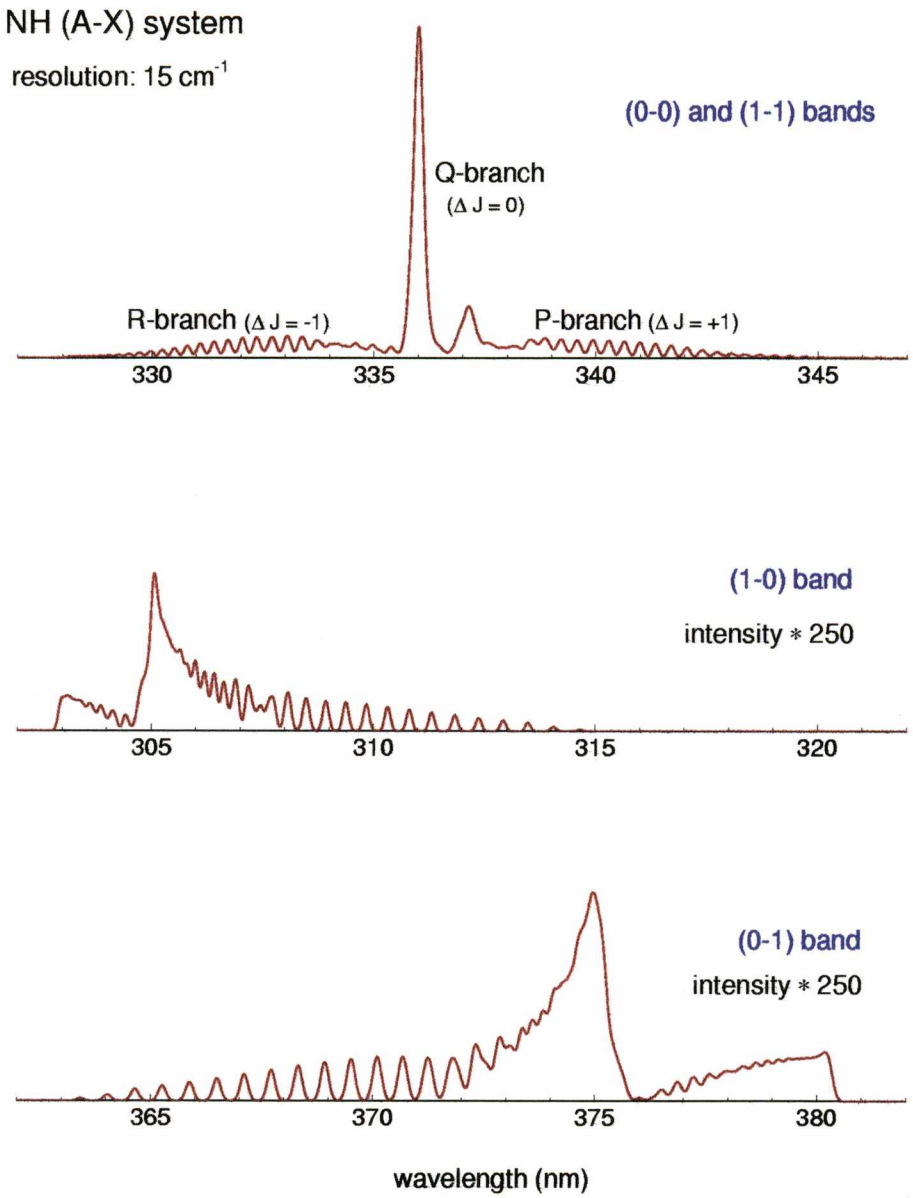



Figure 6.1: Synthetic spectra of NH ($A^3\Pi_i$-$X^3\Sigma^-$) spontaneous radiation.

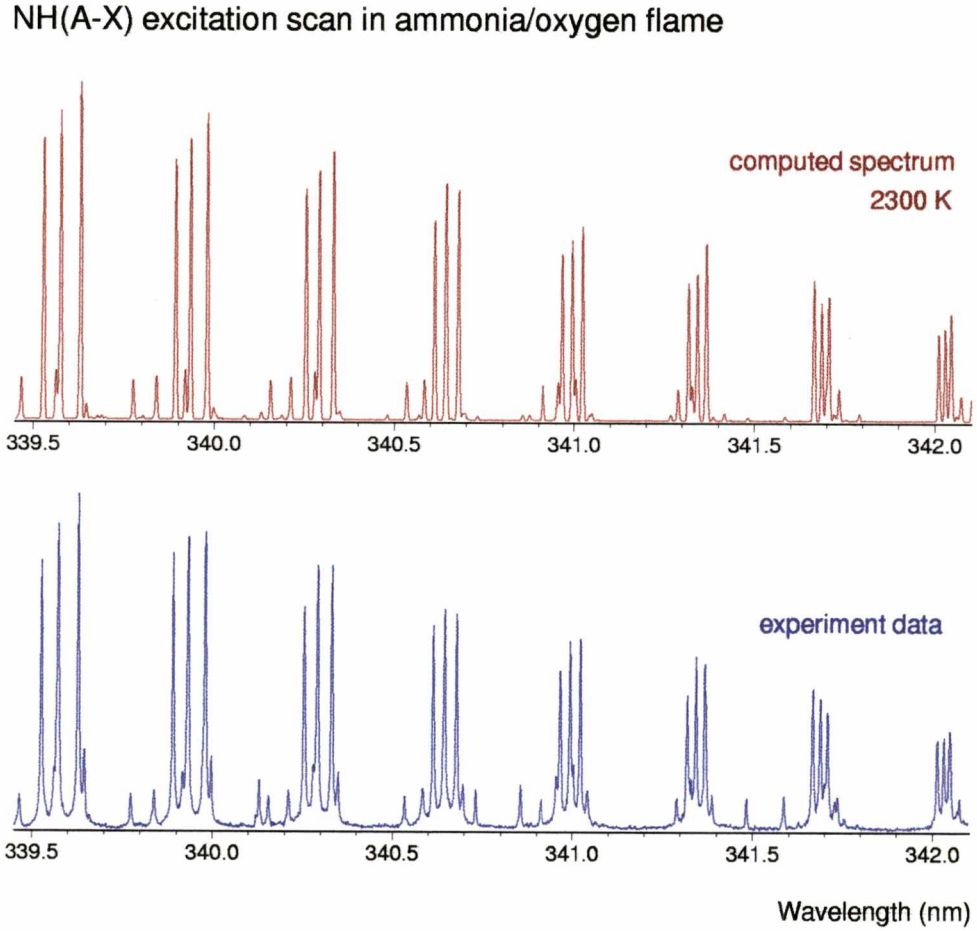



Figure 6.2: NH excitation spectra in atmospheric-pressure ammonia/oxygen flame.

comparatively clean rotational transitions were found to be useful for this purpose and to be free of both multi-species excitations and multiple excitations of the same species.

## 6.3 Time-Dependent Study Using Two-Level Model

In this section we consider NH LIF in a simple two-energy-level model as shown in Figure 6.3. The two levels in this model correspond to the laser-directly pumped rotational levels in the ground and excited electronic states. The two-level model is not strictly appropriate for describing the LIF measurement at high pressure, because the collision energy transfers and quenching effects require the inclusion of more energy levels. However, the two-level model is useful in that it greatly simplifies the mathematics and enables the illustration of many basic concepts. In addition, the simple time-dependent analysis of the two-level model allows us to explore the importance of the pulse-width and temporal profile of the laser-pumping source. Following this presentation, an extension of the two-level model to a multi-level description will be provided.

In Figure 6.3, $N$ is the state population density and $g$ is the degeneracy. The subscripts 1 and 2 indicate the lower and upper levels respectively. $A$ is the spontaneous emission rate given by the Einstein A coefficient, and $Q$ represents the collision-quenching rate. $b_{12}$ and $b_{21}$ are the rates of absorption and stimulated emission, respectively. The b-parameters are proportional to the incident laser intensity and related to the Einstein coefficient of absorption and stimulated emission $B_{12}$ and $B_{21}$ through the equation

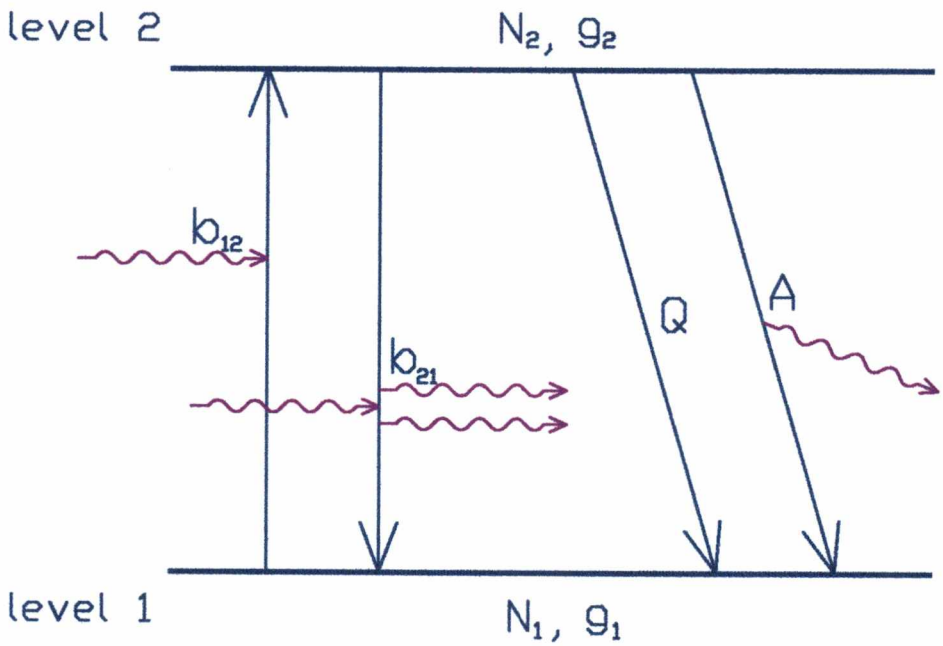



Figure 6.3: Diagram of two energy levels for LIF modeling. $N$ = state population density, $g$ = degeneracy, $A$ = rate of the spontaneous emission, $Q$ = rate of collision-quenching, $b_{12}$ = rate of absorption, $b_{21}$ = rate of stimulated emission

$$b_{nm}(t) = \frac{B_{nm}}{c} \int_{-\infty}^{\infty} I_L(\nu, t)\alpha(\nu)d\nu \ , \tag{6.1}$$

where $I_L$ is the spectral irradiance (with unit of $W/cm^2/cm^{-1}$) of the incident laser, $c$ is the speed of light, and $\alpha(\nu)$ is the absorption line profile function of the molecule. For the NH molecule, the natural line-width of the $(A^3\Pi_i - X^3\Sigma^-)$ transitions, which depend on the rotational quantum number J, is approximately $8\times10^{-5}\ cm^{-1}$ [71, 76, 77, 78]. Under the strong quenching conditions in atmospheric flame, the lifetime of OH and NH molecules are in the order of $1 \sim 2\ nsec$ [79, 80, 81, 82, 83, 84], which corresponds to a line-width of $\simeq 10^{-2}\ cm^{-1}$. However, in most situations, the Doppler- and pressure- broadening dominate the absorption profile, $\alpha(\nu)$. In a typical flame of temperature of 2000 K, the Doppler-broadening for the NH $(A-X)$ transition is calculated $0.24\ cm^{-1}$. In addition to the collision broadening, which is normally in the order of $0.1\ cm^{-1}$ at atmospheric pressure, we would expect a line width of absorption (or spontaneous radiation) in the range of a few tenths of wavenumbers. A typical absorption width of $\simeq 0.3\ cm^{-1}$ has been used for LIF measurement of diatomic molecules OH [83, 85], NH [86], and CN [87] in flame. When the probe laser pulse-width is smaller than the absorption line-width, the pumping is referred as the narrow-band excitation; otherwise, is called the broadband excitation.

Laser excitation of a two-level system can be described using the optical Bloch equations. However, it is known that the coherent properties of the resulting level populations are damped-out in times that are on the order of the phase-destruction relaxation time [88, 89]. In this case, the phase-destruction relaxation time is on the order of 100 picosecond, which is much smaller than the time resolution of this

study. Therefore, in the two-level system, the temporal variation of the excited-state population density for atmospheric-pressure breakdown excitation can be described by a rate equation of the form

$$\frac{dN_2(t)}{dt} = N_1(t)b_{12}(t) - N_2(t)[b_{21}(t) + Q + A] \ . \tag{6.2}$$

The population conservation equation can be written as

$$N_T = N_1(t) + N_2(t) = N_1(t = 0) \ , \tag{6.3}$$

where we assume that, initially, all the molecules reside in the lower level. Since the Einstein $B$ coefficient satisfy the relation $g_1 B_{12} = g_2 B_{21}$, we have

$$b_{12} = g b_{21} \ , \tag{6.4}$$

where $g = g_2/g_1$. If we eliminate $N_1(t)$ and $b_{21}$ from Eq. 6.2 by means of Eqs. 6.3 and 6.4, we obtain

$$\frac{dN_2(t)}{dt} = N_T b_{12}(t) - \frac{N_2(t)}{\tau} \ , \tag{6.5}$$

where

$$\frac{1}{\tau} = (1 + g)b_{21}(t) + A + Q = b_{12}(t) + b_{21}(t) + A + Q \ . \tag{6.6}$$

The unit of $\tau$ is $(sec)$. and $\tau$ can be interpreted as the effective lifetime of the excited state in the presence of the radiation field.

To solve the time-dependent LIF problem, the temporal, spatial, and spectral structure of the incident laser pulse must be given. Then, the time-dependent excitation rate $b_{12}$ in Eq. 6.5 can be obtained through Eq. 6.1.

To make the mathematics simple, we assume the spatial profile of the laser pulse is uniform and that its temporal profile is a rectangular function with pulse width of $\tau_L$

and magnitude $I_L$. For the narrow-band excitation, we can assume the laser spectral profile to be a delta function located at the central frequency of the absorption profile, $\nu_{21}$. With these simplifications, Eq. 6.5 can be solved easily, and the upper-state population density is found

$$N_2(t) = GN_T(\frac{S}{1+S})\left[1 - e^{-t/\tau}\right] , \qquad \text{for } 0 < t \leq \tau_L \tag{6.7}$$

and

$$N_2(t) = N_2(\tau_L)\epsilon^{-(t-\tau_L)/\tau_{21}} , \qquad \text{for } t > \tau_L , \tag{6.8}$$

where $G = g/(1+g) = g_2/(g_1+g_2)$, and $\tau_{21} = (Q+A)^{-1}$ is the molecular lifetime of the excited state without the external field. The important saturation parameter $S$ is defined to be

$$S = \frac{b_{12} + b_{21}}{Q + A} , \tag{6.9}$$

which measures the ratio of optical driving rate (the absorption and stimulated emission) and the relaxation rate (collisional quenching plus spontaneous emission).

Since the terms $b_{12}$ and $b_{21}$ of the numerator are proportional to $I_L$, $S$ can be written as

$$S = \frac{I_L}{I_{sat}} , \tag{6.10}$$

where $I_{sat}$ is called the saturation irradiance and is given by

$$I_{sat} = \frac{c(Q+A)}{(B_{12}+B_{21})\alpha(\nu_{21})} . \tag{6.11}$$

The ratio of the experimental laser irradiance to the saturation irradiance, $S$, is the characteristic index of the driving force applied to the media. Practically, before

applying a quantitative analysis of a spectroscopic model to a measurement, the spectral saturation irradiance of the detected medium should be evaluated first.

For the laser pulse with a spectral bandwidth greater than the absorption line width (i.e. the broadband excitation), a similar derivation leads to the same results, Equations 6.7 and 6.8, except for some modifications in the expression of the saturation irradiance, $I_{sat}$.

From the results given in Equations 6.7 and 6.8, the excited-state populations, $N_2$ are illustrated for various values of $S$ in Figure 6.4 as the function of time. Since the fluorescence signal is proportional to the excited-state number density, one may consider the time-integrated area of $N_2$ as the relative intensity of the fluorescence signal. As clearly shown in Figure 6.4(c), the time-dependent $N_2$ curves can be described in three consequent periods of time: the excitation period ($0 < t \leq \tau$), the steady-state period ($\tau < t \leq \tau_L$), and the relaxation period ($t \geq \tau_L$). At the third stage, after the laser pulse is ended, the relaxation rates in all the situations are the same ($\tau_{21}^{-1} = Q + A$). The excitation time, in the other hand, depends on the external driving source; i.e., $\tau = \tau_{21}/(1 + S)$. The stronger the excitation is, the faster the population reaches the steady state. When the laser pulse width is shorter than the relaxation time, $\tau_{21}$ (e.g. $\tau_L = 0.2\ \tau_{21}$, as shown in Figure 6.4(a)), the steady state is difficult to achieve before the termination of the driven electric field.

At this point, some of the typical experimental parameters are evaluated and compared to the calculation results shown in Figure 6.4. First of all, the spectral-width and excitation resolution of a typical nanosecond laser is about $0.1 \sim 0.2\ cm^{-1}$ unless an etalon is used. Compared to the absorption line-width of NH molecules in

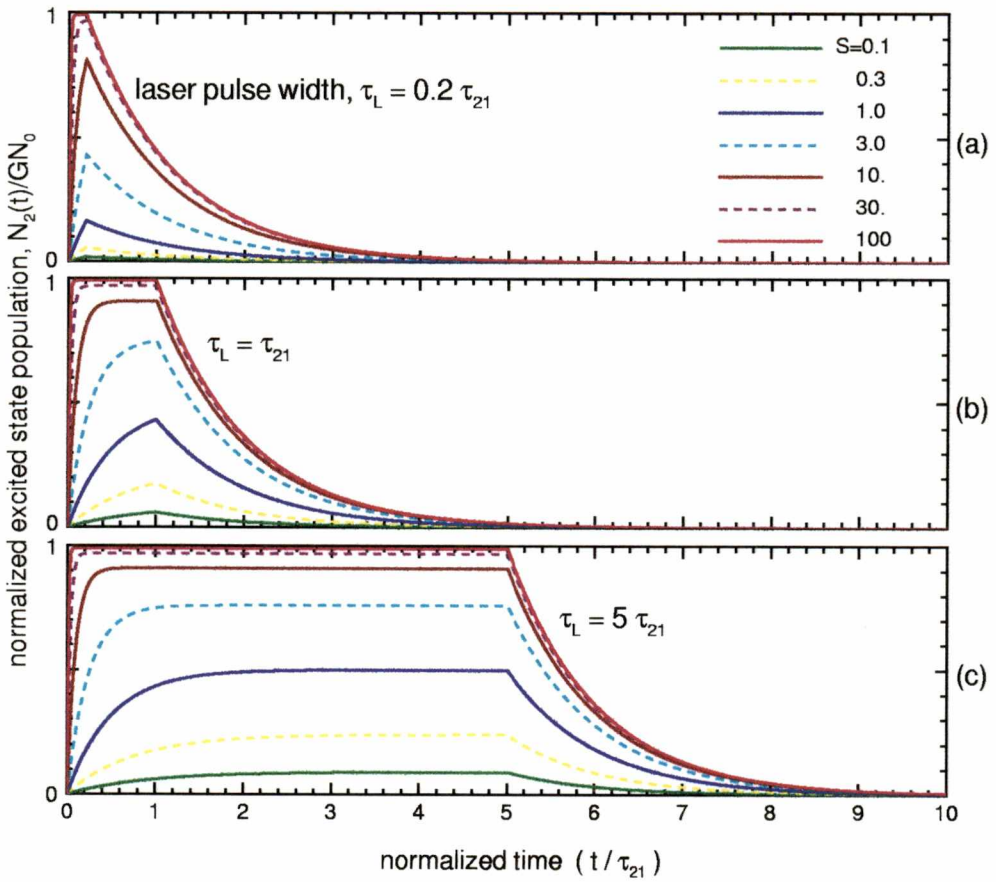



Figure 6.4: Time-dependent excited-state population for molecules pumped by a rectangular-shaped laser pulse of duration $\tau_L$. $\tau_{21}$ = relaxation time. (a) $\tau_L = 0.2\tau_{21}$, (b) $\tau_L = \tau_{21}$, and (c) $\tau_L = 5\tau_{21}$

atmospheric-pressure flame ($\sim 0.4\ cm^{-1}$), we are able to use the simple narrow-band excitation approximation in the LIF derivation. Secondly, to enable the use of the steady-state approximation, the ratio of the laser pulse-width, $\tau_L$, to the relaxation time, $\tau_{21} \approx Q^{-1}$ should be much greater than 1 (see Figure 6.4(a), (b) and (c)). For OH molecules in the atmospheric-pressure flame, the quenching lifetime of the $v' = 0$ and $v' = 1$ levels of the electronic state $A^2\Sigma^+$ are about 0.3$\sim$5 $nsec$ and depend on the rotational quantum number, collision partners and temperature [79, 80, 81]. An average value of 1.5-2.0 $nsec$ is typically measured for OH in flames. For NH molecules under the same condition, the quenching rate and energy-transfer rate parameters are normally reported or assumed to be close to those of the OH molecules [82, 83, 84]. If we take 1.5 $nsec$ for the molecular relaxation time for example, Figure 6.4(a), (b), and (c) illustrate the anticipated experimental results of using 300-picosecond, 1.5-nanosecond, and 7.5-nanosecond lasers respectively. It is very clearly shown in this figure that for a picosecond source pulse, the fluorescence signal does not have a simple relation with the laser pulse function. Normally, the time-dependent calculation and/or short-gate detection ($< \tau_L$) are essential for the ps-LIF study. For the measurement using a nanosecond-laser, the long-pulse excitation normally allows the excited-state population to reach the steady state. If the laser pulse-width is much longer than the excitation and relaxation times ($\simeq \tau \text{and} \tau_{21}$), the fluorescence signal can maintain the temporal profile of the pumping pulse and the simple steady-state calculation can be applied to replace the complicated time-dependent analysis.

The last concern is the laser power, or more accurately, the saturation parameter. Because the saturation irradiance also depends on the quenching conditions such as

pressure, temperature, and collision partners, before these collision conditions are known and the quenching database is sufficiently established, an accurate calculation of $I_{sat}$ or $S$ is not possible. However, the experimentally determined value of $I_{sat}$ is frequently used. The values of the spectral saturation irradiance of NH molecules in the 50-$torr$ flame has been measured and estimated as 2.7 and 2.1 $MW/cm^2/cm^{-1}$ [90, 91]. When the gas pressure is increased, the collision between molecules is stronger. The collision effects tend to reduce the population in the excited state and as a result, saturation become harder to achieve. The increase of saturation irradiance at higher gas pressures depends on the degree of the energy transfer and quenching, as will be described in the following section. For a tunable, nanosecond-laser with a typical output energy in the $mJ$ range, to vary the laser irradiance from $MW/cm^2/cm^{-1}$ to $GW/cm^2/cm^{-1}$ by optical focusing is not difficult. An experimentally determined $I_{sat}$ for the particular molecule of interest can be obtained by varying the probe laser power in LIF experiment.

Assuming steady-state excitation, according to Eq. 6.7, the fluorescence signal is simply

$$\text{LIF(steady state)} = GAN_T(\frac{S}{1+S}) \ , \tag{6.12}$$

or in a more common form

$$\text{LIF(steady state)} = GAN_T(\frac{I_L}{I_L + I_{sat}}) \ . \tag{6.13}$$

From this expression, we realize that the saturation irradiance can be determined by the laser irradiance where the fluorescence signal is half its saturated level, or by

comparing the measured $I_L$ to LIF as shown by Eq. 6.13.

Figure 6.5(a), (b), and (c) show the dependence of the steady state $N_2$ on the saturation parameter, $S$. The logarithmic scale in Figure 6.5(a) shows a wider range of the variable $S$, and the linear scales in (b) and (c) are for more detailed values of the relative intensity of fluorescence. As we will discuss later, the quantitative analysis of LIF is much easier to accomplish under the approximations of either a weak field or a fully saturated excitation. The fluorescence signal is more complicated for the range of the pumping irradiance around $I_{sat}$.

## 6.4 Collisional Effects and the Four-Level Model

The two-level model has been employed in the analysis and measurements in spectroscopic researches for decades. It successfully describes the photon-atom or -molecule interaction for a broad range of applications. However, when the gas pressure increases, one molecule can collide numerous times with other molecules within one nanosecond and these collisions normally alter the number distribution function of the excited molecule. If the collision transfer rates are comparable to or greater than the radiative decay rates, the involvement of more energy levels in the spectroscopic analysis is a consequent result. For an excited state molecule, $X^*$, the collision-caused quenching processes can be divided into physical and chemical types. Physical quenching involves no chemical rearrangement and is a particular subclass of inelastic collisions. Some examples of physical quenching processes are excitation transfer ($X^* + Y \longrightarrow X + Y^*$), ionization ($X^* + Y \longrightarrow X + Y^+ + e^-$) and electronic-

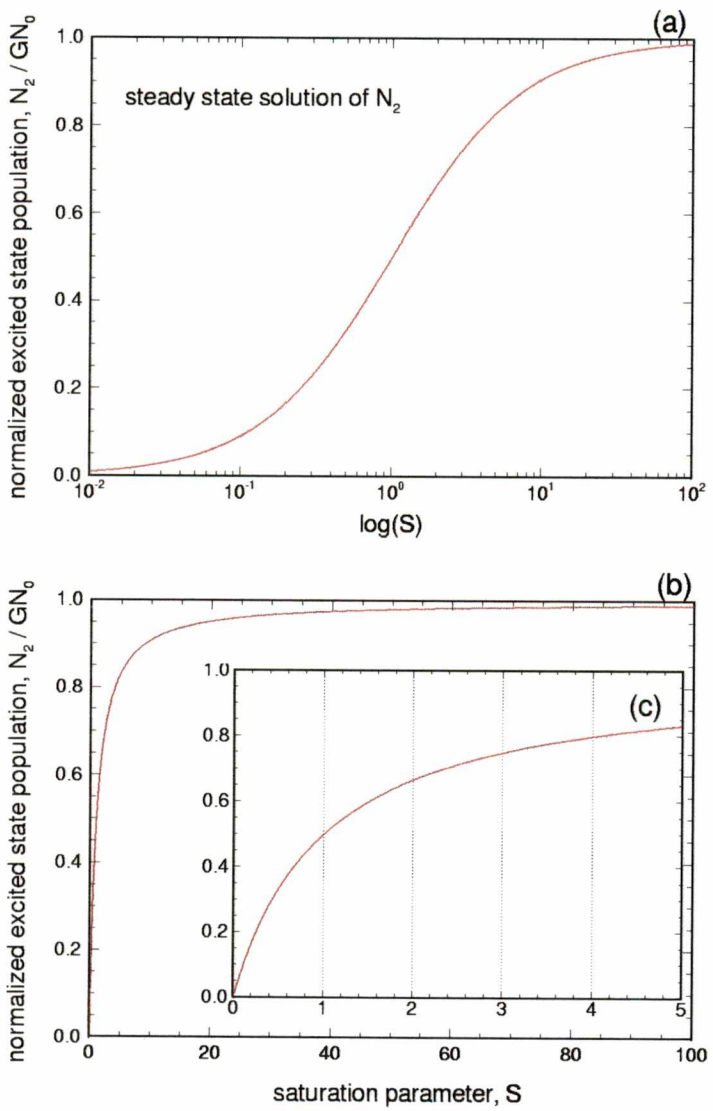



Figure 6.5: Steady-state population as a function of saturation parameter

translational transfer ($X^* + Y \longrightarrow X^{*\prime} + Y$). Chemical quenching processes include associative ionization ($X^* + Y \longrightarrow XY^+ + e^-$), dissociative ionization ($X^* + YZ \longrightarrow XY^+ + Z + e^-$), dissociative deexcitation ($X^* + YZ \longrightarrow X + Y + Z$), etc.. Among all of the collision effects, the impact energy transfer, especially the vibrational and rotational energy transfers, are distinguished from the rest in LIF analysis, for they contribute a significant portion of the fluorescence signal. All the others, which are now called the collisional quenching, remove the molecule from the electronically excited state as a whole so that it does not fluorescence. The impact energy transfer process transfers molecule into a different level, which can then either undergo further collision or emit a photon through the spontaneous radiation. At atmospheric pressure, the rotational and vibrational energy transfers within excited states often occurs quite rapidly so that their rates, $R$ and $V$, and the collisional quenching rate, $Q$ are of the same magnitude.

If we consider only the simplest two-body collisions, the rates of vibrational energy transfer ($V$), rotational energy transfer ($R$) and collisional quenching ($Q$) can all be expressed as the sums over all possible collision partners $i$, of rate constants times number densities $n$.

$$Q = \Sigma_i k_Q(i) n_i \tag{6.14}$$

The rate constant $k_Q$ ($cm^3 sec^{-1}$) can be expressed as

$$k_Q = < \mathrm{v}\sigma_Q > = \int f(\mathrm{v})\mathrm{v}\sigma_Q(\mathrm{v})d\mathrm{v} \ , \tag{6.15}$$

where v is the related velocity between two colliders, $f(\mathrm{v})$ is the distribution function and $\sigma$ is the collision cross section. From this understanding, the quenching and

energy transfer rates are possible to calculate if the concentration $n_i$ of all present species are known, and if we have the collision cross section, $\sigma$, which is in general specific to the initial and final quantum states, of both the colliding molecules. In the other words, the difficulty of computing collisional rates is mostly due to the complicated dependence of collision cross sections on temperature (or the relative velocity, v between two colliders), orientation of colliding molecules, rotational and vibrational quantum numbers of energy states, and the lack of knowledge of the concentration of all important collision partners.

In LIF, an important parameter is the ratio of $V$ and/or $R$ relative to $Q$. If $R$ and/or $V$ are greater than $Q$, an excited molecule will undergo many energy transfers before quenching. The excited state molecules will attain broad energy-level distribution, and then emit fluorescence. If the repopulation in upper state is thermal-like according to the Boltzmann distribution, the fluorescence may be able to yield the temperature in the corresponding spectral region. If $Q$ is greater than $V$, $R$, the initially excited molecules will mostly be quenched before energy transfer, and the fluorescence spectrum will shows large peaks corresponding to lines emitted from that level directly pumped by the laser. This kind of situation is called arrested relaxation or frozen excitation. In either case, the total number of photons emitted per molecule initially excited by the laser is the ratio $A/(A+Q)$. The more detailed discussion of energy transfer and collision quenching effects in atmospheric pressure can be found in the references [75, 92, 93].

Since the energy transfer is in competition with the collisional quenching under a high pressure condition, in addition to the two levels discussed in the previous section,

at least two more energy levels that represent the multi-level baths in the upper and lower electronic states are necessary for the LIF modeling. This type of four-level model for LIF analysis has been used in many studies since 1979 [94, 95] to discuss the energy transfer especially the rotational relaxation effects. The energy transfer rates, $V$ and $R$ are strongly dependent on the energy difference in the transfer process and the molecular temperature. A typical value of the rotational energy transfer rate is in the order of $10^{10}\ sec^{-1}$ [92, 96, 97], and the vibrational energy transfer rate is about one order smaller than the rotational rate in the flame [98]. Figure 6.6 shows the four-level system, in which the rates connecting the levels and manifolds are given. The manifold of energy levels 3 and 4 represent the ensembles or collections of rotational and vibrational levels in the upper and lower electronic states. The downward transfer rates, $D$, are the sum of collisional quenching, $Q$, and spontaneous emission, $A$. Energy transfer rates, $R+V$, are denoted by $T$. The rate equations and conservation of population in this four-level system can be written as

$$\dot{N}_1 = -N_1(b_{12} + T_{14}) + N_2(b_{21} + D_{21}) + N_3 D_{31} + N_4 T_{41} \ , \tag{6.16}$$

$$\dot{N}_2 = N_1 b_{12} - N_2(b_{21} + D_{21} + D_{24} + T_{23}) + N_3 T_{32} \ , \tag{6.17}$$

$$\dot{N}_3 = N_2 T_{23} - N_3(D_{31} + D_{34} + T_{32}) \ , \tag{6.18}$$

$$\dot{N}_4 = N_1 T_{14} + N_2 D_{24} + N_3 D_{34} - N_4 T_{41} \ , \tag{6.19}$$

and

$$N_T = N_1 + N_2 + N_3 + N_4 = N_1^0 + N_4^0 \ , \tag{6.20}$$

where the superscript zero indicates the initial condition (absence of laser pumping).

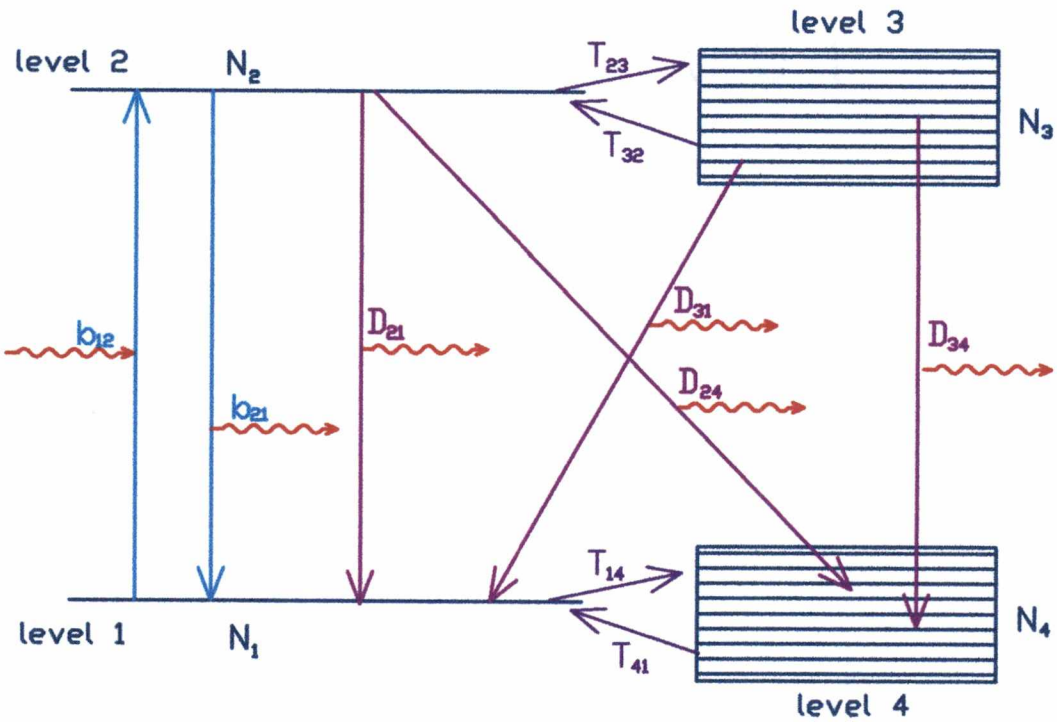



Figure 6.6: Diagram of four energy levels for LIF modeling. $N$ = state population density, $g$ = degeneracy, $D$ = downward transfer rates = $A + Q$, $T$ = energy transfer rates, $b_{12}$ = rates of absorption, $b_{21}$ = rate of stimulated emission.

If we consider the LIF measurement of NH (A-X) system with the resonant excitation in one transition line of the (0-0) P-branch, then levels 1 and 2 in Figure 6.6 correspond to the laser-coupled rotational levels, for example, ($v'' = 0$, $J'' = 11$) and ($v' = 0$, $J' = 10$) in the electronic states $A^3\Pi_i$ and $X^3\Sigma^-$ respectively. The bath levels 3 and 4 represent all the quantum states in vibrational level $v' = 0$ and $v' = 1$ (if vibrational energy transfer is significant) in $A^3\Pi_i$, and $v'' = 0, 1$ in $X^3\Sigma^-$.

For our application, the hot kernel of the ammonia(/oxygen) breakdown, we do not know the collision rates $D$ and $T$ that are required to solve these coupled rate-equations. However, we could assume $D_{31} = D_{21}$, $D_{34} = D_{24}$ and $D = D_{21} + D_{24} = D_{31} + D_{34}$, and expect the downward transfer rate, $D$ in the order of $10^9/sec$. The energy transfer rates $T_{14}$ and $T_{23}$ are approximately on the order of $10^{10}/sec$, and in the steady state without laser pumping, they obey the relation of $N_4^o T_{41} = N_1^o T_{14}$ and $N_3^o T_{32} = N_2^o T_{23}$. To analyze this problem, the weak-field approximation and the saturation approach are mostly applied.

In saturation approach, laser intensity is made sufficiently large so that the absorption and stimulated emission rates $b_{12}$ and $b_{21}$ are much greater than the collision quenching rate which then becomes unimportant (see Eq. 6.13 in the two-level model). Other than the advantage in quenching effects, the saturation excitation generates the strongest fluorescence signal and therefore provides high sensitivity in detecting species of low concentration. Here we refer to the discussion of one saturation approach described by Lucht, *et al.* in 1980 [95]. Lucht, *et al.* introduced a "balanced cross-rate model" in which a modified conservation, $N_1(t) + N_2(t) = constant = N_1^o$ was assumed. They solved the coupled differential equations for $N_2$ in terms of $N_1^o$

and $N_3$. Since laser pulse-width we used for the NH LIF experiment is much larger than the quenching lifetime, we assume that steady-state is approached ($\dot{N}_3 = 0$). Using Eq. 6.18 to eliminate $N_3$ in Lucht's result, we find

$$N_2 = N_1^o(\frac{b_{12}}{b_{12}+b_{21}}) \left[1 + \frac{D(1+\frac{T_{23}}{D+T_{23}})}{b_{12}+b_{21}}\right]^{-1} . \tag{6.21}$$

The factor $b_{12}/(b_{12}+b_{21})$ in the above equation is identical to $G$ in Eq. 6.7 in the two-level system, and Eq. 6.21 has the same form as Eq. 6.7 if the saturation irradiance under strong collisional effect is replaced by

$$I_{sat} = \frac{c(A+Q)}{(B_{12}+B_{21})\alpha(\nu_{21})} \times (1 + \frac{T_{23}}{T_{32}+Q+A}) . \tag{6.22}$$

Eq. 6.22 reduces to Eq. 6.11 when the energy transfer rate is much less than the quenching rate.

This result indicates that if one uses the two-level model to deduce the quenching rate based on the measured saturation intensity, neglect of the energy transfer effects will cause the quenching rate to be overestimated. In other words, the existence of energy transfer in the upper states increases the saturation irradiance and makes the excitation harder to be saturated.

The fluorescence signal we collect from upper states is $F \approx (N_2 + N_3)A$. If we assume the energy transfers in the upper and lower manifolds are similar, then the collected fluorescence from the balanced cross rate model is deduced to be

$$F \approx N_T AG(\frac{I_L}{I_L + I_{sat}}) . \tag{6.23}$$

When applying the saturation approach, the quenching and energy transfer rates are all eliminated from Eq. 6.23. The fluorescence signal reveals the total number density,

$N_T = N_1 + N_4$ of the detected species rather than the population of the directly pumped state, and therefore, loses the information of the molecular temperature.

Many of the saturation LIF measurements made ten years ago applied the two-level model in their analysis. In these studies, the fluorescence signals were collected by integrating the whole temporal profile and over the entire area of the laser beam. The non-saturated fluorescence contributed both temporally and spatially to the signal and led to an overestimated value of saturation irradiance. If saturation LIF is to be applied in the optical breakdown experiment, the temporal and spatial correction for fitting the $I_{sat}$-curve to experiment is necessary.

For LIF in the linear regime, the consideration given by Stepowski and Cottereau (1981) [99] provides another method of analyzing the fluorescence. In Stepowski *et al.*'s time-dependent studies, they assumed that the rotational energy transfer is sufficiently fast compared to the laser pumping (i.e. $b_{12} << R,\ T$), so that the population of level 1 can be maintained at its initial Boltzmann fraction $\beta = N_1/(N_1 + N_4)$.

$$N_1(t) = \beta[N_T - N_u(t)] \ , \tag{6.24}$$

where $N_u = N_2 + N_3$, is the upper state population. By summing Eqs. 6.17 and 6.18, we obtain

$$\begin{aligned} \dot{N}_u &= \dot{N}_2 + \dot{N}_3 = N_1 b_{12} - N_2(b_{21} + D_{21} + D_{24}) - N_3(D_{31} + D_{34}) \\ &= N_1 b_{12} - N_2 b_{21} - N_2 D - N_3 D \\ &= N_1 b_{12} - N_2 b_{21} - N_u D \ . \end{aligned} \tag{6.25}$$

The second term in Eq. 6.25 can be neglected since $N_2 << N_u < N_T$ and $b_{21} << T$,

according to the assumption. With the initial condition, $N_u = 0$, and replacing $N_1$ by Eq. 6.24, Eq. 6.25 can be solved to give

$$N_u = (\frac{b_{12}}{A+Q})\beta N_T[1 - e^{-(A+Q)t}]. \tag{6.26}$$

This result is similar to the results in the two-level model since $\beta N_T = N_1^o$ and $GS/(1+S) = b_{12}/(A+Q+b_{12}+b_{21})$. The magnitude of the fluorescence signal is proportional to the laser energy (as in the linear regime) and to the population of the directly pumped lower state, $N_1^o$. Because of the dependence on the unknown quenching rate $Q$ in the factor $b_{12}/(A+Q)$ (steady state value) of Eq. 6.26, the fluorescence signal will not be able to determine the species concentration directly. However, by monitoring the fluorescence decay after the laser excitation, the quenching rate can be evaluated without knowing rotational transfer rates. The molecular temperature, as described next, is measurable if thermal equilibrium exists for the observed distribution.

## 6.5 Consideration of NH Temperature and Concentration Measurement

The LIF excitation scan is one of the most useful thermometry techniques for steady-state flame applications. In these experiments, a tunable laser with intensity $I_L$ in the linear regime is used to scan over a series of vibration-rotation levels of the ground electronic state. The pump laser excites molecules from the v, J level of the lower electronic state, and the entire fluorescence signal $F_J$ from the upper electronic state is collected. From Eq. 6.26, it is seen that

$$F_J \quad \sim N_J \ ,$$

$$\sim b_{12}\beta N_T \ , \qquad \text{if thermal equilibrium holds,}$$
$$\sim I_L N_T \frac{(2\mathrm{J}+1)\exp(-E_J/kT)}{(\text{partition function})} \ , \tag{6.27}$$

where $\beta$ is the Boltzmann fraction of the laser pumped ground state, J, $N_J$ and $E_J$ are the corresponding rotational quantum number, number density and the rotational energy in the laser-pumped lower state. From Eq. 6.27, it is seen that

$$\ln(\frac{F_J}{(2\mathrm{J}+1)I_L}) = -\frac{E_J}{kT} + \text{constant} \ , \tag{6.28}$$

and that $T$ is determined by measuring the slope of the left-hand side of Eq. 6.28 when plotted versus $E_J$. This so-called Boltzmann-Plot for temperature measurement is also employed in many other spectroscopic analyses.

For the two-dimensional NH temperature determination using the method of the excitation scan, only 10 rotational transition lines (plus 10 positions for background determination) are picked to accomplish this task. The required considerations for this measurement are listed below:

1. The spatial distributions of the NH molecules (temperature and concentration) must be steady during the period of laser scan.

2. Laser intensity is in the linear regime, i.e. where the fluorescence signal is proportional to the laser power.

3. Local thermal equilibrium (LTE) is assumed.

4. Laser pulse-width $\tau_L$ is larger than the excitation time $\tau$ so that the steady-state approximation of LIF can be applied. As we discussed in the previous

section, the excitation time is expected to be no larger than 1~2 $ns$. Therefore, a nanosecond laser with pulse-width of $\sim$ 10$ns$ is used to perform the NH temperature measurement.

5. Narrow-band excitation is applied. From the excitation spectra of both ammonia/oxygen flame and ammonia breakdown, which will be discussed in the next chapter, the absorption line-width ($\sim 0.4 cm^{-1}$) is about 2-3 times larger than the spectral resolution of pumping laser, which indicates the assumption of narrow-band excitation.

6. Einstein $A$ coefficients are assumed to be the same over the energy-transfer manifold and the scanned upper states. According to the NH line strength database, the difference of the Einstein A coefficients among all of the selected transition lines are found less than 4%.

7. The photon energy of the NH($A^3\Pi_i$-$X^3\Sigma^-$) emission ($h\nu \sim 29,300\ cm^{-1}$) is much larger than the energy difference in the energy-transfer manifold ($\sim kT \sim 2,100\ cm^{-1}$ at 3000 K) and the region of the scanned upper levels ($\sim 2,800\ cm^{-1}$) so that we can assume that all of the single fluorescence from the scanned transition lines contribute equally to the signal.

8. Crosley and Smith (1982) have demonstrated that using the narrow band-pass detector centered to collect the maximum fluorescence, the discrimination against the fluorescence from the higher rotational states leads to incorrectly low temperature measurement [85, 92]. Since the fluorescence signals from all the upper electronic states are required to be collected with equal weights, a wide

spectral bandpass in the detection system is essential. In the experiments of temperature images of our research, a broad band-pass detector system which integrates the signal over 280-380 $nm$ region was used. The collected fluorescence signal covers (0-0), (1-1), (2-2), (1-0), and (0-1) bands of NH (A-X) system.

9. To prevent multiple excitation in NH molecules, the rotational transition lines are carefully selected according to our spectrum calculation. As mentioned, in the high-pressure environment, wide bandpass detection is necessary. If the pumping laser pulse excites NH with other molecules, the fluorescence produced from other species will be easily collected simultaneously and confuse the analysis of temperature and concentration measurement. For this reason, we compared the transition lines of NH with the synthetic spectra of OH (A-X) and $N_2$ (second positive) to reduce the possibility of multi-species excitation. Moreover, the excitation spectrum shown in Figure 6.2 is an important reference for examining the presence of multi-species excitations.

Similar to the temperature measurement, the NH concentration measurement should avoid multiple and multi-species excitation. Since the signal of laser-induced fluorescence yields the number density of the directly pumped lower level, the total molecular concentration can be achieved from the Boltzmann expression once the temperature has been determined. The laser-induced fluorescence signal from the upper electronic state is given by

$$F = \int h\nu N_u A \mathrm{V} \frac{\Omega}{4\pi} \Theta(\theta, \phi) dt \ , \tag{6.29}$$

where $h\nu$ is the energy of photon, V and $\Omega$ are the detected volume and solid angle; $\Theta$ represents the angular distribution due to the polarization of pumped molecules. In LIF measurements, the NH fluorescence signal is collected in the 90° direction with respect to the exciting beam. Because the exciting laser beam is linearly polarized, the emission transition dipole is essentially parallel to the absorption transition dipole in a collision-free environment. The molecular rotation itself can reduce the degree of anisotropy [100] (i.e. $\Theta$ depends on the rotational quantum number of the state). The collision effects also reduce the degree of polarization, by either elastic dephasing [101] or collision-caused energy transfers [102], further decreasing the degree of anisotropy. As we measured in our NH LIF experiments in which a rotatable polarizer was placed in front of the detection system, the polarization of the fluorescence signal from the ammonia breakdown kernel is practically isotropic. Therefore, the angular distribution function $\Theta$ can be eliminated from Eq. 6.29.

NH concentration measurements may be achieved by either linear-regime or saturation approaches. For the measurement in the linear-regime, Eq. 6.26 can be incorporated into Eq. 6.29. Since the laser pulse is much longer than the excitation time in NH LIF, the steady-state solution can be used to simplify the equation. The appropriate quantities of collision-quenching rates and the molecular temperature are needed for an accurate evaluation of concentration. If the data of quenching rate is not available, only the relative concentration can be obtained.

For measurements in the saturation regime, the laser irradiance is required to be much higher than the saturation irradiance. Under this approach, the relation of unknown quenching rate and energy transfer rate can be eliminated from the LIF

equation. However, the expression for the saturation fluorescence signal requires the spatial and temporal correction as described in last section.

# Chapter 7

# Time-Resolved Images Using Spectroscopic Techniques

The developing features of the optical breakdown kernel have been studied in Chapter 5 using the shadowgraph technique. In this chapter, we present time-resolved images of the breakdown and ignition kernel using the spectroscopic techniques of Rayleigh scattering, spontaneous emission, and planar laser-induced fluorescence (PLIF) techniques. As described in Chapter 6, the laser-induced fluorescence (LIF) technique can be used to detect species temperature and concentration nonintrusively. The PLIF images are achieved by applying a sheet-beam probe laser in conjunction with a two-dimensional detection system. For a transient event, the PLIF images can be acquired at a selected time delay with a relative short exposure time. Time-resolved PLIF images can then provide the spatial distribution of atoms and molecules throughout the ignition process [23, 103] and in the turbulent combustion phase of the kernel development [104, 105]. In the following sections, we not only present the time-resolved PLIF images of NH molecules in ammonia(/oxygen) breakdown kernels, but also give the quantitative temperature and concentration profiles. The optical, chemical, and

thermodynamic properties of the ammonia(/oxygen) breakdown kernels are further investigated.

## 7.1 Experiment Details

The experimental setup for the spectroscopic study of laser-induced gas breakdown is shown in Figure 7.1. Most of the experimental equipment in the figure has been described in previous chapters. The Nd:YAG (Continuum YG680S) laser system and optics were arranged to induce optical breakdowns with a laser-pulse repetition rate of 10 $Hz$ focused at a position 1 $cm$ above the flat-flame burner. The gas-flow meters and the burner were set up to provide a laminar core flow of ammonia(/oxygen) with flow speed of 6.0 $cm/sec$. The equipment for the spectroscopic diagnostics includes a probe laser system, a spectrometer system, and an intensified-CCD camera system. For the acquisition of the spontaneous radiation images, the intensified-CCD camera and the two-dimensional optical multi-channel analyzer (EG&G PARC OMA4, Model No. 1530-CUV) were used to record the images of the kernel in the direction of 76° with respect to the YAG laser beam. A narrow band-pass filter ($\Delta\lambda \sim 10\ nm$) centered at 337 $nm$ was mounted in front of the detector for the NH(A-X) $\Delta v = 0$ radiation. The transmission functions of the filters and the synthetic spectra of NH, OH, and $N_2$ are shown in Figure 7.2. The detected spontaneous radiation images from the plasma kernel included a certain percentage of the $N_2$ Second Positive radiation through the narrow band-pass filter. The combined spectra of NH and $N_2$ has been investigated in a previous study [18]. For the experiments of the NH PLIF, an excimer-pumped dye-laser system (as described in Chapter 4) was tuned to resonantly excite NH

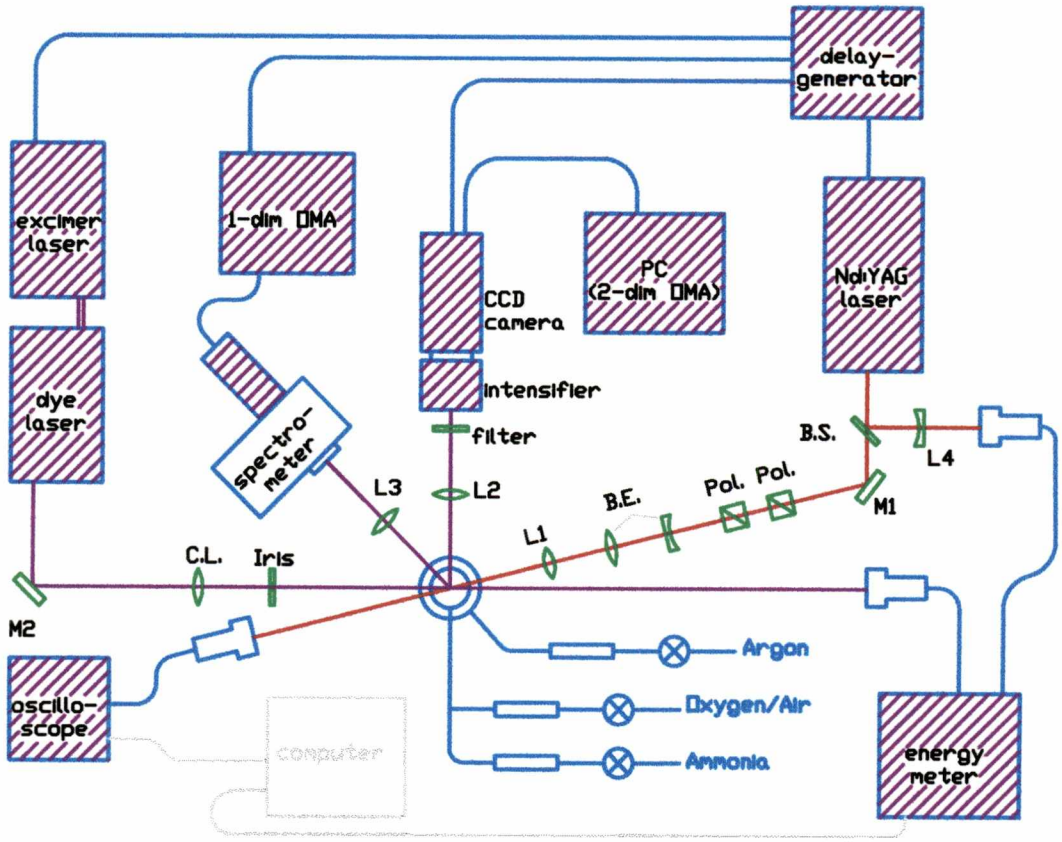



Figure 7.1: Experimental geometry in the study of energy absorption, B.S.= beam splitter, E1 = energy meter (Laser Precision, Model Number RJP-734), E2 = energy meter (Scientech, Model Number P50), M = mirror, Pol.= polarizer, B.E.= beam expander, L = lens

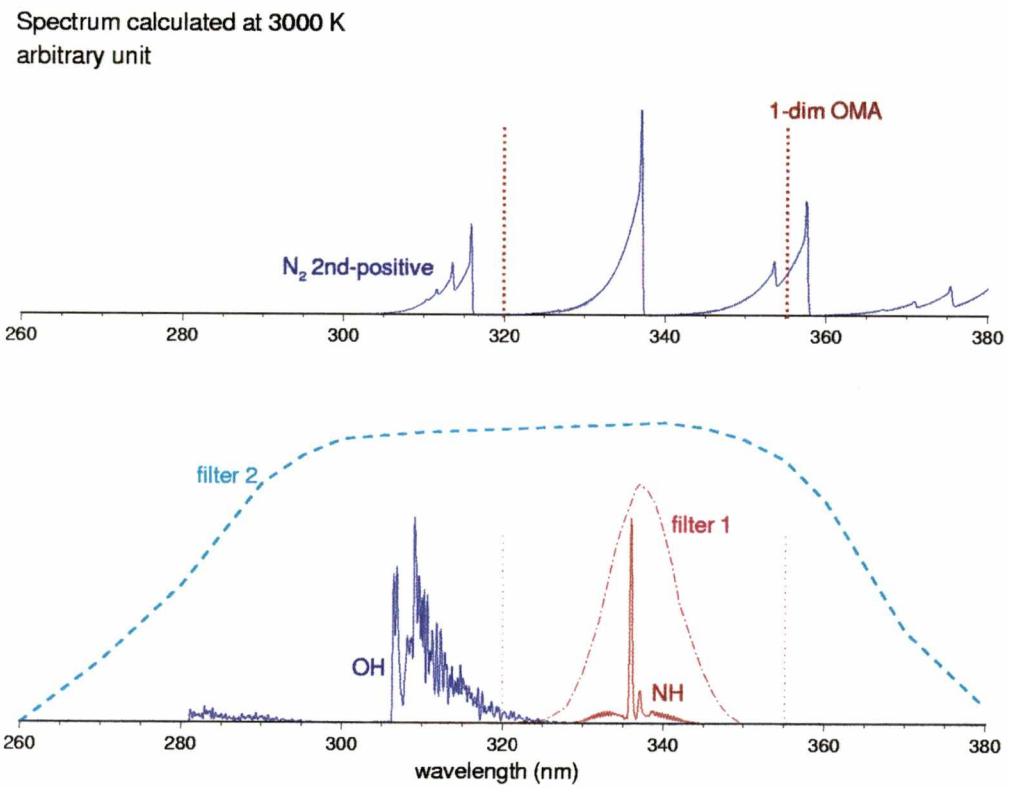



Figure 7.2: Synthetic spectra of NH(A-X), OH(A-X) and $N_2(2^{nd}$ Positive). relative transmissions of narrow band-pass filter for NH(A-X) PLIF experiments, broad band-pass filter for NH temperature experiments, and 1-dimensional OMA (red dotted lines) for excitation scan experiments

molecules in the breakdown kernels. The dye laser beam was focused into a sheet beam and transmitted through the center of the kernel with an angle of $14^o$ with respect to the optical axis of the YAG laser beam. Across the kernel's cross section, the induced fluorescence signals were imaged into the CCD camera system. When the PLIF images were acquired for the purpose of the two-dimensional temperature calculation, a broad band-pass filter was used (see Figure 7.2) to replace the narrow band-pass one. The two-dimensional OMA was calibrated and linearity of the response was ensured (see Appendix A). The Rayleigh (or Mie) scattering images were obtained by tuning the dye-laser to the off-resonant wavelengths of the molecules. The table below describes the relation of these three types of images and their background noise.

| 2-Dimensional Images | Experiment Setup | Background Noise |
|---|---|---|
| Spontaneous Emission = ion-$e^-$ spectrum ($< 2\mu s$) + $NH^*$ radiation ($< 20\mu s$) | laser-induced breakdown (LIB) | system noise |
| Rayleigh and Mie scattering | LIB + probe-laser (at off-resonant wavelength) | spontaneous emission from the kernel + system noise |
| NH fluorescence (PLIF) | LIB + probe-laser (for NH resonant excitation) | Rayleigh and Mie + spontaneous emission + system noise |

In the experiments of the laser-induced fluorescence excitation scan, the Nd:YAG laser was operated with a repetition rate of 10 $Hz$. The narrow band ($\Delta\lambda < 0.002\ nm$ or $\Delta\nu < 0.2\ cm^{-1}$) tunable dye-laser was scanned across the P-branch of the NH(A-X) transitions from 337 to 344 $nm$ with the step-speed of 0.001 $nm/sec$. The focused dye-laser sheet beam passed through each breakdown kernel at a 5-$\mu sec$ delay time after the YAG laser induced the breakdown. The signal of the induced NH fluorescence

was focused on the entrance slit of a spectrometer (Jarrell-Ash Monospec27, with photodiode array: EG&G PARC, Model No. 1423), and the one-dimensional OMA (1D-OMA: EG&G PARC, Model No. 1460) recorded it simultaneously with the laser scanning. The spectral detection range of the spectrometer in the experiment was selected to be 320-355 $nm$, as shown in Figure 7.2.

The timing control between Nd:YAG laser pulses and the detection systems is shown in Figure 7.3.

## 7.2 Time-Resolved Images of NH Spontaneous Emission and PLIF

Time-resolved images of NH spontaneous radiation and NH PLIF in laser-induced ammonia breakdowns are shown in Figure 7.4 and Figure 7.5. In these two figures, each image is scaled 4 $mm$ by 4 $mm$. The Nd:YAG laser pulse was incident from the left for each image with the pulse energy of 32 $mJ$ (corresponding to the absorption of 26 $mJ$). The burner is located at the lower side, 10 $mm$ below the breakdown axis. As mentioned and shown in previous figure, 4.7, the radiation at the earliest 2 $\mu sec$ contains great amount of continuoum spectrum contributed mostly from the recombination process of the ions and electrons. After a couple of microseconds, the spontaneous emission images illustrate the spatial distribution of the NH molecules in the electronic excited state, $A^3\Pi_i$. The PLIF images, on the other hand, present the location of the ground state ($X^3\Sigma^-$) NH populations as discussed in Chapter 6. Instead of dwelling in the center of breakdown kernel as shown in the spontaneous radiation images, the ground state NH molecules are located in a layer surrounding

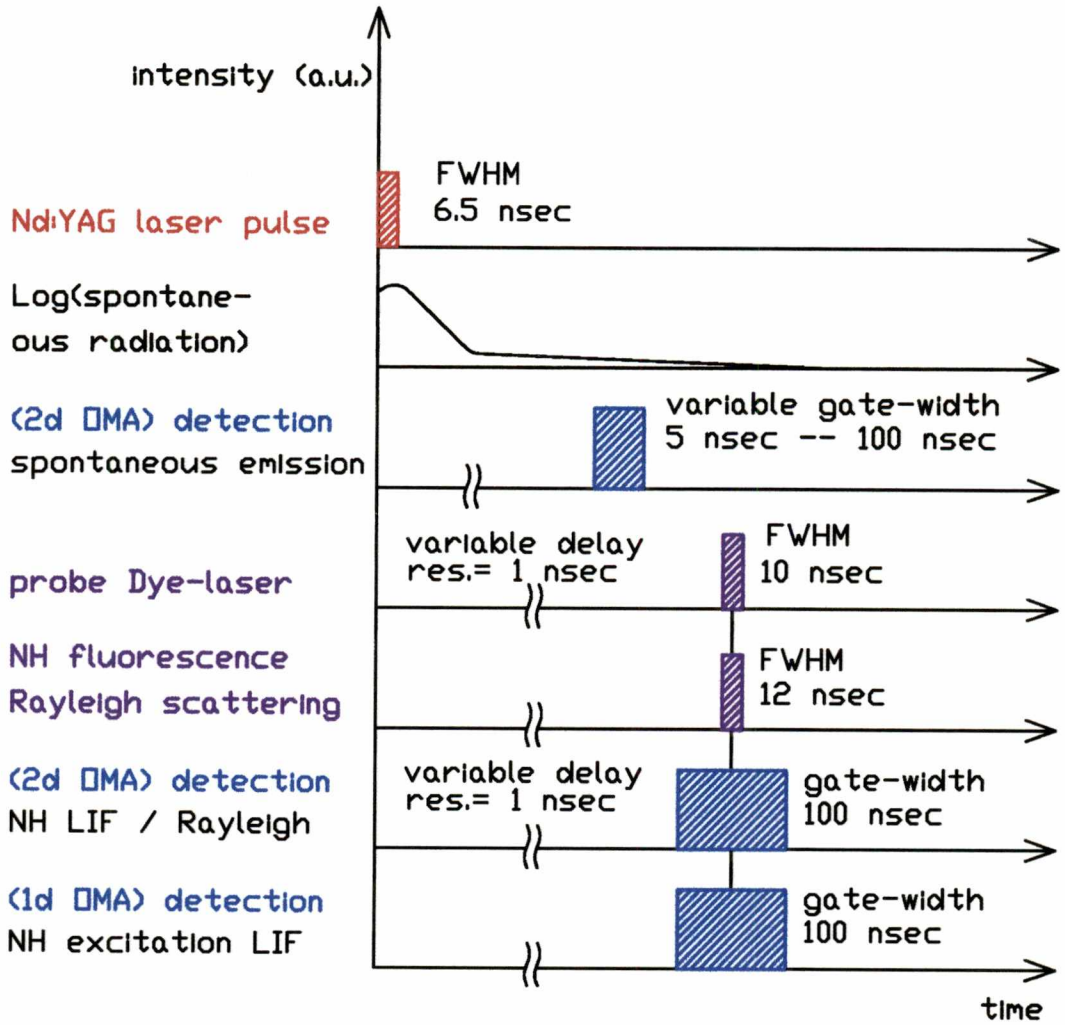



Figure 7.3: Timing control in the experiments of spontaneous emission, laser-induced fluorescence, and Rayleigh scattering

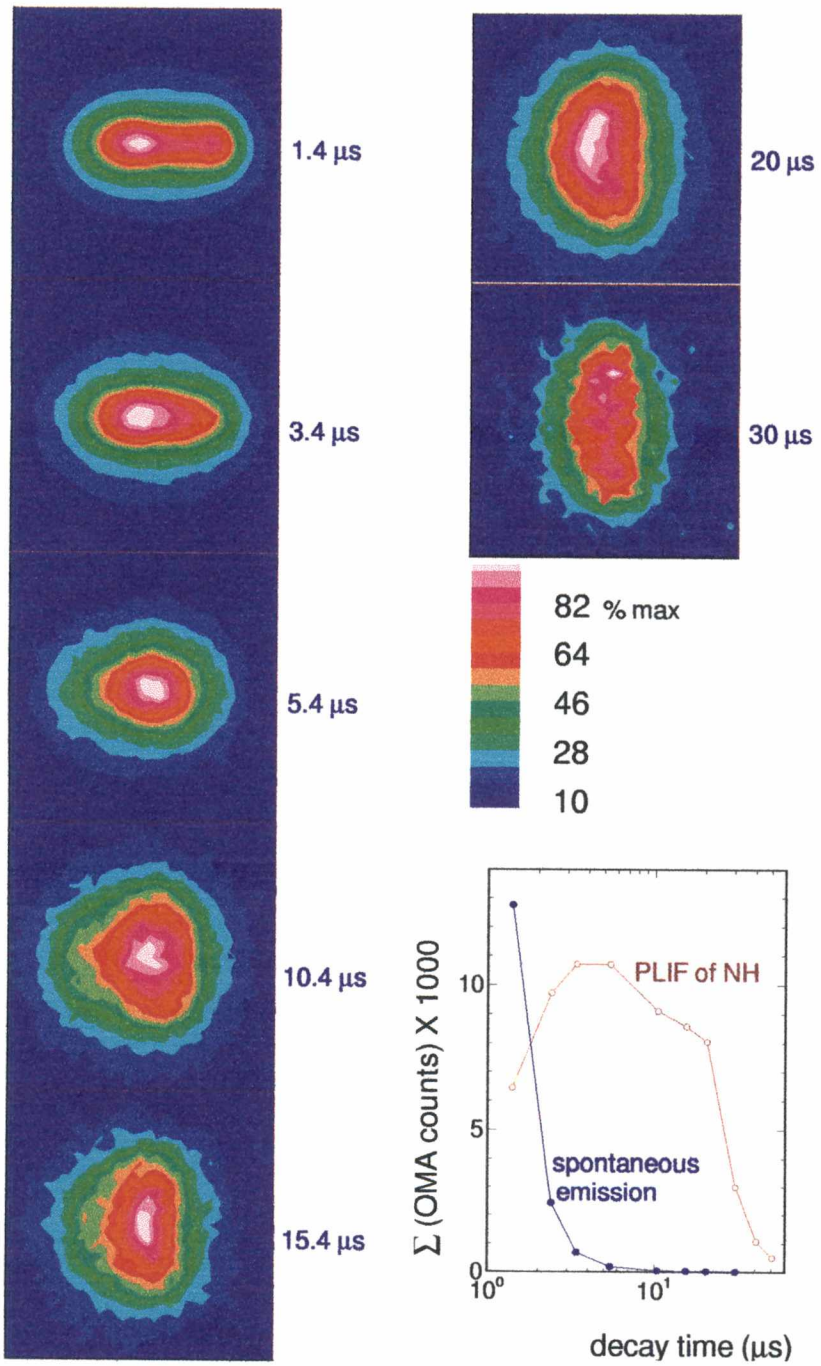



Figure 7.4: Images of NH(A-X) spontaneous emission in laser-induced ammonia breakdown

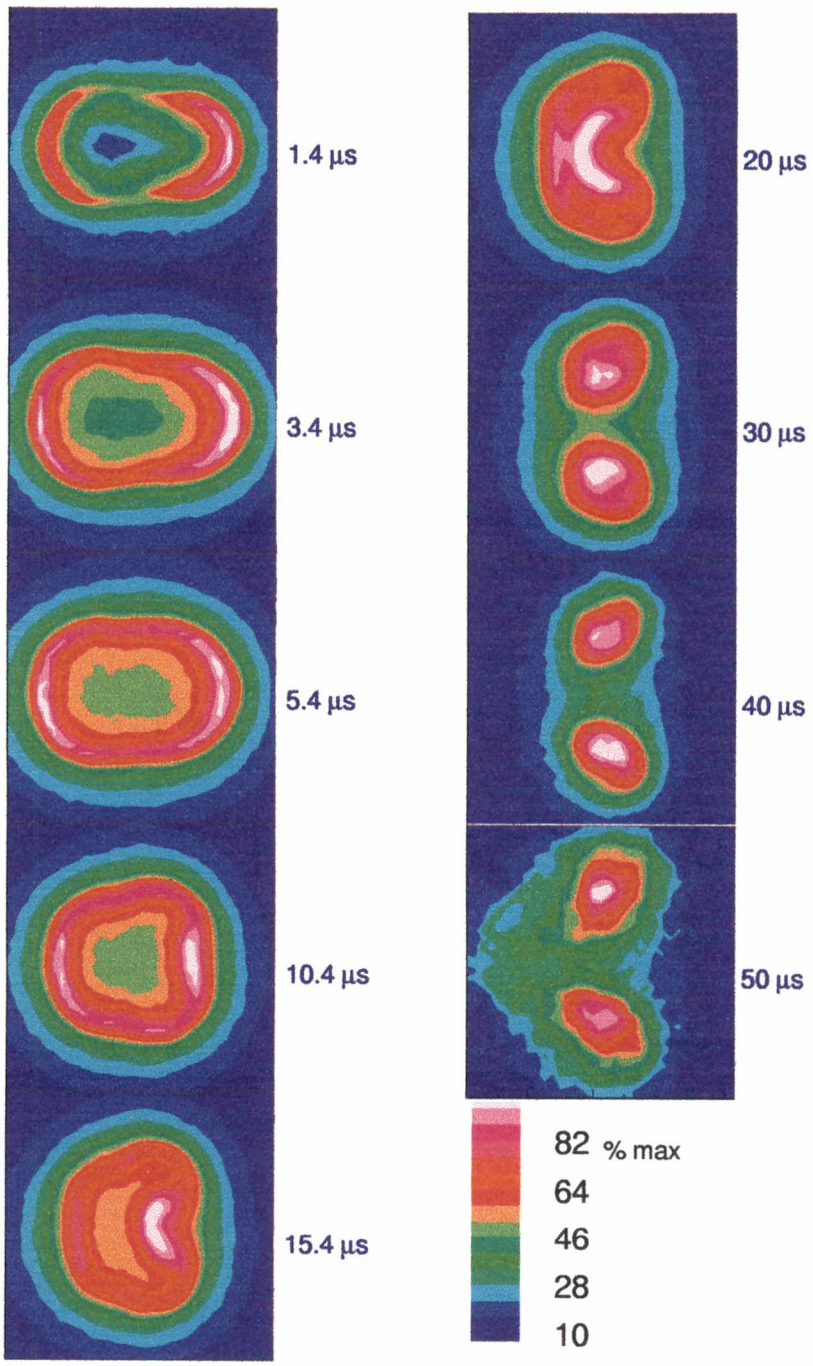



Figure 7.5: Images of NH(A-X) planar laser-induced fluorescence in laser-induced ammonia breakdown

the hot gas kernel. The fluorescence intensity of NH(X) in the center of the kernel is less than one half of that in the outer shell layer. Suppose the concentration of the ground state NH(X) in the center of the kernel is one half of that near the boundary, and assume the molecular temperature is approximately 3500K and 2700K at these two locations, respectively. For the condition of local thermal equilibrium, the population of the electronic excited state NH(A) in the core would be approximately 18 times larger than in the boundary. Therefore, the information carried in the spontaneous emission images is more likely to be determined by the temperature gradient than the NH distribution. The plot in the lower-right corner of Figure 7.4 shows the comparison of the magnitudes of the spontaneous emission from the excited state NH(A) and the fluorescence signal from the ground state NH(X). When the kernel temperature drops after 2 $\mu sec$, the density of the ground state NH molecules increases and maintains its magnitude for about 40 $\mu sec$ of time before decaying.

The back-streaming structure of the kernel appears around 10 $\mu sec$ of delay time in both sets of images, although the feature is not very clearly shown from the spontaneous radiation images. From the PLIF images, we can observe the formation of the toroidal geometry from both sides of the kernel. A stronger gaseous force pushing the plasma kernel from the back (right) appears at 10 $\mu sec$ of time, and a weaker motion from the front (left) side appears at approximately 20 $\mu sec$ of delay time. In the radial direction, too, the kernel seems to expand more significantly in the back than in the front. A tunnel is formed along the axis around 40 $\mu sec$ delay time in the PLIF images, which can also be observed in the shadowgraphs in Figure 5.2.

The PLIF images of laser ignition are shown in Figure 7.6. The experimental

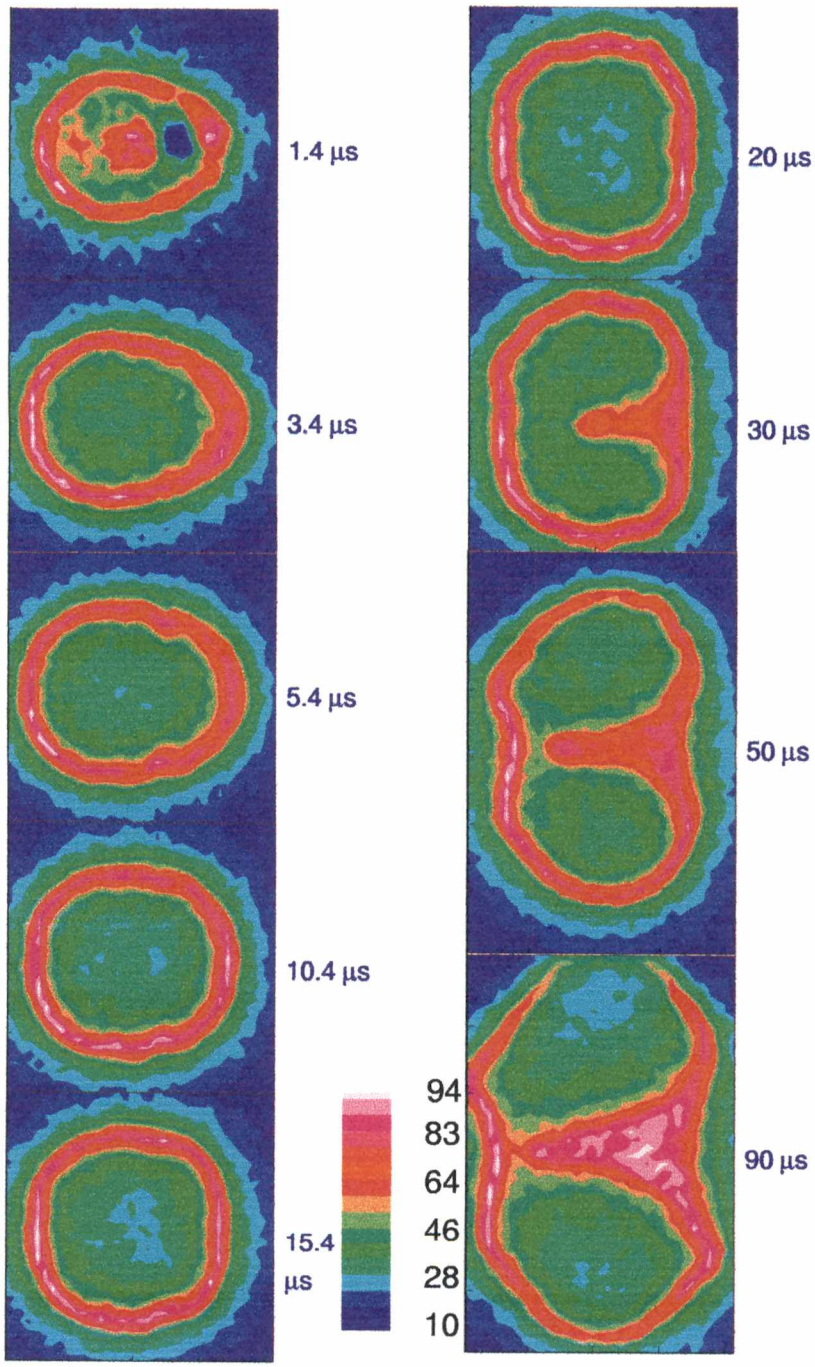



Figure 7.6: Images of NH(A-X) planar laser-induced fluorescence in laser-induced ammonia/oxygen ignition

conditions are the same as that in Figure 7.5 except that the premixed ammonia/oxygen ($\Phi$=1.0) flow is combustible, and chemically reacts following ignition by the laser pulse. The sizes of images corresponding to a 50 and a 90 $\mu sec$ delay are both 4×6 $mm$. As in Figure 7.5, the image recorded at 1.4 $\mu sec$ of delay time suffers from strong background noise from the spontaneous emissions in the center of the kernel, and can not illustrate the proper intensity around this location. The shapes of the expanded plasma kernels in the earliest 2 $\mu sec$ clearly have developed differently between ignition and non-ignition breakdowns. In contrast to the pure ammonia breakdown, the size of the hot kernel of the combusting mixture is bigger, and the NH-molecule layer is thinner in the ignition kernel, which imply a stronger expanding pressure and temperature gradient than found for the pure ammonia case. The fluorescence signal in the core of the ignition kernel is apparently weaker than the pure ammonia breakdown due to the lower mole fraction of the participating N and H atoms. Around 10$\sim$ 20 $\mu sec$ of time, the kernel front has developed into a self-sustained flame front. As a result, the NH molecules are supplied through the chemical reactions in ammonia/oxygen flame, and the total intensity of NH fluorescence continuously increases instead of decaying away as in the pure ammonia breakdown.

As in figures 7.5 and 7.6, a significant concentration of the ground state NH molecules seems to exist in the interface between the hot-gas kernel and the ambient ammonia gas, which suggests a possible formation procedure through the combustion reaction chemistry rather than the recombination of atoms in the kernel. The feature of the NH shell layer appears as early as one microsecond of time from the laser

pulse. The generation of NH through heating requires the breaking of two N-H bonds in the ambient ammonia molecules. Through the recombination process, on the other hand, NH molecules could appear in a very early time following the breakdown. In Figure 7.6, the ignition delay time (while the NH signal starts to increase) at $\Phi = 1$ condition is observed around 20 $\mu sec$, which indicates, roughly, the beginning stages of combustion or chemical reactions. In the very early period of time ($< 5\mu sec$), the atom recombination process is probably the major supplier of the NH(X) molecules. The temperature dependence of recombination-generated molecules may explain the cause of the NH distribution near the surface of the hot gas kernel. In the other words, the density of ions, electrons, atoms, and molecules inside the breakdown kernel are dependent on the local temperature. The NH molecule is more difficult to form near the very hot core than in the outer area where the temperature is right for its formation. If we compare the kernel sizes in NH PLIF images with the shadowgraphs in Chapter 5, the NH-molecule shell, in fact, is formed inside the kernel. Many numerical analyses of the development of electric sparks show the dependence of the temperature and the concentration of various transient species and the molecular shell layers are also predicted [106, 107].

## 7.3 NH Temperature and Concentration Images

As discussed in Chapter 6, the NH rotational temperature can be determined using the spectroscopic technique of LIF excitation scan. An experimental excitation spectrum of NH taken in ammonia/oxygen flame has been shown in Figure 6.2, in Chapter 6. In the pure ammonia ' breakdowns, the excitation spectrum of NH molecules at 5

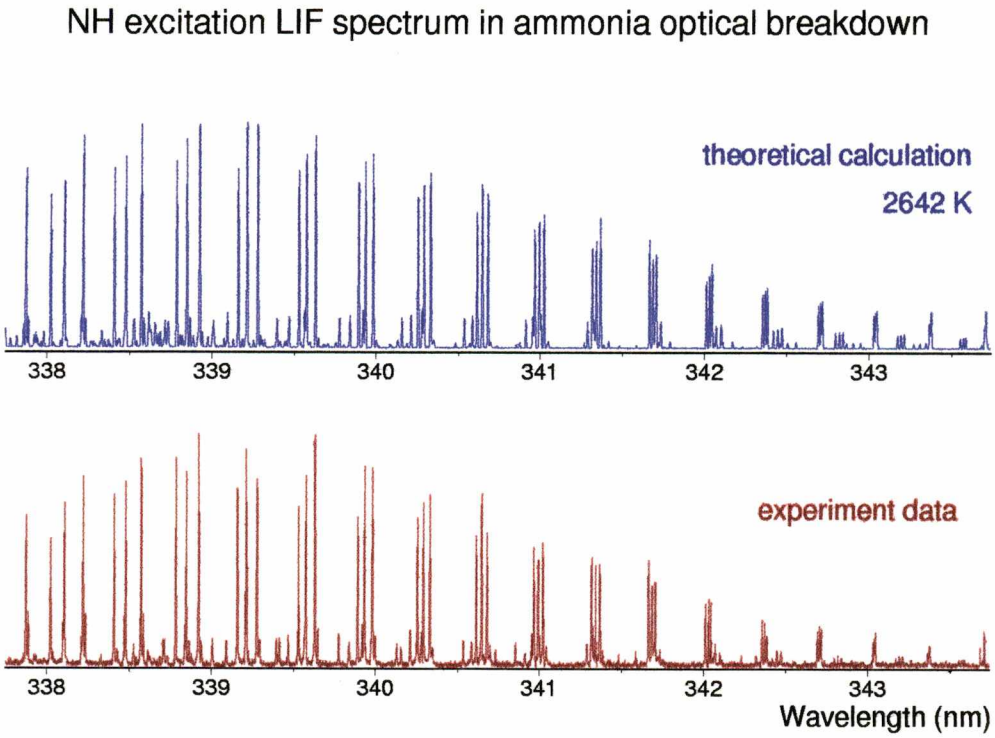



Figure 7.7: NH excitation spectra in atmospheric-pressure laser-induced ammonia breakdowns

$\mu sec$ delay time are shown with the computed spectrum in Figure 7.7. Over the excitation area of the probe laser beam, the NH molecules contribute the fluorescence signal, which corresponds to a certain range of temperature distribution. To reduce the strong background noise in the wavelength range of the probe laser, only the fluorescence signal in Q- and R-branches of the (0-0) band of NH was collected in this measurement. Therefore, the excitation spectrum is used to determine, or locate, some clean, non-overlapped transition lines for the temperature measurements and to determine if multi-species excitation has occurred, rather than determining the temperature itself. To prevent multi-species excitation, the computed spectral lines of electronic transitions of molecules $N_2$ and OH were carefully compared with NH excitation spectra and NH calculation result. No significant involvement of multi-species excitation was found in either experiments of the atmospheric pressure $NH_3/O_2$ flames or the pure $NH_3$ breakdowns. Ten selected transition lines in the P-branch of NH(A-X) $\Delta v = 0$ were used in the two-dimensional temperature measurements of ammonia breakdowns. Corresponding to each of the selected excitation lines, an off-resonant point was chosen for the background determination (see the excitation spectrum in Figures 7.7 and 6.2). The parameters of these transition lines that were used are listed in the following table [71, 72]:

| Type | $\lambda$ $(nm)$ | N″/J″ | Term″ $(cm^{-1})$ | A $(sec^{-1})$ | Bkg. $\lambda$ $(nm)$ |
|---|---|---|---|---|---|
| $P_{33}$ | 339.5275 | 10/09 | 3399.77 | 1.1367 e+6 | 339.488 |
| $P_{11}$ | 339.6293 | 10/11 | 3398.74 | 1.1013 e+6 | 339.488 |
| $P_{11}$ | 339.9804 | 11/12 | 3749.29 | 1.1103 e+6 | 340.020 |
| $P_{33}$ | 340.2539 | 12/11 | 4131.13 | 1.1422 e+6 | 340.404 |
| $P_{33}$ | 340.6117 | 13/12 | 4541.41 | 1.1433 e+6 | 340.502 |
| $P_{11}$ | 341.0226 | 14/15 | 4979.33 | 1.1244 e+6 | 341.143 |
| $P_{33}$ | 341.3171 | 15/14 | 5448.67 | 1.1434 e+6 | 341.237 |
| $P_{22}$ | 341.6862 | 16/16 | 5944.69 | 1.1244 e+6 | 341.546 |
| $P_{33}$ | 342.0100 | 17/16 | 6467.81 | 1.1417 e+6 | 341.960 |
| $P_{22}$ | 342.0281 | 17/17 | 6467.90 | 1.1254 e+6 | 341.960 |

The subscripts of the transition types $P_{ij}$ indicate the triplet splitting of the corresponding rotational states in the upper ($A^3\Pi_i$) and lower ($X^3\Sigma^-$) electronic states. The given term values are the lower-state energy levels of the corresponding transitions. The variation of Einstein A coefficients between the selected transitions is very small. Over the wavelength range of ten excitation lines, the pulse energy of the probe dye laser is not constant. The output power varies over this spectral region by about 10%. For excitations in the linear optical interaction regimes, since the fluorescence intensity is proportional to the laser intensity, the wavelength-variation of the dye laser power can be easily corrected between these ten transitions. The saturation irradiance in the ammonia breakdown needs to be determined prior to the temperature measurements. Measurements of the saturation intensity were carried out in both the ammonia/oxygen flame and the pure ammonia breakdown. In both experiments, simple two-level models were applied, and the fluorescence signals were integrated over the temporal and spatial regions of the excitation, which may lead to an over-estimatation of the saturation intensity. These experimental results are shown

in Figures 7.8 and 7.9, and the saturation irradiance of $\simeq 12$ and $\simeq 22\ MW/cm^2/cm^{-1}$ was determined for ammonia/oxygen flame and ammonia breakdown, respectively. These two values are about five and nine times larger than what was reported in a 50-torr flame [90, 91]. When the gas pressure increases, the collisional energy transfers increase the saturation irradiance by a factor of $\simeq (1 + T/Q)$ (see Eq. 6.22). If we consider a similar magnitude of energy transfer rate for NH relative to the calculated OH rotational energy transfer time of 350 picosecond in 3000 $K$ methane/oxygen flame [96], and the measured value of 600 picosecond for OH(A), J' = 10 state [97], an energy transfer time $1/T$ for NH should correspond to a few hundreds picoseconds. Compared with the quenching time of $1.5\sim 2\ nsec$ for both OH and NH molecules, an increase in the saturation irradiance of a factor less than 10 at atmospheric pressure is expected.

For the acquisition of the two-dimensional temperature images, the irradiance of the dye-laser sheet beam was operated at about one half of the measured saturation irradiance, $I_L \approx 0.5 I_{sat}$. Each of the ten PLIF images used to determine the temperature maps was acquired by accumulating fluorescence signals over 500 breakdowns events to achieve the spatially stable distribution. The background images, as mentioned, were subtracted by tuning the dye-laser wavelength to off-resonance for each transition line. The scale of each PLIF image in the temperature measurements is 4.42 $mm$ in both horizontal and vertical directions, and the images were recorded in 70×70 pixels. By applying the Boltzmann plot at each recorded point (pixel), the two-dimensional temperature images were obtained. Two sets of time-resolved temperature images with incident Nd:YAG laser energy of 21 and 32 $mJ$ are

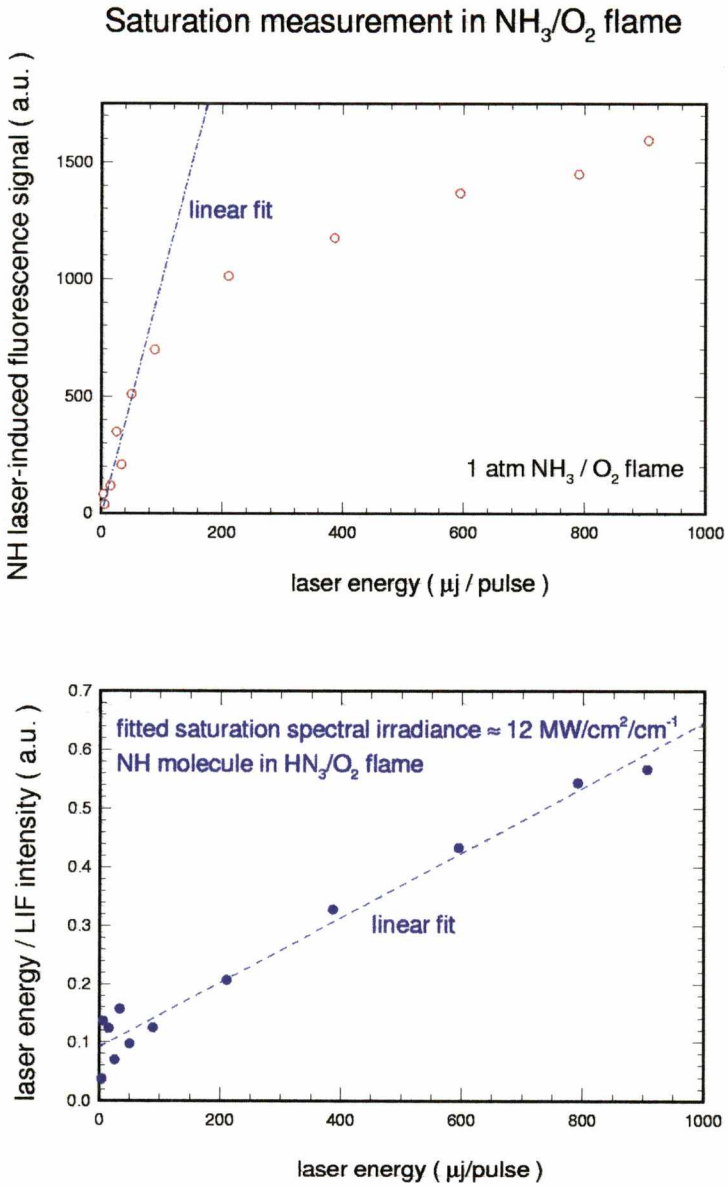



Figure 7.8: Measurement of LIF saturation irradiance in atmospheric pressure ammonia/oxygen flame

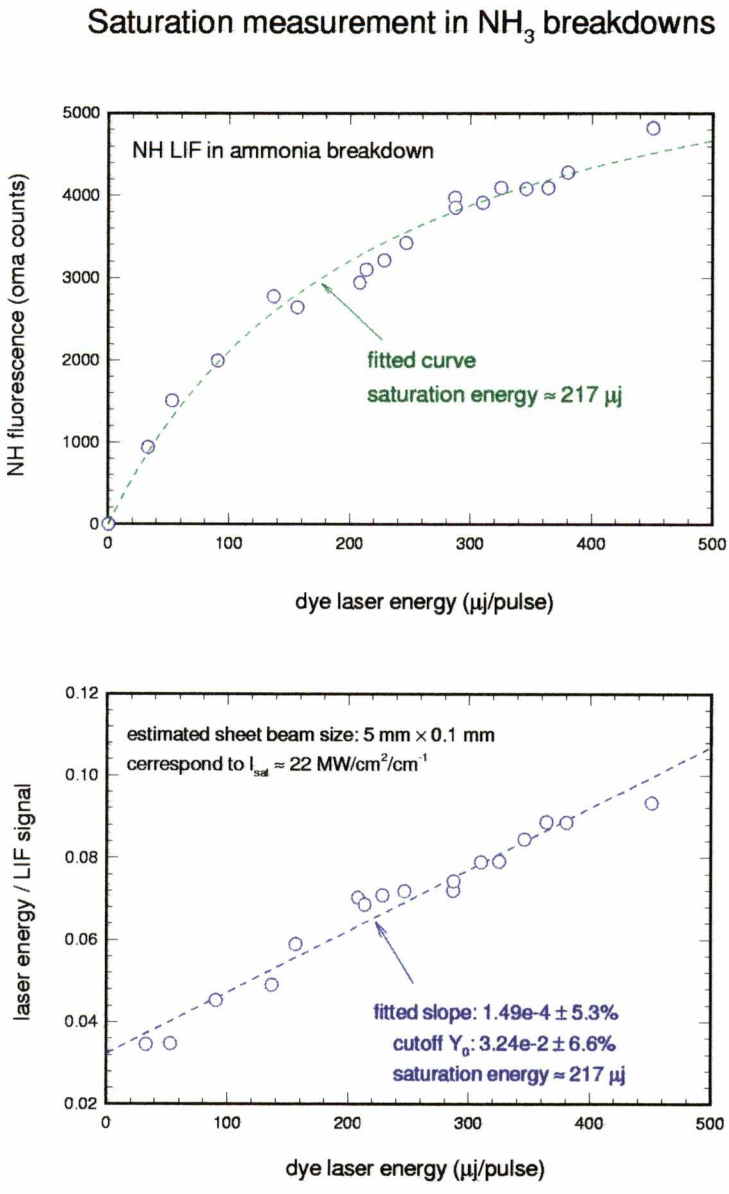



Figure 7.9: Measurement of LIF saturation irradiance in atmospheric pressure pure ammonia breakdowns; transient breakdown kernels at 5 $\mu sec$ delay time were detected

presented in Figures 7.10 and 7.14. The average deviations of linear fitting over the whole temperature image are about 2.0–4.0 per cent. The region with largest fluorescence signal around the NH molecular shell layer has the smallest percentage of fitting error. In the center of the kernel, the uncertainty is greater due to the larger background noise from the spontaneous emission. Also, outside the kernel, the NH fluorescence reduces dramatically, thereby resulting in an increase of the uncertainty of the Boltzmann plot. A typical Boltzmann plot of a single recorded point is shown in Figure 7.13. The error bars in the Boltzmann plot were determined by the analysis of the deviations between single breakdown events, and the magnitude of error bars were used as weighting factors in the least-squares fitting algorithm.

The corresponding NH PLIF images used to calculate the temperature maps are shown in Figures 7.11 and 7.15. As described in Chapter 6, once the molecular temperature is known, the relative molecular density can be determined. Figures 7.12 and 7.16 show the NH concentration images of the ammonia breakdowns. The absolute concentration values in Figures 7.12 and 7.16 were evaluated by comparing fluorescence signals between ammonia breakdown and ammonia/oxygen ignition, and the normalization to the densities obtained in the combustion calculation discussed in Chapter 2.

Compared with the time-resolved temperature maps shown in Figure 7.14, one can clearly see that the NH spontaneous emission images shown in Figure 7.4 reveal the thermodynamics of the breakdown kernel instead of the NH population, as we predicted. The NH molecules are mostly populated at spatial locations where the temperature is in the approximate interval of 2600-2800 $K$. The calculated

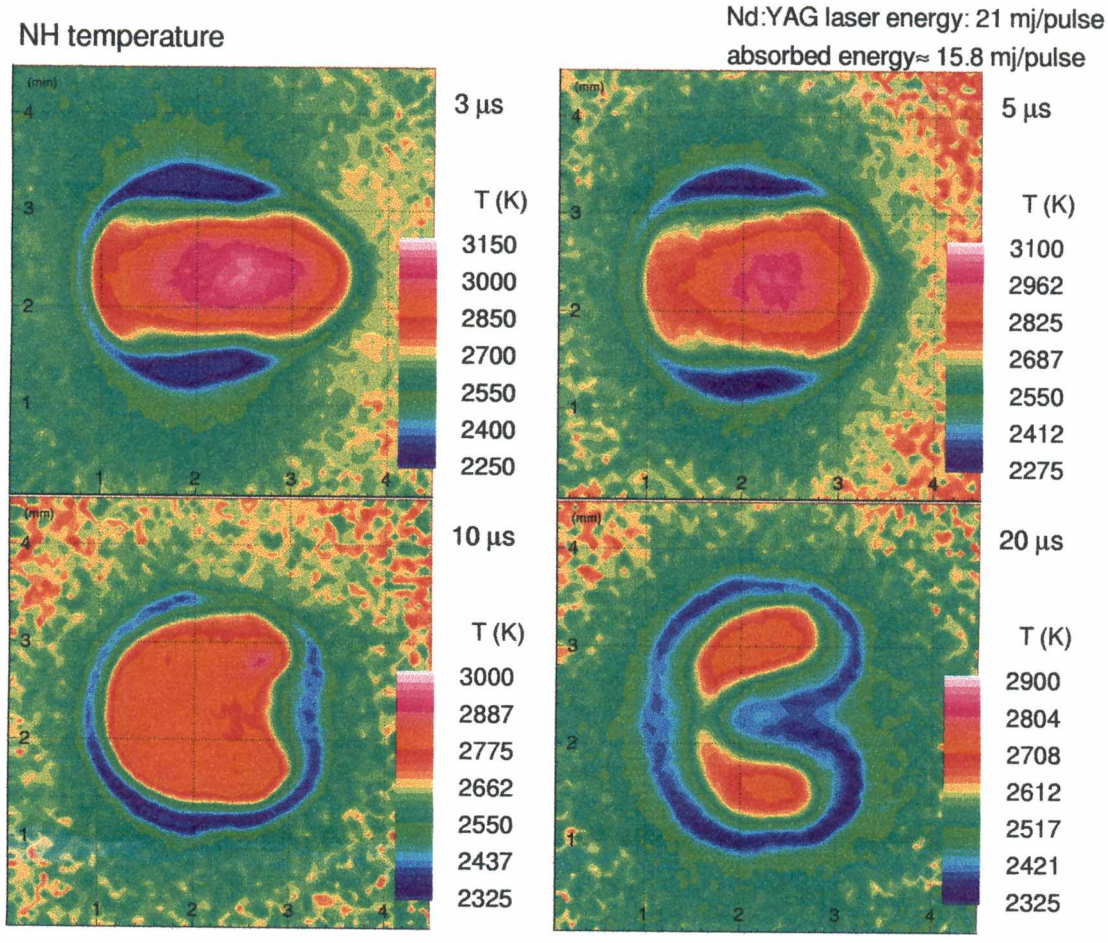



Figure 7.10: Time-resolved temperature images of laser-induced ammonia breakdowns recorded at 3, 5, 10 and 20 $\mu sec$ after breakdown were initialed. Nd:YAG laser pulse energy = 21 $mJ$

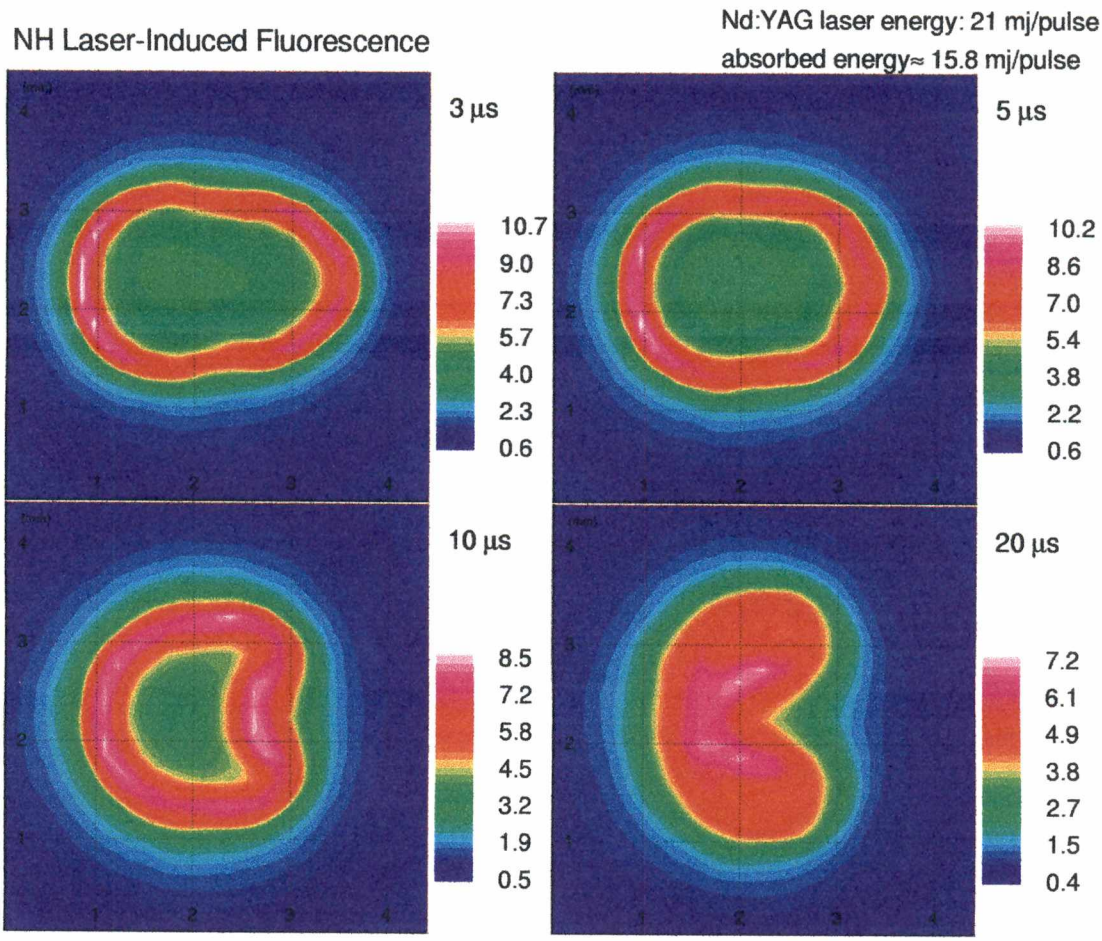



Figure 7.11: Time-resolved NH PLIF images of laser-induced ammonia breakdowns used to calculate temperature maps. Nd:YAG laser pulse energy = 21 $mJ$

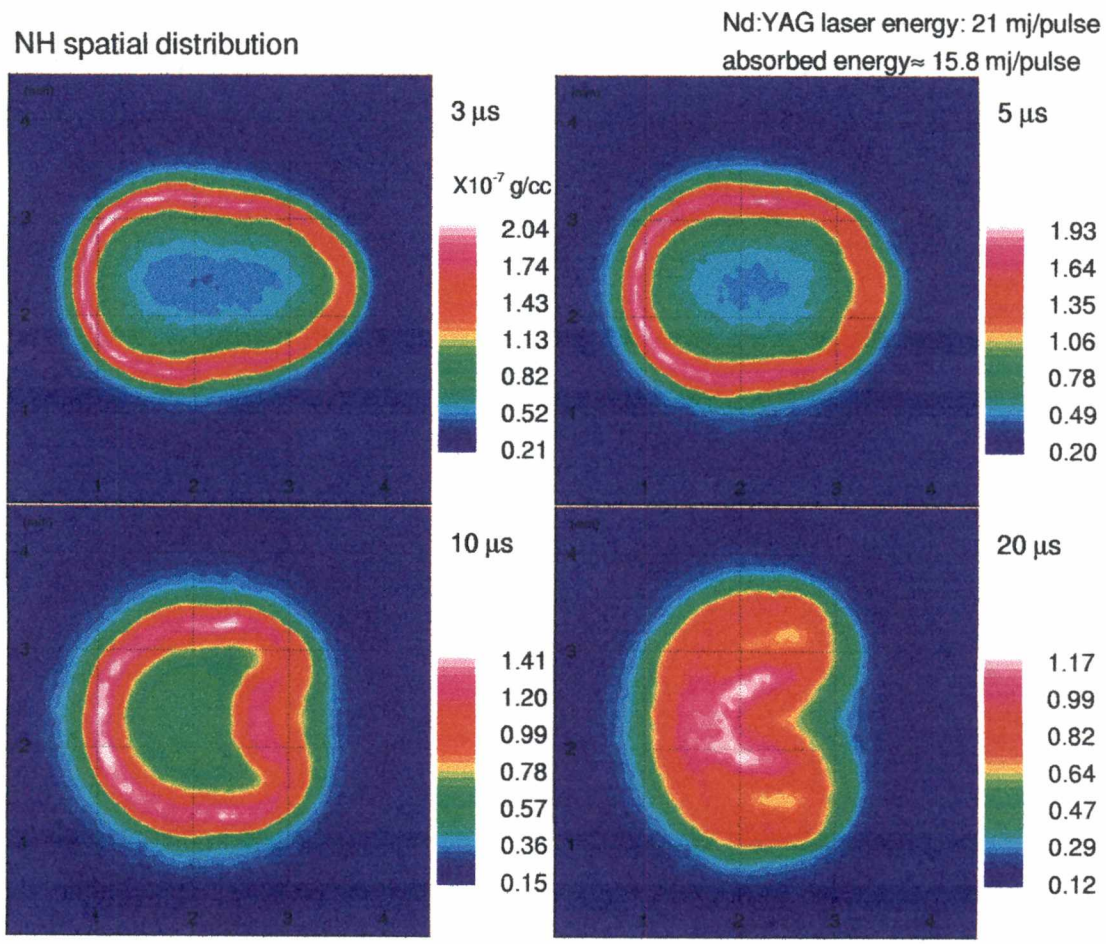



Figure 7.12: NH concentration images of laser-induced ammonia breakdowns calculated from NH PLIF and temperature maps. Nd:YAG laser pulse energy = 21 $mJ$

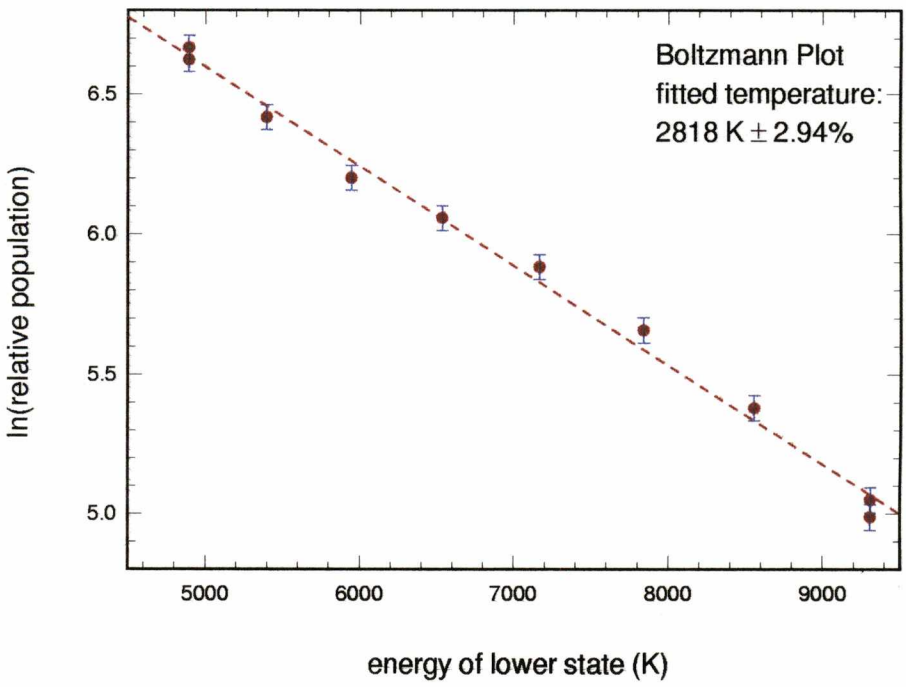



Figure 7.13: The Boltzmann plot of a single pixel in two-dimensional temperature measurement

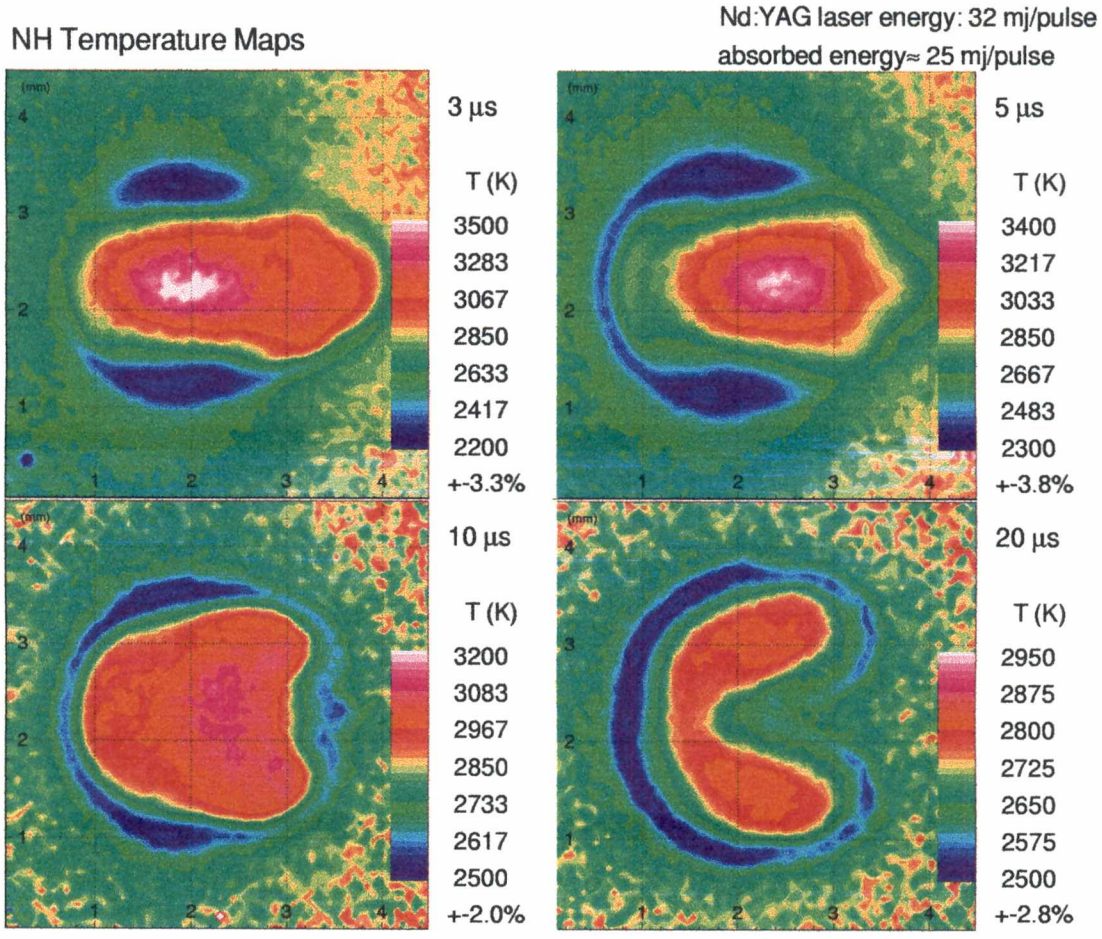



Figure 7.14: Time-resolved temperature images of laser-induced ammonia breakdowns recorded at 3, 5, 10 and 20 $\mu sec$ after breakdown were initialed. Nd:YAG laser pulse energy = 32 $mJ$

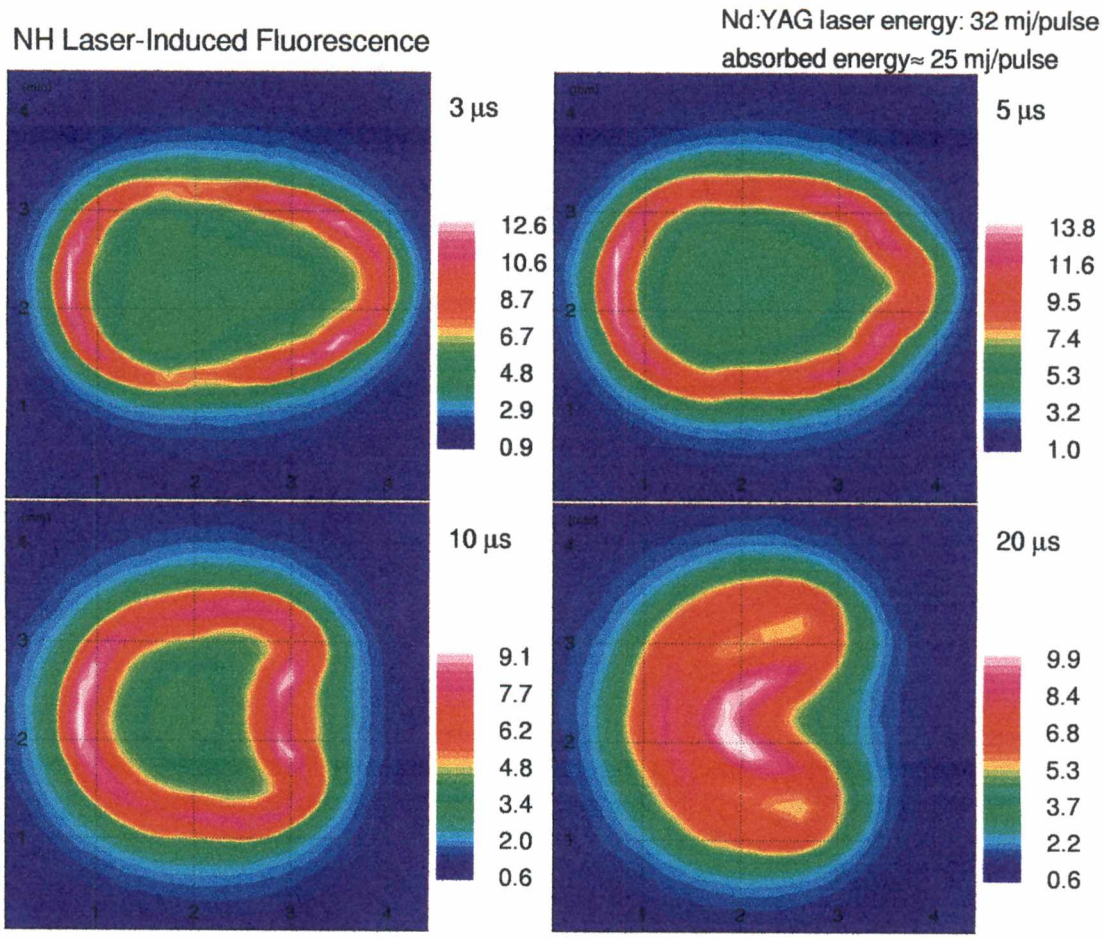



Figure 7.15: Time-resolved NH PLIF images of laser-induced ammonia breakdowns used to calculate temperature maps. Nd:YAG laser pulse energy = 32 $mJ$

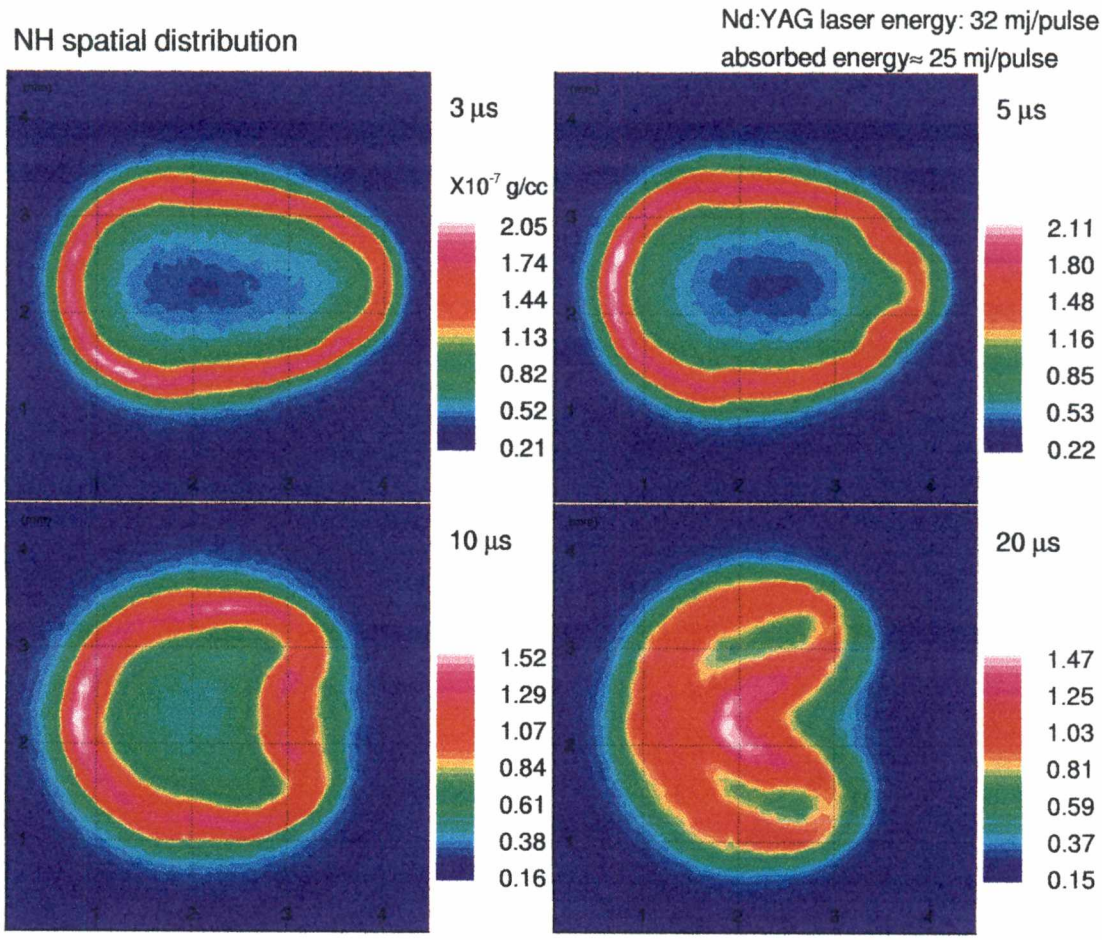



Figure 7.16: NH concentration images of laser-induced ammonia breakdowns calculated from NH PLIF and temperature maps. Nd:YAG laser pulse energy = 32 $mJ$

temperature outside the NH shell can not be used since the NH density is extremely low in these areas and the very small detected fluorescence signal could be from the scattering in the imaging process. In future studies, a molecule that is populated over all the kernel regimes, such as OH, would be a more suitable choice for the measurement of temperature distribution.

## 7.4 Features of Kernel Development

For all the investigations from Chapter 3 to this point, the important features of the ammonia breakdowns under incident Nd:YAG laser beams with energies of 32 $mJ$ (or absorptions of $\sim 26mJ$), and pulse widths of $\sim 6.5$ $nsec$ are summarized:

1. The formation stage ($< 20$ $ns$): The initial plasma is developed in this period as a laser-supported radiation wave (see section 3.1 and 3.2). The initial plasma is optically thick and absorbs practically all the laser energy in the wave front. The growth of the plasma appears as a propagating wave with the speed of $20 \sim 80$ $km/sec$. By the end of this period, the initial plasma is formed along the optical axis with a length of $\sim 1$ $mm$ and the diameters of 35 $\mu m$ in the back (near the focal point) and 200 $\mu m$ in the front side (the lens side). The mass density of plasma is about the same order of magnitude as that before the breakdown. The temperature inside the kernel is estimated $> 100,000$ $K$, and the plasma pressure is estimated larger than $10^3$ $bar$. The ionization process inside the LSR plasma is very strong and the modeling of such a problem requires consideration of, at least, triply ionized species.

2. Post-breakdown time $\cong 1$ $\mu sec$: The initial plasma has already expanded to an egg-shaped kernel with length of $\sim 2$ $mm$ and diameter of $\sim 1.5$ $mm$ toward the wider side (front side). The kernel size is estimated by the NH-molecule shell in the PLIF images instead of shadowgraphs for which the boundary was not clearly defined.

3. Post-breakdown time $\cong 2.5$ $\mu sec$: The shock wave separates from the hot kernel and propagates outward. The kernel size was about 3 $mm$ in length and 2 $mm$ in diameter, which implies an expansion of approximately 1000 times of size from the initial plasma. The gas pressure inside the kernel appears to be close to the pressure outside the kernel. The breakdown kernel is optically thin to the UV laser around 340 $nm$, even for the resonant excitations of the NH transitions. This property can be seen from the Rayleigh scattering as shown in Figure 7.17 and the NH PLIF images in the ammonia-flow breakdown. Inside the hot gas kernel, NH molecules are formed in a hollow shell near the boundary of the kernel, and their temperature is distributed in the region of $2500 \sim 2800K$.

4. Post-breakdown time $\simeq 10 - 50$ $\mu sec$: No significant change in the kernel size is observed in this period of time. The pressure inside the kernel is practically the same as in the ambient gas. However, the formation of the toroidal geometry starts. An asymmetrical gaseous motion force inward along the axis and outward in the radial direction appears. This motion starts earlier and stronger in the backside of the kernel and is observed later and weaker in the front side. When the motion from both sides of the kernel meet, and the stronger motion

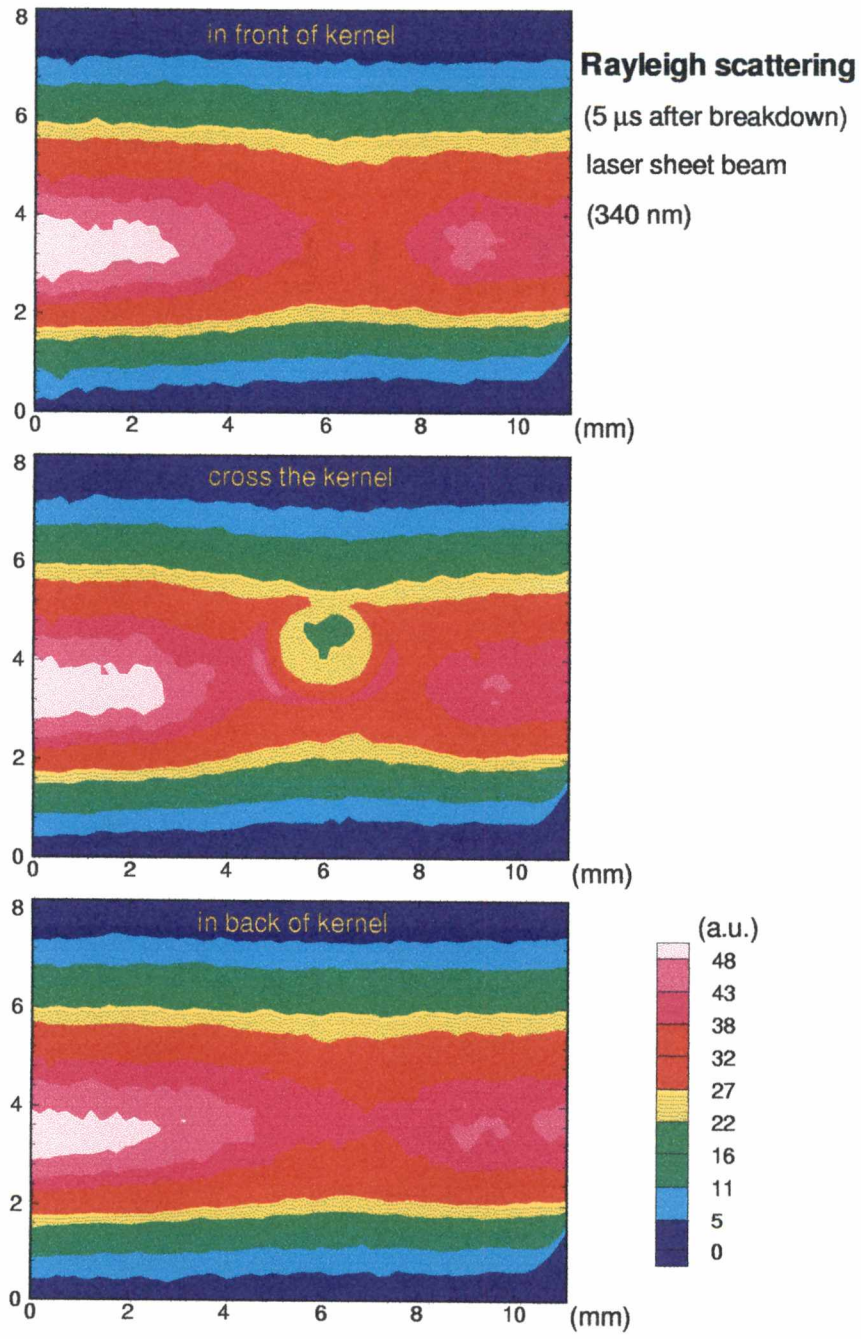



Figure 7.17: Rayleigh scattering of the sheet laser beam in front of the kernel (upper image), across the kernel (middle image), and in the back of the kernel (lower images); Images were recorded at 5 $\mu sec$ after breakdown were initialed

from the backside overcomes the weaker one and pushes the core of the kernel toward the front, the backstreaming effect appears.

5. Post-breakdown time 50 $\mu sec \sim 10msec$: The backstreaming motion continues and gradually slows and weakens. Finally, the kernel decays and fades out as the gas diffusion continues.

When the optical breakdown takes place in a combustible gas mixture, the chemical reactions contribute significantly to the developing hot kernel as early as 20 $\mu sec$ of time. A successful ignition requires the establishment of a proper temperature gradient to support the consequent exothermic reactions and start a self-sustained flame front. The minimum ignition energy in laser-induced breakdown depends on the focusing optical geometry and the energy losses before the initial plasma develops into a proper ignition kernel. As observed in our laser-ignition experiments, formation of a closed NH-molecule shell seems to be one of the necessary conditions for a successful ignition (see section 4.3). The NH shell may ensure a proper temperature gradient and/or a suitable fuel/oxidant combination for the subsequent chemical reactions.

# Chapter 8

# Summary

In this dissertation, the investigation of the pulsed laser-induced breakdown and ignition of the atmospheric-pressure ammonia and ammonia/oxygen mixtures was carried out using an Nd:YAG laser operated at 1064-$nm$ wavelength, with a pulse width of 6.5-$nsec$. The study illustrated the features of both the plasma formation and the decay following the laser-induced breakdown. The first part of the study presented an overview of the physics of optical breakdown and laser ignition in Chapter 2, and the calculated results of the ammonia/oxygen flame are presented for the ignition study in the following chapters. Flame temperature and mole fractions of various molecules were calculated for both equilibrium and non-equilibrium conditions. The computed results predicted the location and time of the formation of the transient radical NH in the one-dimensional free propagating flame. The NH molecules were found in a thin layer with thickness of $\sim 0.3$ $mm$ in the flame-front with maximum mole fraction of $3\times10^{-3}$, which is three orders of magnitude larger than the equilibrium NH concentration at the completion of the reactions. Therefore, experimentally, NH was used as an indicator of the chemical kinetics in the $NH_3$ breakdown and $NH_3/O_2$ laser ignition processes.

The laser-induced breakdown, plasma formation, and subsequent reaction chemistry of $NH_3$ and $NH_3/O_2$ mixtures were studied as a function of the energy of the incident laser beam. In the course of the study, it was found that the optical quality of the laser beam and the flow-speed of the flat-flame burner were significant influences on the overall results of the experiments. Chapters 3 and 4 discussed in detail these results. In Chapter 3, measurements of the spatial and temporal profiles of the laser-induced plasma radiation revealed features of an energy deposition process that was asymmetric in both space and time. The measured time-dependence of the absorbed laser energy showed, as expected, the rapid free-electron growth rate relative to the 6.5 $nsec$ laser pulse-width, and it demonstrated the critical importance of the shape of the leading edge of the incident pulse. Further, the data clearly showed the stochastic nature of the breakdown process and the probability distribution function of the absorbed energy. The spatial features showed that the induced plasma exhibited a laser-supported radiation wave (LSR) with the plasma propagation speed of tens kilometer per second, depending on the temporal laser irradiance in the plasma front. The expansion of the plasma wave grew from the Rayleigh range of the focal zone and indicated a continuously decreasing absorbed energy density along the optical axis.

For the laser-induced ammonia breakdown, it was found that the magnitude of the flow-speed of ammonia from the McKenna burner had a significant effect on the value of the breakdown threshold and the stability of the plasma formation. Chapter 4 presents the results of the investigation of these effects. It was shown that, for a specified spatial position within the flow, a variation of the flow-speed from 6 to 1

$cm/sec$ had significant effect on the breakdown and ignition results. It was found that this effect could be attributed first to gas mixing of the $NH_3$ and $NH_3/O_2$ effluent with the surrounding atmosphere and second to the apparent presence of liquid $NH_3$ aerosol at high ammonia flow rates. The $NH_3$ condensation results in fluctuations of the flow-rate that affected the breakdown events and increased the complexity of the analysis.

Following the investigations of the initial plasma and the flow effects, the development of the breakdown kernel was studied using the high-speed photographic and spectroscopic techniques. As shown in Chapter 5, the high-speed photographic technique offered the advantage of recording a complete sequence of images for a single breakdown event. We compared the shadowgraph images of the breakdown kernels with different absorbed energies, and the resulting laser ignitions in various gas mixtures. The gas dynamics and the backstreaming effect in laser-induced gas breakdown and ignition were shown and discussed. The results and analysis showed that the spatial geometry of the energy deposition, as described in Chapter 3, and the subsequent shock wave ($\sim$ 3 $\mu sec$) were responsible for the asymmetric kernel development at later times ($>$ 10 $\mu sec$).

A variety of spectroscopic and imaging techniques were used to visualize and quantify selected features of the gas dynamics and thermochemistry of the laser-induced ignition phenomenon. Both point-measurements and two-dimensional images were acquired over time scales that spanned the ranges that begin with plasma formation and conclude with the ignition and combustion events. The detailed results of these studies will be crucial to the understanding and development of the theoretical de-

scription of the laser-induced breakdown and ignition process. The following Table and Figure 8.1 summarize these measurements.

| Types of Images | Spatial / Temporal Res. | Size of Image |
|---|---|---|
| Shadowgraphs in ignitions | 110 $\mu m$ / 30 $ns$ | 14×14 $mm^2$ |
| Shadowgraphs in breakdowns | 110 $\mu m$ / 30 $ns$ | 14×14 $mm^2$ |
| Temperature in breakdown | 70 $\mu m$ / 10 $ns$ | 4.5×4.5 $mm^2$ |
| NH PLIF in ignitions | 60 $\mu m$ / 10 $ns$ | 4.5×6.0 $mm^2$ |
| NH PLIF in breakdowns | 60 $\mu m$ / 10 $ns$ | 4.5×4.5 $mm^2$ |
| Electron/ion radiation | 8.5$\sim$ 60 $\mu m$ / 5 $ns$ | (1.5 $mm$)$^2 \sim$ (4.5 $mm$)$^2$ |
| NH spontaneous emission | 60 $\mu m$ / 5 $\sim$ 100 $ns$ | 4.5×4.5 $mm^2$ |

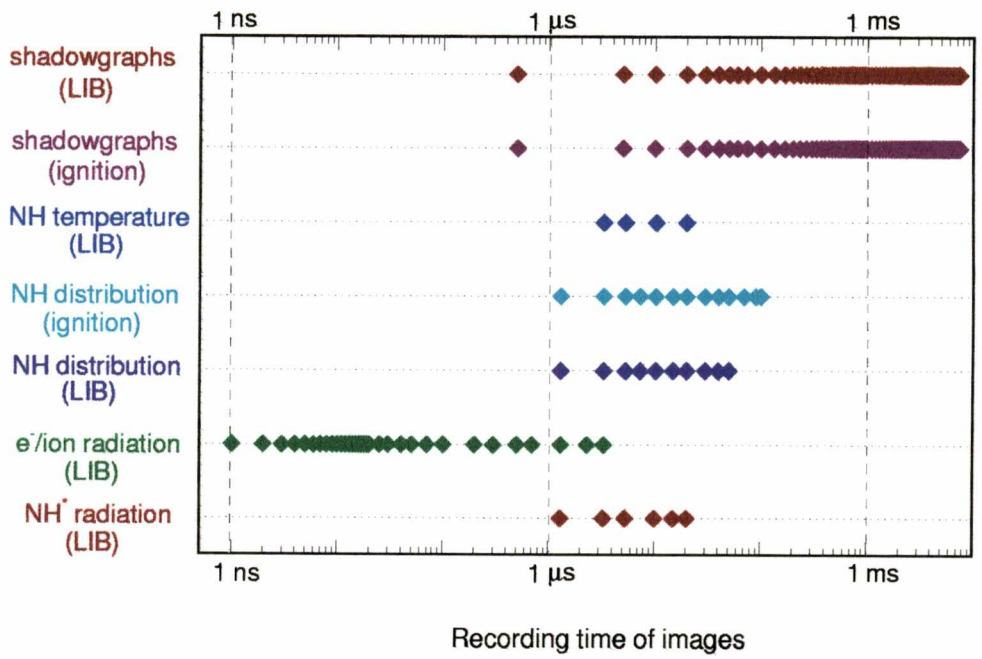



Figure 8.1: Chart of recording time of the two-dimensional images presented in this dissertation

# Bibliography

# Bibliography

[1] "The new encyclopedia Britannica". vol. 2, 634, Encyclopedia Britannica, Inc., Chicago, 1994.

[2] "The new encyclopedia Britannica". vol. 2, 84-86, Encyclopedia Britannica, Inc., Chicago, 1994.

[3] E. C. Watson. "Reproductions of prints, Drawing and Paintings of interest in the history of physics - 14A. Paintings of lectures at the Royal Institution: Michael Faraday Lecture on Metals, Dec. 27, 1855". American Journal of Physics, 8, 1-6: 387-30, 1940.

[4] A. H. Lefebvre. "Gas turbine combustion". p221-256, Hemisphere publishing Corp., New York, 1983.

[5] J. D. Few and J. W. L. Lewis. "Gas turbine engine photon ignition system". U.S. Patent number 4,947,640, Aug. 14, 1990.

[6] J. D. Few and J. W. L. Lewis. "Laser-initiated non-linear fuel droplet ignition". U.S. Patent number 5,485,720, Jan. 23, 1993, Patent number 5,404,712, April 11, 1995, Patent number 5,497,612, March 12, 1996, Patent number 5,524,429, June 11, 1996.

[7] F. J. Weinberg and J. R. Wilson. "Preliminary investigation of the use of focused laser beams for minimum ignition energy studies". Proc. Roy. Soc. Lond. Series A 321, 41-52, 1971.

[8] G. F. Carrier, F. E. Fendell, and M. S. Chou. "Laser-initiated conical detonation wave for supersonic combustion. III". AIAA paper 92-3247, 28th AIAA/SAE/ASME/ASEE joint propulsion Conference and exhibit, Nashville, 1992.

[9] R. G. Kingdon and F. J. Weinberg. "Effect of plasma constitution on laser ignition energies". In 16th international Symposium on combustion, 747-756, Combustion Institute, Pittsburgh, 1976.

[10] J. A. Syage, E. W. Fournier, R. Rianda, and R. B. Chen. "Dynamics of flame propagation using laser-induced spark initiation: ignition energy measurements". J. Appl. Phys., 64, 1499-1507, 1988.

[11] J. H. Lee and R. Knystautas. "Laser spark ignition of chemically reactive gases". AIAA J. 7, 312-317, 1969.

[12] H. M. Thompson, J. W. Daiber, and R. G. Rehm. "Two-dimensional growth of laser-driven waves in a hydrogen free jet". J. Appl. Phys., 47, 2427-2432, 1976.

[13] V. F. Klimkin, R. I. Soloukhin and P. Wolansky. "Initial stages of a spherical detonation directly initiated by a laser spark". Combust. Flame, 28, 61-66, 1977.

[14] B. E. Forch, and A. W. Miziolek. "Ultraviolet laser ignition of premixed gases by efficient and resonant multiphoton photochemical formation of microplasma". Combust. Sci. Tech. 52, 151-159, 1987.

[15] B. E. Forch, and A. W. Miziolek. "Laser-based ignition of $H_2/O_2$ and $D_2/O_2$ premixed gases through resonant multiphoton excitation of H and D atoms near 243 nm". Combust. Flame, 85, 254-262, 1991.

[16] M.-S. Chou, F. E. Fendell, and H. W. Behrens. "Theoretical and experimental studies of laser-initiated detonation waves for supersonic combustion". Proc. SPIE, 1862, 45-58, 1993.

[17] R. A. Hill. "Ignition-delay times in laser-initiated combustion". Appl. Opt., 20, 2239-2242, 1981.

[18] D. H. Plemmons. "Laser-spark ignition and the NH radical". PhD thesis, The University of Tennessee Space Institute, 1996.

[19] D. R. Ballal and A. H. Lefebvre. "The influence of flow parameters on minimum ignition energy and quenching distance". In 15th International Symposium on Combustion, 1473-1480, Combustion Institute, Pittsburgh, 1974.

[20] P. S. Tromans and R. M. Furzeland. "An analysis of Lewis number and flow effects on the ignition of premixed gases". In 21st International Symposium on Combustion, 1891-1897, Combustion Institute, Pittsburgh, 1986.

[21] G. G. DeSoete. "The influence of isotropic turbulence on the critical ignition energy". In 13th International Symposium on Combustion, 735-743, Combustion Institute, Pittsburgh, 1970.

[22] J. M. Seitzman, P. H. Paul, and R. K. Hanson. "Digital imaging of laser-ignited combustion". AIAA-88-2775, Thermophysics, Plasmadynamics and Lasers Conference, San Antonio, TX, 1988.

[23] T. A. Spiglanin, A. Mcilroy, E. W. Fournier, R. B. Cohen, and J. A. Syage. "Time-resolved imaging of flame kernels: laser-spark ignition of $H_2/O_2/Ar$ mixtures". Combustion and flame, 102, 310-328, 1995.

[24] P.D. Maker, R. W. Terhune, and C. M. Savage. "Optical third harmonic generation". In III Int. Conf. On Quant. Electronics, Paris, 1963.

[25] C. DeMichelis. "Laser induced gas breakdown: A bibliographical review". IEEE J. Quantum Electron., QE-5, 5: 188-202, 1969.

[26] G. V. Ostrovskaya and A. N. Zaidel. Usp. Fiz. Nauk, 111: 579, 1973.

[27] C. G. Morgan. "Laser-induced breakdown of gases". Rep. Prog. Phys. (GB) 38, 5: 621-665, 1975.

[28] Y. P. Raizer. "Laser-Induced Discharge Phenomena". Consultants Bureau, New York, 1977.

[29] C. G. Morgan. "Laser-induced electrical breakdown of gases". In electrical breakdown of gases, J. M. Meek, J. D. Crags, Eds., 717-752, Wiley, New York, 1978.

[30] G. M. Weyl. "Physics of laser-induced breakdown: an update". In L. J. Radziemski and D. A. Cremers, editors, "Laser-Induced Plasma and Applications". Marcel Dekker, Inc., New York, 1989.

[31] R. G. Root. "Modeling of post-breakdown phenomena". In L. J. Radziemski and D. A. Cremers, editors, "Laser-Induced Plasma and Applications". Marcel Dekker, Inc., New York, 1989.

[32] T. Keldysh. "Ionization in the field of a strong electromagnetic wave". Sov. Phys. JETP, 20, 1307-1314, 1965.

[33] G. Baravian, J. Godart, and G. Sultan. "Multiphoton ionization of molecular nitrogen by a Neodymium-glass laser". Phys. Rev., A25, 1483-1495, 1982.

[34] J. A. Stamper, B. H. Ripin, R. E. Peterkin, Jr. and R. F. Stellingwerf. "Aneurisms in laser-driven blast waves". Phys. Fluids, 31, 11: 3353-3361, 1988.

[35] W. M. Trott. "$CO_2$-laser-induced deflagration of fuel/oxygen mixtures". J. Appl. Phys., 54, 118-130. 1983.

[36] B. E. Forch, and A. W. Miziolek. "Oxygen-atom two-photon resonance effects in multiphoton photochemical ignition of premixed $H_2/O_2$ flow". Opt. Lett., 11, 3: 129-131, 1986.

[37] N. M. Witriod, B. E. Forch, and A. W. Miziolek. "Modeling laser-ignition of combustible gases". CPIA Publication 557, III, 213-217, 1990.

[38] P. D. Ronney. "Laser versus conventional ignition of flames". Optical Engineering, 33, 510-521, 1994.

[39] B. Lewis and G. von Elbe. "Combustion, flames, and Explosions of gases". 3rd ed., Academic Press, New York, 1987.

[40] S. Gordan and B. McBride. "Computation program for calculation of complex equilibrium compositions, rocket performance, incident and reflected shocks, and Chapman-Jouguet detonations". Interim Revision NASA Report SP-273, NASA Lewis Research Center, 1976.

[41] R. J. Kee, J. F. Grcar, M. D. Smooke, and J. A. Miller. "A FORTRAN program for modeling steady one dimensional flames". Technical Report SAND85-8240, Sandia National Laboratories, 1985.

[42] V. Ya. Basevich and V. I. Vedeneev. "Propagation of a laminar ammonia flame". Combust. Explos. Shock Waves, 27, 559-564, 1991.

[43] G. A. Hill, D. J. James, and S. A. Ramsden. "Breakdown thresholds in rare and molecular gases using pulsed 0.6 micron radiation". J. Phys. D. Appl. Phys., 5, L97-99, 1971.

[44] C. H. Chan, C. D. Moody, and W. McNight. "Significant loss mechanisms in gas breakdown at 10.6 $\mu m$". J. Appl. Phys., 44, 1179-1188, 1973.

[45] D. E. Lencioni. "The effect of dust on 10.6 $\mu m$ laser induced air breakdown". Appl. Phys. Lett., 23, 12-14, 1973.

[46] R. E. Schlier, A. N. Pirri, and D. J. Reilly. "Air breakdown studies". Rep. AFWL-TR-72-74, AVCO Everett Res. Lab. Everett, Mass. 1973.

[47] G. H. Canavan, and R. E. Nielsen. "Focal spot dependence of gas breakdown induced by particulate ionization". Appl. Physics. Lett., 22, 409-410, 1973.

[48] S. Yalcin, D. R. Crosey, G. P. Smith, and G. W. Faris. "Spectroscopically determined temperatures and electron densities in laser produced sparks". In 1995 OSA Annual Meeting/ILS-XI Program, page 147, Portland, Oregon, September 1995. Optical society of America and Laser Science Topical Group/APS.

[49] G. Guan and C. Parigger. private communication. Center for Laser Applications, University of Tennessee Space Institute.

[50] C. Parigger, Y. Tang. D. H. Plemmons, and J. W. L. Lewis. "Spherical aberration effects in lens-axicon doublets: theoretical study". Appl. Optics, 36, 31: 8214-8221, 1997.

[51] V. I. Bergel'son. T. V. Loseva, I. V. Nemchinov, and T. I. Orlova. "Propagation of plane supersonic radiation waves". Sov. J. Plasma Phys., 1: 498-503, 1976.

[52] Y. P. Raizer. "Heating of gas by a powerful light pulse". Sov. Phys. JETP, 21, 5: 1009, 1965.

[53] Y. P. Raizer. "The laser spark and propagation of discharges". In Russian, Nauka, Moscow, 1974.

[54] C. F. Bohren and D. R. Huffman. "Absorption abd scattering of light by small particles". John Willey & Sons, Inc., 1983.

[55] R. M. Measures. "Laser Remote Sensing: fundamentals and applications". Krieger Publishing Company, Malabar, Florida, 1992.

[56] L. A. Vasil'ev. "Schlieren methods". Keter Inc., New York, 1971.

[57] H. W. Liepmann and A. Roshko. "Elements of gasdynamics". John Willey & Sons, Inc., New York, 1957.

[58] J. N. Bradley. "Shock waves in chemistry and physics". John Willey & Sons, Inc., New York, 1962.

[59] D. Bershader. "Some aspects of the refractive behavior of gases". In D. S. Dosanjh, editor, "Modern optical methods in gas dynamic research". Plenum Press, New York, 1971.

[60] G. V. Sklizov. "Laser in high-speed photography". In Laser Handbook, ed. F. T. Arecchi and E. O. Schulz-Du Bais, 1545, 1972.

[61] H. Goldstein. "Classical mechanics". Addision-Wesley Publishing Com., Menlo Park, California, Second edition, 1981. Chapter 10.

[62] A. Heath. "Geometrical Optics". Cambridge, 1897.

[63] M. T. Lim, R. W. Anderson, and V. S. Arpaci. "Prediction of Spark Kernel Development in Constant Volume". Combustion and Flame, 69, 303-316, 1987

[64] M. Kono, K. Niu, T. Tsukamoto, and Y. Ujiie. "Mechanism of flame kernel formation produced by short duration sparks". In Twenty-Second Symposium (International) on Combustion, pages 1643-1649, Pittsburgh, 1988. The Combustion Institute.

[65] J. A. Stamper, B. H. Ripin, R. E. Peterkin, Jr. and R. F. Stellingwerf. "Aneurisms in laser-driven blast waves", Phys. Fluids, 31, 11: 3353-3361, 1988

[66] V. Ya. Basevich and V. I. Vedeneev. "Propagation of a laminar ammonia flame". Combust. Explos. Shock Waves, 27, 559-564, 1991

[67] A.Fowler and C. C. L. Gregory, Philos. Trans. R. Soc. A 218, 251, 1919.

[68] G. K. Funke, Z. Phys. 96, 787, 1935.

[69] R. N. Dixon, Can. J. Phys. 37, 1171, 1959.

[70] C. R. Brazier, R. S. Ram, and P. F. Bernath. "Fourier transform spectroscopy of the $A^3\Pi_i$-$X^3\Sigma^-$ transition of NH". J. Mol. Spectrosc. 120, 2: 381-402, 1986.

[71] J. O. Hornkohl, C. Parigger, and J. W. L. Lewis. "On the use of line strengths in applied diatomic spectroscopy". Submitted to Optical Society of America for presentation in the 1995 conference on Laser Applications to Chemical and Environmental Analysis, March 1996.

[72] J. O. Hornkohl, C. Parigger, and J. W. L. Lewis. "Computation of Synthetic diatomic spectra". In Laser Applications to Chemical Analysis, 1994 Technical Digest Series, 5: 234-237, Washington, DC, 1994. Optical Society of America.

[73] A. P. Thorne. "Spectrophysics". Chapman and Hall, New York, New York, Second edition, 1988. Table 11.1.

[74] D. R. Crosley and G. P. Smith. "Laser-induced Fluorescence spectroscopy for combustion diagnostics". Opt. Eng., 22, 545-553, 1981.

[75] D. R. Crosley. "Collision effects on laser-induced Fluorescence flame measurements". Opt. Eng., 20, 511-521, 1981.

[76] E. L. Chappell, J. B. Jeffries, and D. R. Crosley. "Collisional quenching of highly rotationally excited NH ($A^3\Pi_i$)". J. Chem. Phys., 97, 4: 2400-2405, 1992.

[77] A. Kaes and F. Stuhl. "Quenching, Λ-doublet mixing and fluorescence lifetimes of single excited NH($A^3\Pi, v' = 0, N', J', e/f$) states". J. Chem. Phys. 97, 10: 7362-7370, 1992.

[78] N. L. Garland and D. R. Crosley. "Rotational level dependent quenching of the $A^3\Pi_i, v' = 0$ state of NH " J. Chem. Phys. 90, 7: 3566-3573, 1989.

[79] M. Kollner, P. Monkhouse, and J. Wolfrum, "Time-resolved LIF of OH($A^2\Sigma^+, v = 1$ and $v = 0$) in atmospheric-pressure flames using picosecond excitation", Chem. Phys. Lett., 168, 3, 4: 355-360, 1990.

[80] A. Dreizler, R. Taddy, P. Monkhouse, and J. Wolfrum. Appl. Phys. B 57, 85, 1993.

[81] M. Kollner and P. Monkhous. "Time-resolved LIF of OH in the flame front of premixed and diffusion flames at atmospheric pressure." Appl. Phys. B 61, 499-503, 1995.

[82] K. J. Rensberger, J. B. Jeffries, R. A. Copeland, K. Kohse-Hoinghaus, M. L. Wise, and D. R. Crosley. "Laser-induced fluorescence determination of temperature in low pressure flames". Appl. Optics, 28, 17: 3556-3566, 1989.

[83] J. B. Jeffries, R. A. Copeland, G. P. Smith, and D. R. Crosley. "Multiple species laser-induced fluorescence in flames". Twenty-first symposium (International) on combustion/ The combustion institute, 1709-1718, 1986.

[84] J. A. Vanderhoff, W. R. Anderson, A. J. Kotlar, and R. A. Beyer. "Raman and fluorescence spectroscopy in a methane-nitrous oxide laminar flame". Twentieth symposium (International) on combustion/ The combustion institute, 1299-1306, 1984.

[85] D. R. Crosley. "Laer-induced fluorescence in spectroscopy, dynamics and diagnostics." J. Chem. Ed. 59: 446-455, 1982.

[86] J. Malicet, J. Brion, and H. Guenebaut. "Spectroscopic study of the $A^3\Pi_i$-$X^3\Sigma^-$ transition in the NH radical". J. Chim. Phys. 67, 1: 25-30, 1970.

[87] K. P. Huber and G. Herzberg. "Molecular spectra and molecular structure IV: constants of diatomic molecules". Van Nostrand Reinhold, New York, 1979.

[88] L. Allen and J. H. Eberly. "Optical resonance and two-level atoms". John Wiley & Sons, Inc., New York, 1974.

[89] R. Loudon. "The quantum theory of light". Second edition, Clarendon Press, Oxford, 1992.

[90] J. T. Salmon, R. P. Lucht, D. W. Sweeney and N. M. Laurendeau. "Laser-saturated fluorescence measurements of NH in a premixed subatmospheric $CH_4/N_2O$/Air flame." Proceedings Twentieth Symposium (Int'l) Combustion, The Combustion Institute, Pittsburgh, PA. 1985.

[91] J. T. Salmon and N. M. Laurendeau. "Analysis of probe volume effects associated with laser-saturated fluorescence measurements." Appl. Opt. 24, 1313-1321, 1985.

[92] D. R. Crosley, G. P. Smith. "Rotation energy transfer and LIF temperature measurements". Comb. Flame, 44, 27-34, 1982.

[93] A. C. Eckbreth. "Laser diagnostics for combustion temperature and species". Ed. By A. K. Gupta, D. G. Lilley, Energy Eng. Sci. Ser., Vol. 7, Abacus, Cambridge, MA 1988.

[94] J. O. Berg and W. L. Shackleford. "Rotational redistribution effect on the saturated laser-induced fluorescence". Appl. Opt., 18: 2093-2094, 1979.

[95] R. P. Lucht, D. W. Sweeney and N. M. Laurendeau. "Balanced cross-rate model for saturated molecular fluorescence in flames using a nanosecond pulse length laser". Appl. Opt., 19: 3295-3300, 1980.

[96] F. Bormann, T. Nielsen, M. Burrows, P. Andresen. "Single-pulse collision-insensitive picosecond planar laser-induced fluorescence of OH $A^2\Sigma^+(v' = 2)$ in atmospheric-pressure flames". Appl. Phys. B, 62: 601-607, 1996.

[97] E. W. Rothe, Y. W. Gu, G. P. Reck. "Laser-induced predissociative fluorescence: dynamics and polarization and the effect of lower-state rotational energy transfer on quantitative diagnostics". Appl. Opt., 35, 6: 934-947, 1996.

[98] D. R. Crosley, G. P. Smith. "Vibrational energy transfer in laser-excited $A^2\Sigma^+$ OH as a flame thermometer". Appl. Opt. 19, 4: 517-520, 1980.

[99] D. Stepowski and M. J. Cottereau. "Time-resolved study of rotational energy transfer in $A^2\Sigma^+(v' = 0)$ state of OH local concentration in a flame by laser-induced fluorescence". J. Chem. Phys. 74, 6674-6679, 1981.

[100] D. R. Crosley. "Collision effects on laser induced fluorescence flame measurements". Opt. Eng. 720, 4: 511-521, 1981.

[101] R. K. Lengel and D. R. Crosley. "Energy transfer in $A^2\Sigma^+$ OH. I. Rotational". J. Chem. Phys., 67, 5: 2085–2101, 1977.

[102] T. A. Caughey and D. R. "Coherence retention during rotationally inelastic collisions of selectively excited diatomic sulfur". Crosley. Chem. Phys., 20, 3: 467–475, 1977.

[103] T. Berglind and J. Sunner. "The temporal development of OH concentration profile in ignition kernels studied by single-pulse laser-induced fluorescence". Combust. Flame, 63: 279-288, 1986.

[104] J. K. Kelnam and A. R. Masri. "Quantitative imaging of temperature and OH in turbulent diffusion flames by using a single laser source". Appl. Opt., 33: 3992-3999, 1994.

[105] A. Hirano and M. Tsujishita. "Visualization of CN by the use of planar laser-induced fluorescence in a cross section of an unseeded turbulent $CH_4$-air flame". Appl. Opt., 33, 33: 7777-7780, 1995.

[106] E. Sher, J. Ben-Ya'ish, and T. Kravchik. "On the birth of spark channels". Combust. Flame, 89: 186-194, 1992.

[107] T. Kravchik and E. Sher. "Numerical modeling of spark ignition and flame initiation in a quiescent methane-air mixture". Combust. Flame, 99: 635-643, 1994.

# Appendices

# Appendix A

# Calibrations of Experimental Apparatus

(a) Laser Energy Control

For all of the experiments described in this dissertation, the pulse energy of the Nd:YAG laser used to induce the optical breakdowns was controlled by two crystal polarizers. The first polarizer was rotatable to have an angle with respect to the second one, which was aligned parallel to the original polarization of the output laser beam. The output pulse energy can be easily controlled between $0\sim$ 90 $mJ$ as shown in Figure A.1. In the experiment to determine saturation energy in the $NH_3$-$O_2$ flame (Figure 7.8), the optics were rearranged, and the same two polarizers were used to control the pumping energy of the dye-laser.

(b) Flow Control

Three mass flow meters, MKS-20000sccm (no.1), MKS-50000sccm (no.2), and MKS-5000sccm (no.3) were used to control the ammonia, oxygen (, air or nitrogen), and argon flows. The calibration results are shown in Figure A.2, and the flow rate of

gases were corrected as:

$$\begin{aligned}
\text{flow rate } (l/min) &= [\text{read out}(volt) + 0.003] \times 4.174 \times \text{G.C.F.}\,, && \text{for meter no.1} \\
&= [\text{read out}(volt) + 0.026] \times 9.601 \times \text{G.C.F.}\,, && \text{for meter no.2} \\
&= [\text{read out}(volt) - 0.012] \times 4.174 \times \text{G.C.F.}\,, && \text{for meter no.3}
\end{aligned} \tag{A.1}$$

where the gas correction factors (G.C.F.) are 1.44 for argon, 0.73 for ammonia and 1.0 for oxygen, nitrogen and air.

(c) Sensitivity calibration for CCD camera and 2-D OMA detection system

For the quantitative measurement of the temperature and concentration images, the linear response over the signal range of the detection system is required. For the purpose of sensitivity calibration, the scattering signals of the dye laser at 340 $nm$ were detected and shown in Figure A.3.

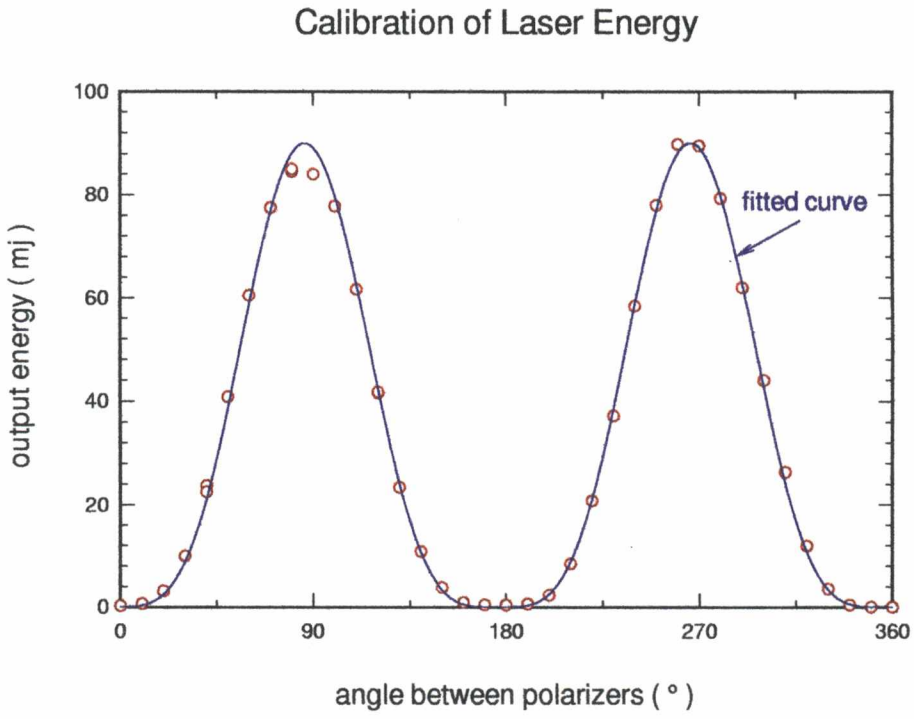



Figure A.1: Laser pulse-energy controlled by two polarizers

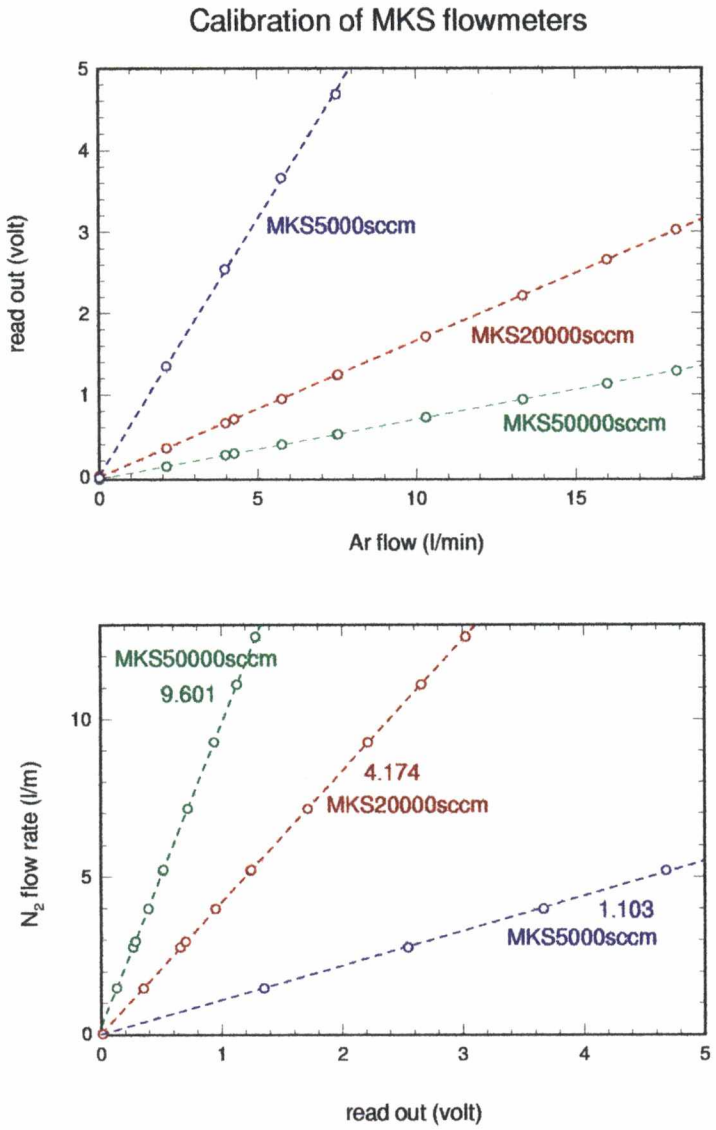



Figure A.2: Calibrations of mass-flow meters, MKS-5000sccm, MKS-20000sccm and MKS-50000sccm

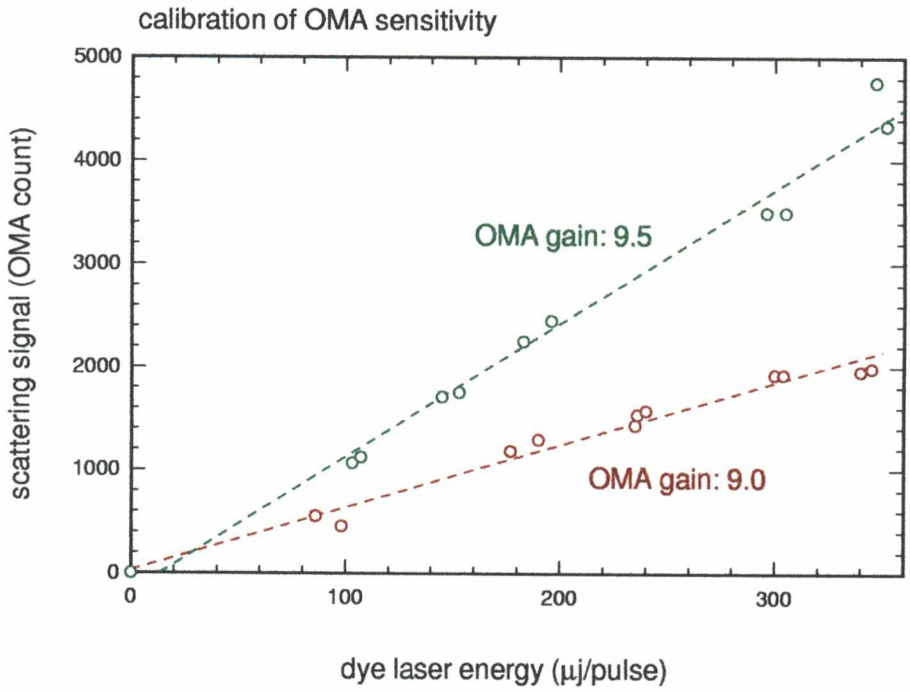



Figure A.3: Sensitivity calibration of CCD camera and two-dimensional OMA detection system

# Vita

Ying-Ling Chen was born in Taiwan on April 2, 1963. In 1981, She enrolled at Fu-Jen Catholic University studying physics and received the degree of Bachelor of Science in 1985. The following August, she enrolled at the graduate institute of The National Central University in Taiwan. She earned her M.S. degree in optical science in 1987. From 1987 to 1989, she worked as an assistant researcher in Chung-Shan Institute of Science and Technology (CSIST). In 1989, she moved to the United States with her husband. In 1991, she enrolled in the graduate school at The University of Tennessee Space Institute (UTSI) studying physics. She earned her Ph.D. in physics in 1998.